

# **Tidal propagation and variable density processes in coastal aquifers**

By

**Silvia Cristina Solórzano-Rivas**

*Thesis Submitted to Flinders University for the degree of*  
**Doctor of Philosophy**

College of Science and Engineering  
June 2021

---

# Table of Contents

<b>TABLE OF CONTENTS</b> .....	<b>I</b>
<b>DECLARATION</b> .....	<b>III</b>
<b>DEDICATION</b> .....	<b>IV</b>
<b>ACKNOWLEDGEMENTS</b> .....	<b>V</b>
<b>SUMMARY</b> .....	<b>VI</b>
<b>LIST OF FIGURES</b> .....	<b>IX</b>
<b>LIST OF TABLES</b> .....	<b>XII</b>
<b>CHAPTER 1</b> .....	<b>1</b>
Technical terminology .....	1
<b>CHAPTER 2</b> .....	<b>4</b>
Introduction .....	4
2.1 Research problem .....	4
2.2 Research objectives .....	6
2.3 Thesis organisation .....	7
<b>CHAPTER 3</b> .....	<b>9</b>
Dispersion effects on the freshwater-seawater interface in subsea aquifers .....	9
3.1 Abstract .....	9
3.2 Introduction .....	10
3.3 Methods .....	12
3.4 Numerical methodology .....	17
3.5 Output variables .....	22
3.6 Mixed convection analysis .....	24
3.7 Results .....	26
3.8 Discussion .....	38
3.9 Conclusions .....	44
<b>CHAPTER 4</b> .....	<b>47</b>
Mixed-convective processes within seafloor sediments arising from fresh groundwater discharge .....	47
4.1 Abstract .....	47
4.2 Introduction .....	48
4.3 Conceptual model .....	50
4.4 Review of mixed-density non-dimensional numbers applicable to SFGD through seafloor sandy sediments .....	52
4.5 Numerical simulation of SFGD .....	55

4.6	Results and discussion .....	59
4.7	Conclusions .....	68
<b>CHAPTER 5.....</b>		<b>69</b>
Applicability of analytical solutions to tidal propagation in circular islands .....		69
5.1	Abstract.....	69
5.2	Introduction .....	70
5.3	Conceptual model .....	71
5.4	Circular-island solution .....	73
5.5	Numerical model .....	75
5.6	The Ferris solution versus the circular-island solution.....	76
5.7	Results and discussion .....	77
5.8	Conclusions .....	85
<b>CHAPTER 6.....</b>		<b>87</b>
Estimating hydraulic properties from tidal propagation in circular islands.....		87
6.1	Abstract.....	87
6.2	Introduction .....	88
6.3	Methods .....	90
6.4	Results and Discussion .....	102
6.5	Conclusions .....	118
<b>CHAPTER 7 CONCLUSIONS.....</b>		<b>120</b>
7.1	Summary of findings .....	120
7.2	Future work .....	122
<b>BIBLIOGRAPHY.....</b>		<b>124</b>
<b>APPENDIX A.....</b>		<b>139</b>
<b>APPENDIX B.....</b>		<b>148</b>

## **Declaration**

I certify that this thesis does not incorporate without acknowledgment any material previously submitted for a degree or diploma in any university; and that to the best of my knowledge and belief it does not contain any material previously published or written by another person except where due reference is made in the text.

.....

Silvia Cristina Solórzano Rivas

## **Dedication**

To my parents, Samuel and Silvia, I would not be standing here without your support in my education. You showed me by your example how to strive for excellence, love learning and be driven. That is the best inheritance you gave me.

A mis padres, Samuel y Silvia, no estaría logrando esto si no fuera por la educación que me dieron. Con su ejemplo aprendí cómo alcanzar la excelencia, deseo de aprender y tener metas siempre. Esa es la mejor herencia que he recibido de ustedes.

## Acknowledgements

I would like to start by expressing my deepest gratitude to my principal supervisor Professor Adrian Werner. The present thesis would not have been possible without his dedicated guidance and support. Adrian, I want to thank you for being so generous with your time; I highly appreciate it. I owe much to my co-supervisor Dr Dylan Irvine, his enthusiastic guidance throughout my PhD has been so motivating. Thank you, Dylan, for your advice on my oral presentations and your kind assistance with Python. I am deeply in debt to Dr Neville Robinson. Your valuable advice and generous guidance improved this thesis. I would like to thank Dr Vincent Post for his generous assistance with the PBC package.

A special thanks to my husband, Javier, and my children, Daniel, Diego, and Rebeca. You were my continuous motivation to accomplish this PhD. I do not have enough words to thank you, Javier. I could not have been able to achieve the work presented here without all your unwavering support, sacrifices and patience.

I thank and praise God, who has blessed me with His grace and sustained me throughout this PhD process.

Financial support for the PhD candidature was provided by the Australian Government through the Research Training Program Scholarship and is gratefully acknowledged.

I would like to express my gratitude to Prof. Peter Cook and Prof. Okke Batelaan, my internal examiners, for the kind acceptance to sit on my Final Thesis Review milestone. I also wish to thank Prof. Anirban Dhar and Prof. Torben Sonnenborg, my external examiners, for their kindness and patience in going through my thesis, their positive feedback has improved this thesis.

## Summary

Coastal aquifers are an integral source of freshwater supplying an increasing population, especially in coastal communities. Thus, understanding the groundwater dynamics in coastal zones is critical for the effective management of this precious freshwater resource. The study of coastal groundwater has the inherent complexity of the hydraulic connection of groundwater with the ocean. This thesis has selected three main complex processes involved in the fresh groundwater-ocean interaction that are not yet well understood: (1) the effects of dispersion in submarine aquifers caused by the mixing between subsea freshwater and seawater; (2) flow instabilities associated with mixed-convective processes induced by the occurrence of subsea fresh groundwater discharge through high-permeability seafloor sediments; and (3) the effects of tidal forces on groundwater levels in circular islands.

The first part of this study investigates the effects of dispersion in submarine freshwater distribution. It does so by comparing the Werner and Robinson (2018) analytical solution (i.e., the latest sharp-interface based analytical solution to offshore freshwater extent) with numerical model simulations, adding dispersion parameters. Results show that dispersion affects differently the interface tip position (i.e., where the interface intercepts the top of the aquifer) than it does to the interface toe (i.e., where the interface intercepts the bottom of the aquifer). The changes on the interface tip as well as on the interface width at the top of the aquifer caused by dispersion are dependent on the hydraulic characteristics of the submarine aquitard. This interdependence makes that the tip location and the interface width at the top of the aquifer have a non-monotonic relationship with increasing dispersion. Conversely, the submarine aquitard seems to have little influence at the bottom of the aquifer where both the toe location and the interface width have a monotonic relationship with dispersion, in a similar fashion to what it is observed in onshore aquifers. Additionally, our investigation shows that seawater circulation rates and submarine fresh groundwater rates increase with increasing dispersion, implying that heterogeneity causes larger groundwater fluxes to the ocean. We found that the effects of dispersion, especially in the submarine fresh groundwater discharge, are interrelated with the type of analytical case, showing larger changes in freshwater discharge with increasing dispersion in the analytical case associated with an onshore toe.

Our attempts to find a correction to the Werner and Robinson (2018) analytical solution to account for dispersion were not successful as a result of the complex interplay between dispersion, aquitard characteristics and the analytical case classification undertaken by the Werner and Robinson (2018) analytical solution. Nevertheless, this study provides insights into the controlling factors that can be considered when seeking dispersive correction coefficients for individual situations, such as individual correction factors for the tip and toe, as well as considering specific analytical cases.

The second part of this study investigates the subsea fresh groundwater discharge (SFGD) distribution through high-permeability seafloor sediments. Most studies related to predict offshore freshwater extent assume that low-permeability sediments protecting the submarine freshwater from overlying seawater intrusion are in direct contact with the ocean, implicitly assuming that SFGD is uniformly distributed. However, the distribution of SFGD through high-permeability sediments containing seawater is not well understood. This study demonstrates through variable-density and solute transport numerical modelling that mixed-convective processes govern the SFGD distribution through sandy seafloor sediments in the form of unstable buoyant freshwater fingers. Hence, mixed-convective theory, such as the non-dimensional Rayleigh number and mixed convection ratio, may be applied for the prediction of SFGD occurrence through high-permeability seafloor sediments. This investigation demonstrates that the temporality characteristic of unstable flow conditions in the form of permanent buoyant fingers is controlled by the lower boundary. This study is the initial step for further investigation to establish critical non-dimensional numbers to infer the occurrence of SFGD through high-permeability seafloor sediments.

The final part of this study investigates tidal propagation in circular islands. The aim is to determine the applicability of the widely used Ferris solution to tidal propagation, which is based on the assumption of a straight, infinite shoreline, in circular islands. The investigation is undertaken by comparing an existing analytical solution under radial flow conditions ('circular solution') with the Ferris solution. This comparison allowed us to obtain a correction factor to the Ferris solution to be applied in circular boundaries ('corrected Ferris solution'). The advantage of the corrected Ferris solution over the circular solution is its direct application for the inverse problem of inferring aquifer diffusivity, while the circular solution requires

iterative methods. This investigation demonstrates that the corrected Ferris solution and the circular solution predict within 1% and 2.5% of the known diffusivities for confined and unconfined conditions, respectively. This study contributes by extending the available tools to estimate aquifer parameters, especially in circular aquifers, facilitating the determination of properties that otherwise require more invasive methods such as pumping tests.

## List of Figures

<b>Figure 1.1</b>	Schematic of complex processes associated with coastal aquifers. Analytical solutions to the freshwater distribution in offshore aquifers adopt a sharp interface rather than the zone of dispersion shown in the figure. ....	1
<b>Figure 3.1</b>	Simplified cross section of a coastal aquifer extending offshore to the end of the continental shelf (i.e., the right vertical edge of the diagram) (adapted from Solórzano-Rivas and Werner, 2018). Dark blue represents seawater, where the zone with the pattern represents the saline part of the aquifer, light blue represents freshwater, dark brown is the onshore confining unit, and light brown is the offshore semi-confining unit (i.e., the aquitard). The vertical dashed line indicates the shoreline location. ....	13
<b>Figure 3.2</b>	Conceptual model to apply the Werner and Robinson (2018) sharp-interface solution (modified from Solórzano-Rivas and Werner, 2018). Colour lines denote the model input/output boundaries: blue for the inland freshwater boundary and red for the sea boundary. The vertical seaward boundary of the aquitard is a no-flow condition. The grey dashed line indicates the freshwater potential (which is higher than sea level due to density effects). ....	14
<b>Figure 3.3</b>	Contours of dimensionless toe location within a range $-2.0 \leq xT' \leq 1.5$ , as a function of $\mu$ and $\lambda_s$ for a constant value of $\beta H/H_l = 0.1$ (adapted from Werner and Robinson, 2018). Red lines demarcate the separation of Analytical cases I to IV. ....	16
<b>Figure 3.4</b>	Schematic of the variables used to describe the results of dispersive subsea aquifer simulations. Light blue and dark blue arrows represent the inflow/outflow of groundwater with salinity (relative to seawater) of $<50\%$ and $>50\%$ , respectively. Arrows lengths do not infer the rates of inflow and outflow. Pink and cyan shaded areas represent the onshore and offshore aquifers, respectively. Contour labels are salinities relative to seawater... ..	23
<b>Figure 3.5</b>	Steady-state locations of the 0.5 isochlor (50% seawater salinity) for the five scenarios (see Table 3.1), where panels (a) to (e) are Scenarios 1 to 5, respectively. Tip and toe locations from each simulation are given in the left column of graphs, while interface shapes are shown in the right column. The parameterisation of $\alpha_L$ is depicted by the colour of symbols and lines. Grey lines and symbols represent the sharp-interface solution, and the pink and cyan shaded areas identify the onshore and offshore domains, respectively. ....	27
<b>Figure 3.6</b>	Dimensionless mixing zone widths at the tip ( $W'_{tip}$ ) and toe ( $W'_{toe}$ ) for different values of dispersivity. The effects of changing the $K:K_z$ contrast is demonstrated by differences in subfigures (a) to (e), which represent Scenarios 1 to 5 (the $K:K_z$ ratio is shown in each subfigure), respectively. ....	31
<b>Figure 3.7</b>	Freshwater discharge deviation ( $\Delta Q_f$ ) attributable to dispersion effects, i.e., as a function of dimensionless dispersivity. Positive values of $\Delta Q_f$ indicate that the numerically derived freshwater flux is larger than the corresponding analytically derived freshwater flux. ... ..	33
<b>Figure 3.8</b>	Dimensionless seawater circulation rates ( $SC$ ) versus dimensionless dispersivity (given in terms of $\alpha T/H$ ). Curves are labelled with the analytical, sharp-interface value of $\mu$ , showing that the vertical sequencing of the curves is correlated to $\mu$ (i.e., $\mu$ increases from top to bottom). ....	34
<b>Figure 3.9</b>	$Ra_\delta$ values versus dimensionless dispersivity. ....	35

<b>Figure 3.10</b>	$Ra^*$ values versus dimensionless dispersivity.....	36
<b>Figure 4.1</b>	Two conceptual models of a subsea unconfined aquifer subject to SFGD. Blue is freshwater, and purple is seawater. Model A (left) involves sandy sediments overlying a subcropping, higher-permeability aquifer, and Model B represents an aquitard overlain by sand. ....	50
<b>Figure 4.2</b>	Conceptual models for the numerical implementation of SFGD through an unconfined subsea aquifer, where the left side shows sandy sediments overlying a subcropping, higher-permeability aquifer, and Model B represents an aquitard overlain by sand. Red and blue represent seawater and freshwater boundary conditions, respectively. The equivalent freshwater head at the base of the aquifer, when the aquifer is seawater-filled (i.e., the initial condition), is shown as $h_f$ . ....	57
<b>Figure 4.3</b>	Salinity distributions in seafloor sediments obtained from simulations of the Base Case (i.e., $\alpha_L = 0.1$ m; $\alpha_T = 0.01$ m) of Model A (left column) and Model B (right- column). Concentration values represent the relative seawater concentration, where 0 and 1 are freshwater and seawater, respectively. The bottom left subplot depicts steady state results, while the bottom right subplot shows a quasi-steady state salinity distribution. ....	60
<b>Figure 4.4</b>	Salinity distributions in seafloor sediments obtained from simulations of Case 1 (i.e., $\alpha_L = 0.5$ m; $\alpha_T = 0.05$ m) of Model A (left column) and Model B (right column). Concentration values represent the relative seawater concentration, where 0 and 1 are freshwater and seawater, respectively. The bottom left subplot depicts steady-state results, while the bottom right subplot shows a quasi-steady state salinity distribution. ....	61
<b>Figure 4.5</b>	Salinity distribution in seafloor sediments obtained from simulations of Case 2 (i.e., $\alpha_L = 1$ m; $\alpha_T = 0.1$ m) of Model A (left column) and Model B (right column). Concentration values represent the relative seawater concentration, where 0 and 1 are freshwater and seawater, respectively. The bottom left subplot depicts steady-state results, while the bottom right subplot shows a quasi-steady state salinity distribution.....	62
<b>Figure 4.6</b>	Numerical model results of total solute mass with time. (a) and (d) Base Case (i.e., $\alpha_L = 0.1$ m; $\alpha_T = 0.01$ m); (b) and (e) Case 1 (i.e., $\alpha_L = 0.5$ m; $\alpha_T = 0.05$ m); and (c) and (f) Case 2 (i.e., $\alpha_L = 1$ m; $\alpha_T = 0.1$ m). The left column represents cases of Model A and the right column represents cases of Model B. ....	64
<b>Figure 4.7</b>	Salinity distribution in profile (subplots (a) to (c); top row) and temporal variation of solute concentration (subplots (d) to (f); bottom row) in seafloor sediments obtained from Model B simulations: Subplots are (from left to right) the Base Case, Case 1 and Case 2. Concentration values represent the relative seawater concentration, where 0 and 1 are freshwater and seawater, respectively. All subplots show a quasi-steady state salinity distribution. ....	66
<b>Figure 5.1</b>	Conceptual model of a circular island subjected to tidal forcing at the shoreline, where $b$ is the aquifer thickness, $r$ is the radial distance from the centre of the island, and $a$ is the island radius.....	72
<b>Figure 5.2</b>	Results for the propagation of groundwater tides within a circular island of radius $a = 500$ m showing the match between the circular-island analytical solution (solid lines) and numerical modelling (symbols). Comparisons are given for: (a) hydraulic head oscillations at three locations, (b) tidal efficiency variation with $r$ , and (c) phase variation with $r$ . Red dashed lines in (b) and (c) represent the absolute differences in amplitude ( $ A_{gn} - A_g $ ) and phase ( $ \varphi_n -$	

$\varphi )$ , respectively. Note that $a - r = 0$ represents the shoreline and $r = 0$ represents the island centre. The subscript “n” indicates the numerical solution results.....	78
<b>Figure 5.3</b> Comparison of Ferris (dashed lines) and circular-island (solid lines) solutions in terms of the tidal efficiency with distance from the island coastline. Results are given for an island of size $a = 500$ m and considering four different $\alpha$ values. Note that $a - r = 0$ represents the shoreline and $a - r = 500$ represents the island centre.....	80
<b>Figure 5.4</b> Comparison of $\varphi$ estimated with the Ferris (dashed lines) and circular-island (solid lines) solutions with distance from the shoreline for an island of $a = 500$ m and four values of $\alpha$ . Dashed lines are entirely obscured by solid lines in the lower plots (i.e., $\alpha = 250$ and $2500$ m <sup>2</sup> /d). Note that $a - r = 0$ represents the shoreline and $a - r = 500$ represents the island centre. ....	81
<b>Figure 5.5</b> Spatial distribution of $AgFAg$ (left column; (a) to (d)) and $\varphi F\varphi$ (right column; (e) to (h)) for island radii ( $a$ ) between 50 and 2000 m (a total of 976 island radii were used in creating Figure 5.5) for four different $\alpha$ values. $r' = 0$ represents the shoreline and $r' = 1$ the centre of the island. The grey shading indicates where $A_g \leq 1$ cm. Solid lines represent points of equal $AgFAg$ ratio.....	82
<b>Figure 6.1</b> Schematic of the conceptual model adopted by the circular solution (i.e., confined conditions), showing a vertical cross section of a circular island subjected to tidal forcing at the shoreline (i.e., ocean tide), where $r$ is the radial distance from the centre of the island, and $a$ is the island radius. The monitoring well within the aquifer allows for observations of tidal groundwater heads. ....	91
<b>Figure 6.2</b> Two examples of synthetic groundwater tides, representing a distance from the shoreline equal to $0.2a$ , for the $\lambda_1$ -scenario (i.e., $\lambda = 150,000$ m <sup>2</sup> /d). The green line represents theoretical observations and the blue line shows theoretical observations with noise. Groundwater levels are relative to mean sea level. ....	96
<b>Figure 6.3</b> Schema of input data for the application of the circular solution and the corrected Ferris solution in the estimation of $\lambda$ for both confined and unconfined aquifer conditions..	102
<b>Figure 6.4</b> Comparison of $ E_r $ for estimated values of $\lambda_A$ , $\lambda_\varphi$ , $\lambda_{A,\varphi}$ and $\lambda_{av}$ for the three $\lambda$ -scenarios, derived from the theoretical observations with noise and applying the circular solution. Grey dashed line represents $ E_r  = 0.6\%$ . ....	110
<b>Figure 6.5</b> Comparison of $ E_r $ for estimated values of $\lambda_A$ , $\lambda_\varphi$ , $\lambda_{A,\varphi}$ and $\lambda_{av}$ for the $K_1$ constituent, three $\lambda$ -scenarios, derived from the numerical observations (left column) and numerical observations with noise (right column) and applying the circular solution. Grey dashed line represents $ E_r  = 2.5\%$ . ....	111
<b>Figure 6.6</b> Comparison of $ E_r $ for estimated values of $\lambda_{AF}$ , $\lambda_{\varphi F}$ and $\lambda_{avF}$ for the three $\lambda$ -scenarios, derived from theoretical observations (i.e., without noise) and applying the corrected Ferris solution. Grey dashed line represents $ E_r  = 0.4\%$ . ....	114
<b>Figure 6.7</b> Comparison of $ E_r $ for estimated values of $\lambda_{AF}$ , $\lambda_{\varphi F}$ , and $\lambda_{avF}$ for the three $\lambda$ -scenarios, derived from theoretical observations with noise and applying the corrected Ferris solution. Grey dashed line represents $ E_r  = 1\%$ . ....	115
<b>Figure 6.8</b> Comparison of $ E_r $ for estimated values of $\lambda_{AF}$ , $\lambda_{\varphi F}$ , and $\lambda_{avF}$ for the three $\lambda$ -scenarios, derived from numerical observations and numerical observations with noise, applying the corrected Ferris solution. Grey dashed line represents $ E_r  = 2.5\%$ . ....	117

## List of Tables

<b>Table 3.1</b> Model parameters for five offshore aquifer scenarios (see Figure 3.2 for a pictorial representation of geometric parameters). .....	20
<b>Table 3.2</b> Dimensionless sensitivities ( $S_{tip}$ and $S_{toe}$ ) describing changes in the tip and toe with changes to $\alpha_L$ (indicated by the shaded numbers) in the five scenarios described in Table 2.1. Negative values of $S_{tip}$ indicate that increasing $\alpha_L$ causes a decrease in $x_{tip}$ , otherwise $x_{tip}$ increases with $\alpha_L$ . $x_{toe}$ increased with $\alpha_L$ in all cases, and therefore negative $S_{toe}$ values indicate that $x_{toe}$ is onshore. ....	29
<b>Table 3.3</b> Effects of the seafloor boundary condition (where (a) represents flow direction-dependent salt mass flux, and (b) represents fixed concentration; see Section 3.3.2) on dispersive ( $\alpha_L = 1$ m and $\alpha_L = 20$ m) and non-dispersive numerical solutions ( $\alpha_L = 0$ m) for Scenarios 2 and 4. ....	37
<b>Table 3.4</b> Values of $V^*$ , $\mu$ and $SC$ for each scenario, where values of $l_f$ are constant .....	42
<b>Table 6.1</b> Amplitudes ( $A_0$ ), periods ( $\tau$ ) and frequencies ( $f$ ) of the constituents forming the synthetic tides of the current study. ....	93
<b>Table 6.2</b> Comparison of parameters obtained from harmonic analysis of theoretical observations and of theoretical observations with noise under confined conditions. Signals that have moved into the next tidal cycle are denoted by *. Results based on amplitudes smaller than 2.5 cm (i.e., within the limits of measurement techniques) are denoted by †. ....	103
<b>Table 6.3</b> Parameters obtained from the harmonic analysis of numerical observations for unconfined conditions ( $A_{n,obs}$ and $\varphi_{n,obs}$ ) for the $K_1$ constituent, and their respective relative errors. Amplitude values smaller than 2.5 cm are denoted by †. ....	105
<b>Table 6.4</b> Sensitivity ( $S_A$ ) of $\lambda_A$ to changes in $A_{g,obs}$ for $\delta = 0.5\%*$ .....	106
<b>Table 6.5</b> Sensitivity ( $S_\varphi$ ) of $\lambda_\varphi$ to changes in $\varphi_{obs}$ for $\delta = 0.5\%*$ . Scenarios leading to phase lags greater than one tidal cycle are denoted by ‡. ....	106
<b>Table 6.6</b> $\lambda$ estimates ( $\lambda_A$ , $\lambda_\varphi$ and $\lambda_{A,\varphi}$ ) from theoretical observations with noise ( $A'_{g,obs}$ and $\varphi'_{obs}$ ) for the three $\lambda$ -scenarios, obtained by minimisation of equations (6.13) to (6.15). $\lambda_{av}$ is the average of $\lambda_A$ and $\lambda_\varphi$ . Note that at the inland distance of $0.3a$ for the $MK_3$ constituent, $\lambda_1$ -scenario, the $\lambda_\varphi$ estimate did not require the cycle correction mentioned in Section 6.4.1, even though the transpired phase lag is greater than $2\pi$ . ....	108

# Chapter 1

## Technical terminology

This chapter briefly describes the technical terminology associated with the processes involved in coastal aquifers due their interconnection with the ocean. Figure 1.1 summarizes the three process that were investigated in this thesis. Note that the processes illustrated in Figure 1.1 have been individually studied. For example, the study of subsea fresh groundwater discharge (SFGD) distribution through seafloor sediments (process 2) did not include the effect of tidal propagation (process 3).

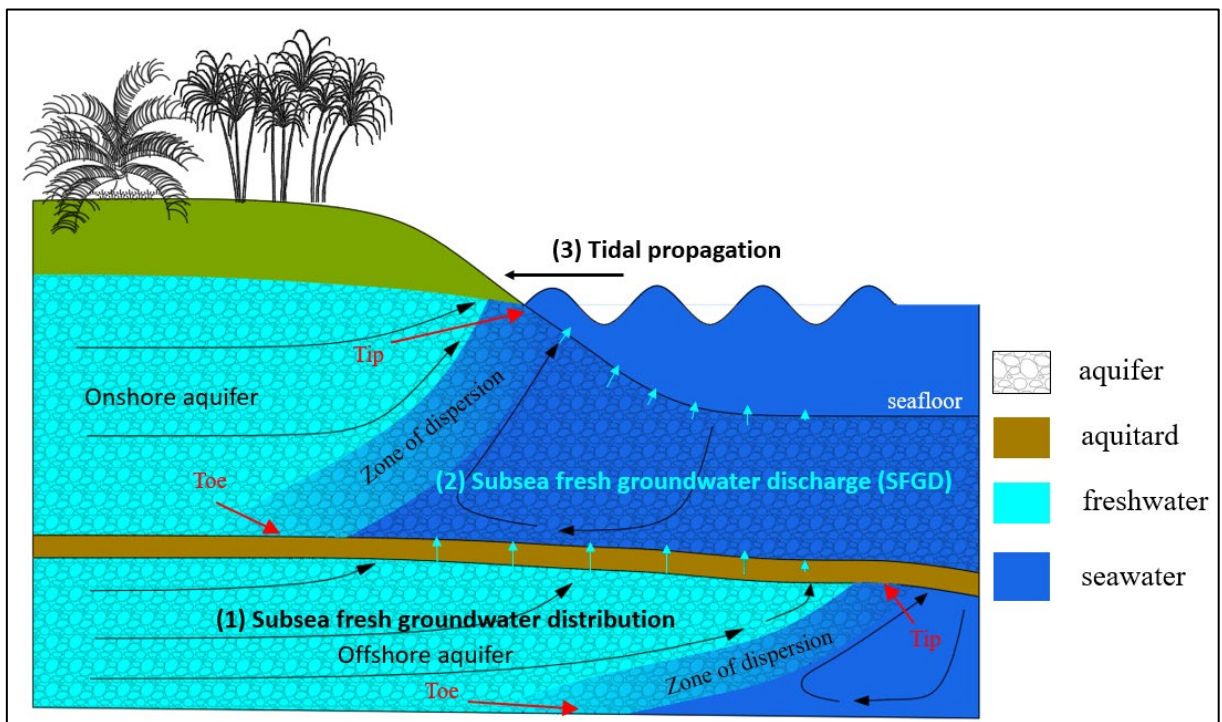


**Figure 1.1** Schematic of complex processes associated with coastal aquifers. Analytical solutions to the freshwater distribution in offshore aquifers adopt a sharp interface rather than the zone of dispersion shown in the figure.

The important terms from Figure 1.1 are described below:

**Dispersion**

Spread of individual particle velocities from the calculated seepage velocity induced by pore-scale heterogeneity (i.e., microscopic dispersion) or field-scale heterogeneity (i.e., macroscopic dispersion) (e.g., Zheng and Bennett, 2002). In this thesis, only the influence of macroscopic dispersion in submarine aquifers has been investigated. Dispersion, the short name for hydrodynamic dispersion [ $L^2 T^{-1}$ ], is the sum of mechanical dispersion, which is associated with changes in fluid velocity; and molecular diffusion, which is associated to the particle movement independent of fluid velocity and caused by the existence of a solute concentration gradient (e.g., Zheng and Bennett, 2002). In numerical models of groundwater flow and variable density solute transport, mechanical dispersion is simulated by multiplying dispersivity parameters (i.e., longitudinal and transverse dispersivities [ $L$ ]) with velocity vectors [ $L T^{-1}$ ]; and molecular diffusion is accounted for adopting an effective molecular diffusion coefficient [ $L^2 T^{-1}$ ].

**Zone of dispersion**

Zone of gradually varying salinity between freshwater and seawater (e.g., Jiao and Post, 2019).

**Sharp interface**

Clear separation between freshwater and seawater without a transition zone (e.g., Jiao and Post, 2019). Many analytical solutions make the sharp interface assumption (e.g. Werner et al., 2012; Werner and Robinson, 2018). These models ignore the effects of dispersion.

**Tip**

The freshwater-seawater interface end that intercepts the top of the aquifer.

**Toe**

The freshwater-seawater interface end that intercepts the bottom of the aquifer.

**Onshore aquifer**

Terrestrial permeable sediments containing fresh groundwater.

**Offshore aquifer**

Permeable continental shelves containing low-salinity groundwater (e.g., Post et al., 2013).

**M<sub>2</sub>**

Largest semidiurnal lunar harmonic constituent with a period of 12.42 hours.

**S<sub>2</sub>**

Main solar semidiurnal tidal constituent with a period of 12 hours.

**N<sub>2</sub>**

Larger lunar elliptic semidiurnal tidal constituent with a period of 12.66 hours.

**K<sub>1</sub>**

Lunar-solar diurnal tidal constituent with a period of 23.93 hours.

**O<sub>1</sub>**

Principal lunar diurnal tidal constituent with a period of 25.82 hours.

**K<sub>2</sub>**

Luni-solar semidiurnal constituent with a period of 11.97 hours.

**P<sub>1</sub>**

Principal solar diurnal tidal constituent with a period of 24.07 hours.

**MK<sub>3</sub>**

Tidal constituent that arises from the combination of M<sub>2</sub> and K<sub>1</sub> when they pass through shallow-water depths (e.g., Luick, 2004) with a period of 8.18 hours.

# Chapter 2

## Introduction

### 2.1 Research problem

Groundwater systems in coastal aquifers are typified as highly complex groundwater systems in relation to their inland counterparts (e.g., Custodio, 1987). Groundwater-ocean interactions involve complex processes that affect the dynamics of groundwater flow in coastal aquifers. Complex processes in coastal aquifers include (1) mixing between freshwater and seawater identified by a transition or mixing zone controlled by dispersion mechanisms; (2) unstable convective flow arising from water density gradients between freshwater and seawater; (3) the propagation of ocean tides into groundwater levels, which is governed by the aquifer hydrogeological properties (e.g., Custodio, 1987; Werner et al., 2013; Jiao and Post, 2019). Despite the study of these complexities have attracted significant scientific attention, there remain some aquifer-ocean settings that are poorly understood.

While the role of dispersion in the freshwater distribution in onshore aquifers is understood, the role of dispersion in offshore aquifers has not been widely studied. Dispersion controls the freshwater extent in coastal aquifers, both onshore and offshore, creating a mixing zone (i.e., a dispersive interface). However, sharp-interface models that assume stagnant seawater conditions and no formation of the mixing zone are commonly applied to estimate the freshwater distribution (i.e., the extent of seawater intrusion) (e.g., Werner et al., 2012). Cooper (1964) demonstrated that by adopting sharp-interface models, the freshwater extent in onshore aquifers is underestimated relative to more realistic dispersive models. In sharp-interface models, the toe location is estimated to be located further landward than a dispersive model predicts. Sharp-interface models in onshore aquifers typically assume that the tip is fixed at the shoreline or intertidal zone, for which the freshwater extent is quantified only by the toe location (e.g., Werner et al., 2012). The assumption of a fixed tip location close to the shoreline cannot be translated to offshore aquifers, where the fresh groundwater discharge can extend well beyond the intertidal zone, defining the tip location. Hence, the freshwater distribution in

offshore aquifers is determined not only by the toe location (as in onshore aquifers) but also by how far from the shoreline the tip occurs. Whether dispersion mechanisms affect the tip location in the same fashion as that described for the toe location has not been investigated in detail. Thus, the role of dispersion in the submarine freshwater distribution and other associated processes remains unclear.

Fresh groundwater discharge beyond the intertidal zone usually requires the existence of an overlying low-permeability layer to preserve the occurrence of offshore fresh groundwater, that would otherwise occur near the shoreline (e.g., Jiao et al., 2015; Michael et al., 2016). Analytical solutions to determine the offshore extent of freshwater typically assume that the low-permeability layer is in direct contact with the ocean (e.g., Werner and Robinson, 2018;), whereas seafloor sediments are commonly comprised by high-permeability layers (e.g., Riedl et al., 1972). The conceptual model adopting high-permeability sediments in contact with the ocean provides an alternative to the typically assumed case where uniformly distributed subsea fresh groundwater discharges to the sea through low-permeability seafloor sediments (e.g., Taniguchi et al., 2003; Michael et al., 2003). A discharge pattern to the seafloor associated with unstable flow conditions, rather than a uniformly distributed pattern, is anticipated when fresh groundwater discharge occurs through high-permeability sediments that are overlain by seawater.

Unstable flow conditions are associated with the configuration of a dense fluid overlying a less dense fluid in high-permeability sediments (Simmons et al., 2010). Under these unstable flow conditions in the context of submarine groundwater flow, mixed-convective processes will govern the flow distribution. In a subsea setting, fresh groundwater flow will be driven by the combination of buoyancy and hydraulic forces. Although mixed-convective flow processes have been comprehensively studied for the scenarios of downward moving, high-density solute plumes (e.g., Stevens et al., 2009; Xie et al., 2011), the flow distribution caused by buoyant low-concentration (i.e., freshwater) plumes is still not well understood. Understanding the subsea fresh groundwater discharge distribution involves significant implications to its measurement (e.g., seepage meters distribution), which is of particular importance to scientific fields related to the understanding of seafloor ecosystems. Thus, an insight into the main

controlling factors of subsea fresh groundwater discharge through high-permeability seafloor sediments is warranted.

Aquifer hydrogeological characterisation is an integral aspect of groundwater management, and is particularly important in island aquifers, where freshwater lenses are often the main source of freshwater (e.g., Werner et al., 2017). Thus, quantification of hydraulic parameters is vital to better understand these water resources. Ferris (1951) provided the first methodology (hereafter "Ferris solution") to estimate aquifer hydraulic characteristics that are integrated over significant distances, based on tidal propagation. Aquifer diffusivity (i.e., the ratio of hydraulic conductivity and specific storage, or its equivalent, transmissivity over storativity) is the hydraulic characteristic that controls the delay and attenuation of ocean tides on groundwater levels as they penetrate inland. The fact that groundwater data in coastal aquifers are often readily accessible (i.e., data from observation bores) makes the application of analytical solutions to tidal propagation an attractive tool to estimate aquifer diffusivities. For example, the Ferris solution has been widely applied for the estimation of aquifer diffusivity, including islands (e.g., Banerjee et al., 2008; Chattopadhyay et al., 2014). However, the underlying assumptions of the Ferris solution, including an infinite straight shoreline and an infinite aquifer length perpendicular to the shoreline, pose a limitation for coastal aquifers, especially islands. Hence, the application of the Ferris solution to islands requires further investigation.

## **2.2 Research objectives**

This PhD investigates three complex processes in coastal aquifers: (1) Dispersion in offshore aquifers; (2) convection processes in seafloor sediments; and (3) tidal propagation in coastal aquifers. The objectives of this PhD are to address the knowledge gaps identified in the previous section that are associated with those three groundwater processes characteristic of coastal aquifers. These three processes are investigated across four separate bodies of research, that:

- (a) determine the role of dispersion in the freshwater distribution, freshwater discharge and width of the mixing zone in offshore aquifers;
- (b) identify the controlling factors in the subsea fresh groundwater discharge distribution through high-permeability seafloor sediments;

- (c) ascertain the applicability of a straight shoreline based analytical solution to tidal propagation in aquifers of orbiculate shape; and
- (d) determine the applicability of the analytical solutions studied in (c) for the inverse problem of estimating aquifer diffusivity.

## **2.3 Thesis organisation**

This thesis is arranged into seven chapters, including this Introduction chapter (Chapter 2). Chapter 1 introduces some of the technical terms utilised in this thesis. Chapters 3 through 6 correspond precisely to four journal article manuscripts, two of which are already published (Chapters 3 and 5), and the other two (Chapters 4 and 6) are currently under review. Each chapter can, therefore, be read independently. A brief summary of each chapter is provided below.

Chapter 1 pictorially summarises the three coastal processes investigated in this thesis. Chapter 1 also defines some of the technical terms highly utilised in this thesis.

Chapter 3 investigates the role of dispersion in offshore aquifers. Numerical model simulations are undertaken in SEAWAT, adding dispersion parameters to the conceptual model adopted by the sharp-interface, Werner and Robinson (2018) analytical solution. A comparison between the dispersive numerical model results and the sharp-interface analytical solution provides insight into the dispersion impact on offshore groundwater flow. The Werner and Robinson (2018) analytical solution is the latest methodology that quantifies the offshore freshwater extent.

Chapter 4 explores the controlling factors in the distribution of subsea freshwater discharge. The study includes a review of the existing non-dimensional numbers applied to unstable groundwater flow. The aim of this chapter is to explore whether this buoyancy theory (i.e., non-dimensional numbers) widely applied to the occurrence of downward, high-density solute plumes can equally be applied to the occurrence of upward freshwater plumes. This study suggests that such a pattern of upward freshwater plumes will dominate the subsea fresh

groundwater discharge in cases where high-permeability seafloor sediments are in direct contact with the ocean.

Chapter 5 develops a comparison between two analytical solutions to tidal propagation, the straight-shoreline based Ferris solution and an existing radial-flow based ("circular") analytical solution. Such a comparison gives rise to a correction factor to the more straightforward to apply Ferris solution so that it can be applied to orbiculate aquifer boundaries. The study also compares the circular analytical solution to numerical experiments. This is the first study to simulate tidal propagation using the axisymmetric correction proposed by Langevin (2008) and the modified version of SEAWAT by (Post, 2011).

Chapter 6 explores the application of the circular analytical solution and the correction factor to the Ferris solution, proposed in Chapter 5, for the inverse calculation of estimating aquifer diffusivities. The study applies synthetic tidal hydrographs with random noise imposed as observed groundwater tides. This chapter also explores the application of both solutions (devised for confined conditions) to estimate aquifer diffusivities in unconfined conditions.

Chapter 7 provides an overall summary of the main results and conclusions of this thesis.

## Chapter 3

### Dispersion effects on the freshwater-seawater interface in subsea aquifers

Accepted for publication in *Advances in Water Resources*: Solórzano-Rivas, S. C., Werner, A. D., Irvine, D. J. Dispersion effects on the freshwater-seawater interface in subsea aquifers. *Advances in Water Resources*, 130, 184-197. doi:10.1016/j.advwatres.2019.05.022.

*Approximate contribution of co-authors: S.C. Solórzano-Rivas (65%); Adrian Werner (25%); Dylan Irvine (10%).*

#### 3.1 Abstract

Recent recognition of the widespread occurrence of freshwater beneath the ocean has renewed interest in approaches to understand and predict its extent. The most straightforward methodologies are based on the sharp-interface approximation, which neglects dispersive mechanisms. The understanding of dispersion effects on freshwater extents in coastal aquifers is based almost entirely on onshore aquifer situations. This study explores dispersion in offshore coastal aquifers, in terms of the steady-state freshwater extent, seawater circulation and freshwater discharge, through numerical experimentation. Results show that increasing dispersion causes a seaward shift in the interface toe location, as expected, whereas the interface tip shows a non-monotonic relationship with dispersion that depends on the contrast between aquifer and aquitard hydraulic conductivities. Higher dispersion leads to enhanced seawater recirculation rates and freshwater discharge, as opposed to non-monotonic relationships obtained previously for onshore aquifers. The mixing zone at the toe widens as dispersion increases, similar to onshore cases, whereas the mixing zone at the tip has a surprisingly non-monotonic relationship with dispersion. The dispersion relationships revealed in this study can be explained by counteractions between dispersion, density and advective forces, and refraction across the aquifer-aquitard interface, which in combination produce offshore aquifer behaviour that differs, in some ways, to the manner in which onshore aquifers respond to dispersive processes. Consequently, previous empirical corrections to sharp-interface methods (to account for dispersive effects) applied to onshore coastal aquifers are ineffective in their application to offshore settings.

## 3.2 Introduction

The discovery of widespread fresh groundwater in continental shelves (e.g., Post et al., 2013) has promoted a renewed interest in methods to quantify the extent of these resources. The development of simplified methodologies is particularly relevant to subsea freshwater estimation because offshore data are usually scarce and rapid approximations are critical first steps in recognising the potential for offshore freshwater reserves. For example, Solórzano-Rivas and Werner (2018) employed simplified conceptual models of offshore aquifers in their numerical modelling study of subsea freshwater extents, and proposed an approximate method for simulating the offshore sea boundary condition using the General Head Boundary package of SEAWAT (Langevin et al., 2008). They recommended revision of analytical solutions to the extent of offshore fresh groundwater, developed by Bakker (2006) and Bakker et al. (2017), to allow for alternative salinity assumptions in the offshore aquitard. Werner and Robinson (2018) subsequently developed this revision, and Knight et al. (2018) applied it to the rapid assessment of numerous offshore aquifers from around the world.

The above analytical methods are based on assumptions that there is no mixing between freshwater and seawater (i.e., a sharp interface), and that seawater is stagnant rather than the circulating behaviour that is found in onshore coastal aquifer settings (e.g., Smith, 2004). Studies have shown that the seawater extent in coastal aquifers is overestimated by sharp-interface methods (e.g., Cooper et al., 1964; Volker and Rushton, 1982). However, sharp-interface methods overestimate the extent of freshwater lenses for variable-density situations in riverine riparian zones (Werner, 2017a), and therefore, neglecting dispersion may lead to over- or underestimation of fresh groundwater bodies in variable-density systems.

The extent of seawater in coastal aquifers is commonly quantified by the interface toe location, i.e., where the interface intercepts the bottom of the aquifer (e.g., Volker and Rushton, 1982; Werner and Simmons, 2009). While the toe location typically indicates the most landward advancement of seawater, at least in homogeneous aquifers, the tip location (i.e., where the interface intercepts the top of the aquifer), usually reflects the maximum offshore extent of freshwater penetration. This is an important additional consideration in studies concerned with the storage of freshwater beneath the seafloor. The best known and studied cases of terrestrial

discharge into the sea occur within the intertidal zone (e.g., Reilly and Goodman, 1985; Bear et al., 1999), thereby presuming that the tip is effectively connected to, or near to, the shoreline. Consequently, the current understanding of the key factors (in particular, the role of dispersion) influencing the tip position, and by association the offshore extent of freshwater, is somewhat deficient.

Although extensive research has been carried out to assess the impact of neglecting dispersion in sharp-interface models of onshore aquifers (e.g., Cooper et al., 1964; Pool and Carrera, 2011; Llopis-Albert and Pulido-Velazquez, 2014; Werner, 2017b), only Hill (1988) has considered the effect of dispersion on the distribution of subsea freshwater. Hill (1988) compared sharp-interface and dispersive-interface solutions to the freshwater-seawater distribution in a case-study investigation of a layered, offshore aquifer setting (Cape May County, New Jersey). Hill (1988) evaluated the freshwater extent in three aquifers with intervening aquitards (an unconfined aquifer overlying two semi-confined aquifers), extending offshore some 22 km. Hill (1988) compared Essaid's (1986) sharp-interface numerical solution to dispersive numerical results for the stratified-aquifer system. The results showed that the tip and toe of the dispersive mixing zone were considerably more seaward than the sharp-interface solution in the upper- and lowermost aquifers, whereas in the middle aquifer, the sharp interface occurred within the numerical mixing zone, albeit differing in slope relative to the dispersive mixing zone. Hill (1988) attributed the sharp/dispersive interface mismatch within the upper- and lowermost aquifers to differences in inter-aquifer freshwater flow exchange between the sharp-interface and dispersive methods. That is, while the dispersive solution treated inter-aquifer exchange using standard flow and transport equations, Essaid's (1986) solution required special treatment of upward freshwater leakage where it flowed into saltwater in the overlying aquifer. Hill (1988) found that Essaid's (1986) method caused overestimation of the seawater extent, as Mehdizadeh et al. (2014) later confirmed. Hill (1988) also reported that dispersive results better matched sharp-interface estimates with lower transverse dispersivity ( $\alpha_T$ ), although supporting evidence for this outcome was not presented.

Given that Hill's (1988) analysis of offshore dispersive effects was confounded by Essaid's (1986) assumption of inter-aquifer freshwater exchange, and the effect of dispersion was not systematically investigated, a more thorough analysis of the role of dispersion on offshore

salinity distributions, including on both the toe and tip locations, is warranted. Furthermore, the influence of dispersion on estimates of freshwater discharge and on rates of seawater circulation in offshore aquifers should also be assessed. In this regard, this study is the first to investigate the effect of dispersion on freshwater discharge to, and within, offshore aquifers, when inland boundary conditions are specified by fixed heads rather than fixed fluxes.

Thus, the main aim of this study is to explore the role of dispersion in influencing the key features of offshore freshwater-seawater relationships, including the characteristics of the freshwater-seawater interface (e.g., the tip and toe location, and the mixing zone width), rates of freshwater discharge, and seawater circulation rates. Intentionally simplified offshore aquifer settings are considered, in the form of cross-sectional models of uniform geometry and homogeneous, isotropic hydraulic properties. This allows for comparison to the Werner and Robinson (2018) solution for the sharp-interface position, and assists in elucidating generalised behaviour that would otherwise be challenging to discern using more complicated situations. We extend the research of Solórzano-Rivas and Werner (2018), who studied steady-state salinity distributions in subsea aquifer-aquitard systems without accounting for dispersion (i.e., based on the sharp-interface assumption). The dispersion-independent form of the boundary Rayleigh number considered by Solórzano-Rivas and Werner (2018) is revisited for dispersive situations. Additionally, the study of largely onshore seawater recirculation by Smith (2004) is re-examined for offshore conditions.

### **3.3 Methods**

#### **3.3.1 Analytical solution**

The Werner and Robinson (2018) solution is used here to provide exact distributions of the offshore freshwater-seawater interface under steady-state sharp-interface conditions. The conceptual model used by Werner and Robinson (2018) and others (e.g., Bakker, 2006; Bakker et al., 2017; Solórzano-Rivas and Werner, 2018) for the offshore continuation of continental fresh groundwater is illustrated in Figure 3.1. This two-dimensional, cross-sectional conceptual model is based on the assumption of one-dimensional flow (i.e., the Dupuit approximation) within an offshore aquifer that is homogeneous and isotropic. Freshwater and seawater are immiscible and separated by a sharp interface.

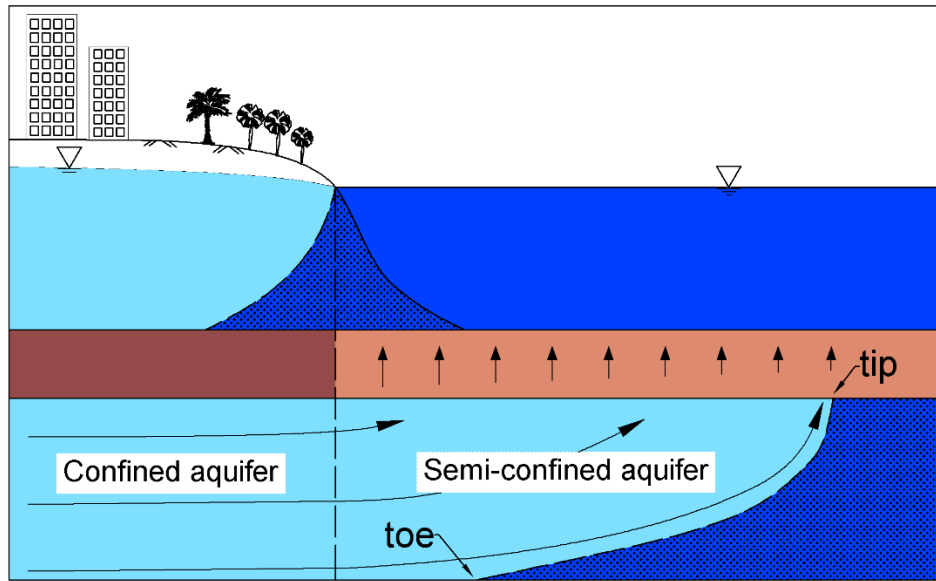


**Figure 3.1** Simplified cross section of a coastal aquifer extending offshore to the end of the continental shelf (i.e., the right vertical edge of the diagram) (adapted from Solórzano-Rivas and Werner, 2018). Dark blue represents seawater, where the zone with the pattern represents the saline part of the aquifer, light blue represents freshwater, dark brown is the onshore confining unit, and light brown is the offshore semi-confining unit (i.e., the aquitard). The vertical dashed line indicates the shoreline location.

Solórzano-Rivas and Werner (2018) compared non-dispersive numerical solutions against the Bakker (2006) and Bakker et al. (2017) analytical solutions, demonstrating that the analytical solution overestimated the extent of offshore fresh groundwater (at the top of the aquifer) due to the presumption by Bakker (2006) that the offshore aquitard was filled entirely with seawater. Solórzano-Rivas and Werner (2018) concluded that if the aquitard, in areas overlying fresh groundwater, is assumed to contain freshwater instead of seawater, the analytical solution would give better results. Based on Solórzano-Rivas and Werner (2018) findings, Werner and Robinson (2018) developed a solution that allows the aquitard salinity to be specified, confirming that when freshwater is assumed in the aquitard, the analytical solution and the non-dispersive numerical solution are in better agreement. For example, Werner and Robinson (2018) report an improvement in the analytically derived tip location from an average discrepancy of 87% (with the non-dispersive numerical results) when adopting seawater in the aquitard, to only 2% when the salinity was changed to that of freshwater. Some of the input parameters to apply the Werner and Robinson (2018) solution are illustrated in Figure 3.2.

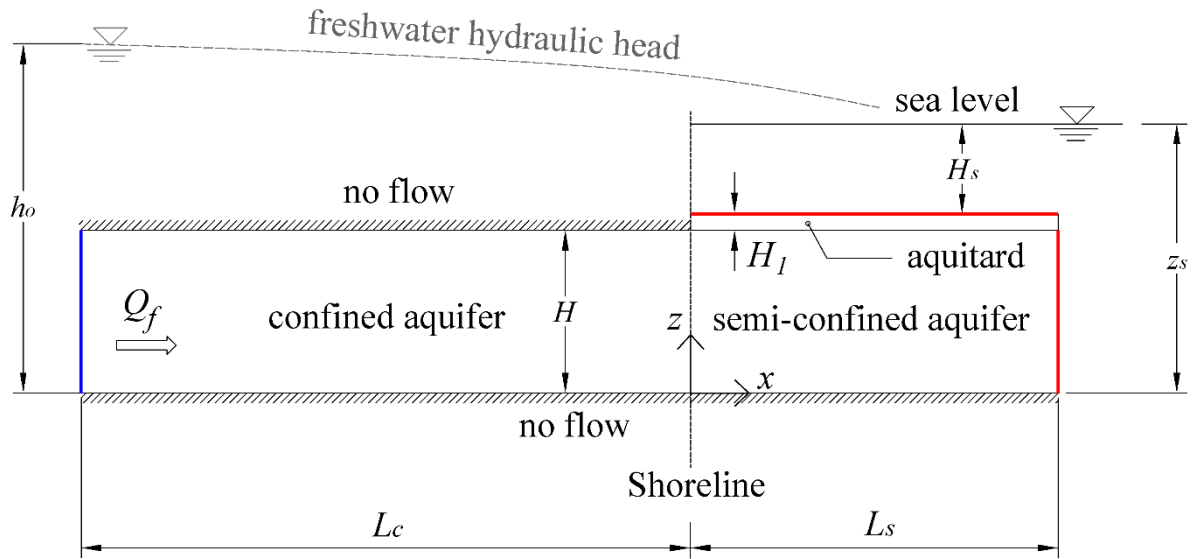


**Figure 3.2** Conceptual model to apply the Werner and Robinson (2018) sharp-interface solution (modified from Solórzano-Rivas and Werner, 2018). Colour lines denote the model input/output boundaries: blue for the inland freshwater boundary and red for the sea boundary. The vertical seaward boundary of the aquitard is a no-flow condition. The grey dashed line indicates the freshwater potential (which is higher than sea level due to density effects).

The symbols in Figure 3.2 are as follows:  $H$  is the thickness of the aquifer [L];  $H_1$  is the thickness of the aquitard [L];  $H_s$  is the depth of the sea at the top of the aquitard [L];  $z_s$  is the depth of the sea at the bottom of the aquifer [L];  $Q_f$  is the freshwater flow (per unit length of coastline) into the offshore aquifer [ $L^2 T$ ];  $h_o$  is the onshore hydraulic head [L],  $L_c$  is the length of the onshore confined aquifer [L], and  $L_s$  is the length of the offshore semi-confined aquifer [L].

The Werner and Robinson (2018) solution has the flexibility of specifying  $Q_f$  or  $h_o$  at the onshore boundary (i.e., blue line in Figure 3.2). Here, we adopted the option of specifying  $h_o$ , which is more practical given the tendency to measure and characterise groundwater heads rather than fluxes.  $Q_f$  can be calculated by applying Darcy's law in the onshore section in conjunction with knowledge of the head at the toe (if the toe is onshore), or obtaining the head at the shoreline through application of Werner and Robinson's (2018) solution (if the toe is offshore).

Werner and Robinson (2018) introduced a dimensionless parameter ( $\beta$ ) that defines the uniform groundwater salinity within the aquitard in the region where freshwater occurs in the aquifer. It can be specified within the range of 0 to 1, whereby a value of 0 indicates that the aquitard contains seawater (i.e., the assumption of Bakker (2006) and Bakker et al. (2017)), and 1 indicates that the aquitard contains freshwater, which accords with the recommendation of Solórzano-Rivas and Werner (2018). Werner and Robinson (2018) define three key parameters to solve for the offshore interface distribution, as: (1) the dimensionless discharge in the confined section (i.e., onshore aquifer),  $\mu = Q_f l_f / (KH^2 \delta)$ , where  $l_f$  is the leakage factor [L] defined by  $l_f = \sqrt{KHH_l / K_z}$ ,  $K$  is the aquifer hydraulic conductivity [ $L T^{-1}$ ],  $K_z$  is the aquitard vertical hydraulic conductivity [ $L T^{-1}$ ],  $\delta$  is the dimensionless density difference between freshwater,  $\rho_f [M L^{-3}]$ , and seawater,  $\rho_s [M L^{-3}]$ , given by  $(\rho_s - \rho_f) / \rho_f$ ; (2)  $\beta H_l / H$ ; and (3) the dimensionless offshore aquitard length:  $\lambda_s = L_s / l_f$ . Other variables have been defined earlier in the paper. The reader is referred to Werner and Robinson (2018) for a complete description of the mathematical solution.

Bakker (2006) divided the original analytical solution into four interface cases, which Werner and Robinson (2018) follow, and which depend on the toe and tip position relative to the shoreline. Cases I and III have an onshore toe, and in Cases II and IV the toe is offshore. The tip position is landward of the vertical sea boundary in Cases I and II, and is attached to the offshore limit of the aquifer (e.g., the edge of the continental shelf) in Cases III and IV. The remainder of the text designates these cases as Analytical cases I to IV to distinguish them from the numerical model cases used in this study.

Figure 3.3 shows contours of analytically derived dimensionless toe location,  $xT'$  (i.e., toe location relative to the shoreline,  $x_{toe}$ , divided by  $l_f$ , where negative and positive values indicate onshore and offshore toe locations, respectively), as a function of  $\mu$  and  $\lambda_s$ . The range  $-2.0 \leq xT' \leq 1.5$  is shown. Red lines are the boundaries separating each Analytical case, wherein the line labelled  $xT' = 0$  identifies the conditions under which the toe is coincident with the shoreline. The  $x$ -axis is truncated at  $\lambda_s = 3.5$ , because higher values of  $\lambda_s$  do not affect the salinity distribution in the subsea aquifer for Analytical cases I and II. That is, offshore aquifers longer than  $\lambda_s = 3.5$  have the same toe location for the values of  $\mu$  used in Figure 3.3.

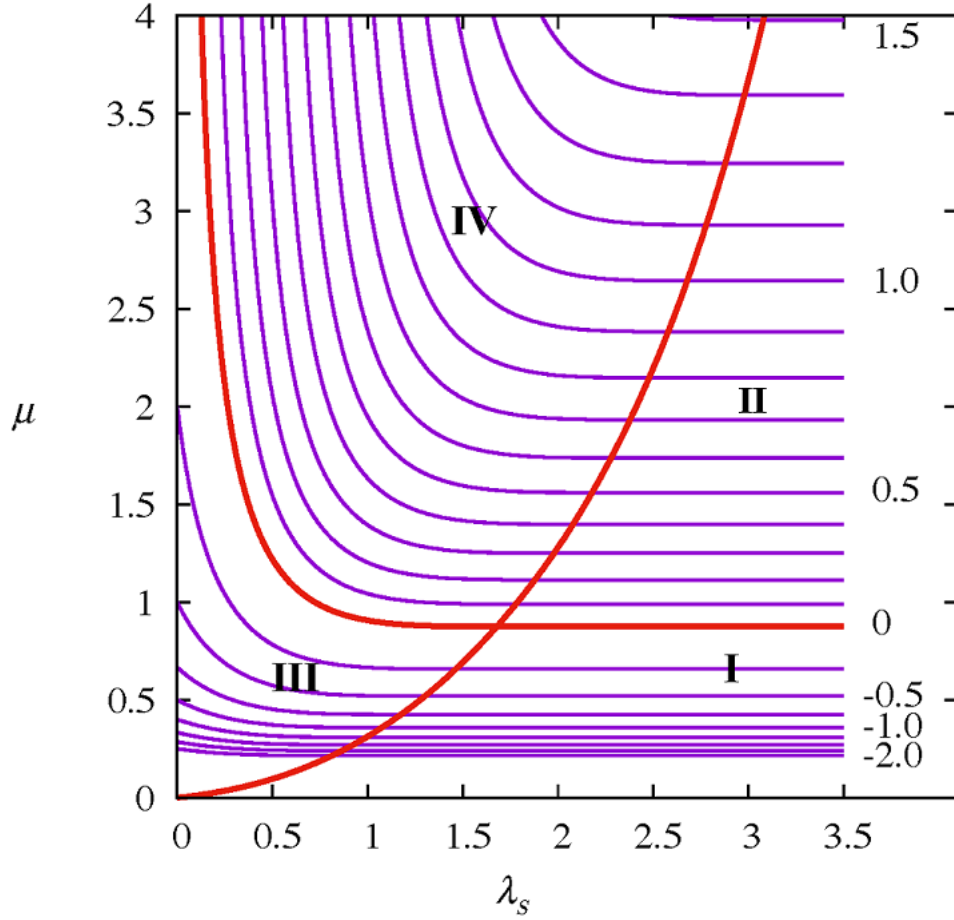


**Figure 3.3** Contours of dimensionless toe location within a range  $-2.0 \leq x_t' \leq 1.5$ , as a function of  $\mu$  and  $\lambda_s$  for a constant value of  $\beta H/H_l = 0.1$  (adapted from Werner and Robinson, 2018). Red lines demarcate the separation of Analytical cases I to IV.

The contours in Figure 3.3 provide important information about the toe position in onshore-offshore aquifer settings that is relevant to the current research objectives. For example, the contours of  $x_t'$  are nearly vertical in parts of Analytical case IV (tip connected to the offshore boundary and the toe is offshore), indicating low sensitivity of  $x_t'$  to changes in freshwater discharge ( $\mu$ ). Additionally, Analytical cases I and II are represented by horizontal  $x_t'$  contours, highlighting that those situations are independent of the dimensionless offshore length  $\lambda_s$ . According to Knight et al. (2018), published situations of significant subsea fresh groundwater predominantly involve tips that are landward of the offshore aquifer limit, at least under modern-day conditions, and therefore, Analytical cases I and II are likely the most common. For that reason, and considering also that the tip can vary in its location in Analytical cases I and II, thereby clearly differentiating our offshore aquifer analysis from onshore situations

(where the tip is relatively immobile; attached to the coastline), we focus on Analytical cases I and II in this investigation. That is, both the tip and toe potentially vary in response to parameter changes in our analysis.

### 3.4 Numerical methodology

The finite-difference numerical code SEAWAT (version 4; Langevin et al., 2008) was used to simulate dispersive cases of subsea freshwater groundwater. SEAWAT combines MODFLOW-2000 (Harbaugh et al., 2000) and MT3DMS (Zheng and Wang, 1999) to solve the equations that describe variable-density flow and solute transport in porous media. The governing equations and methodology used by SEAWAT are omitted here for brevity, and the reader is referred to the user manual (Langevin et al., 2008) for details of the code.

Numerical experiments were based on the conceptual model illustrated in Figure 3.2, and to some degree on cases developed by Solórzano-Rivas and Werner (2018), except with the incorporation of dispersion parameters. Steady-state salinity distributions were obtained for various offshore aquifer situations by running SEAWAT in transient mode until the models converged on steady-state conditions. Two different geometries are presented in this study: a small domain to allow for simulation using a fine grid (Cross section A), and a more realistic field-scale domain (Cross section B) that required coarser discretisation (see Table 3.1 for the dimensions adopted for both cross sections). Cross section A contains 111 layers and 1875 columns (total dimension of 250.05 m long by 11.1 m deep). Uniform vertical discretisation ( $\Delta z$ ) of 0.1 m was used throughout the model domain, while the horizontal discretisation ( $\Delta x$ ) varies from 0.1 m near the seaward boundary up to 10 m at the landward boundary. Cross section B (2508 m long by 55.5 m deep) comprises 111 layers and 1137 columns with  $\Delta x = 2$  m at the seaward boundary gradually increasing to 10 m at the landward boundary, and a constant  $\Delta z$  of 0.5 m. The grid sizes of both cross sections were designed such that interfaces occurred in the regions of finest discretisation (i.e., 0.1 m by 0.1 m in Cross section A, and 2 m by 0.5 m in Cross section B). We tested the effect of grid discretisation in Cross section A. For example, a finer grid was tested in Cross section A of 0.05 m by 0.05 m. Changes in salinity distributions attributable to the grid resolution were up to 2% (i.e., freshwater zone was 2% larger using a finer grid, estimated by averaging the differences in tip and toe locations),

indicating that model results are within reasonable bounds of grid dependency. In any case, the grid resolutions used in this study are at the limit of refinement in the context of model runtimes, which were up to 178.3 hours (using an Intel® Xeon® CPU, with specifications E5-1650 v4, 3.60 GHz and 32 GB RAM).

Following the model layout of Solórzano-Rivas and Werner (2018), the topmost grid layer in the offshore portion simulates the effect of the ocean using a high value for  $K$  (i.e., 10,000 m/d), and the subsequent ten layers simulate the desired aquitard thickness. The onshore boundary (blue line in Figure 3.2) is a specified head with concentration conditions equal to freshwater (i.e., zero concentration). Along the two sea boundaries (red lines in Figure 3.2), seawater hydrostatic heads were assigned. The influence of the ocean on salinities at the aquifer-ocean interface were simulated as follows:

The vertical sea boundary represents the offshore limit of the aquifer, and therefore, the concentration condition depends on the flow direction, such that discharge to the sea occurs at the ambient groundwater concentration, whereas seawater concentration was assigned to any inflowing water.

The horizontal sea boundary represents seawater immediately above the seafloor, and therefore boundary cells were assigned constant seawater concentration, presuming that freshwater discharge does not cause freshening of the sea.

Smith (2004) recommends precaution in using type (b) boundary conditions, because salt may accumulate at the boundary in an unrealistic manner. A similar issue was recognised in the original Henry problem, as reported by Segol et al. (1975), and others. Following Smith's (2004) recommendation, we tested both approaches to the assignment of boundary conditions (i.e., (a) and (b), described above) to the horizontal seafloor. Results are reported for boundary condition (b) along the seafloor, and only a selection of results obtained using boundary condition (a) are given (for brevity). As neither boundary condition accurately represents the physical mixing of freshwater and seawater within, and immediately above, the seafloor, an argument can be made for one choice over the other. The effect of seafloor boundary condition choice is reported in Section 3.4.2.

Five offshore aquifer scenarios (termed Scenarios 1 to 5) were used to explore dispersion effects on the distribution of subsea fresh groundwater. Cross section A was used for Scenarios 1 to 3, and Cross section B for Scenarios 4 and 5. Each scenario adopted a range of dispersion parameters, creating 40 simulations in total. Table 3.1 defines the parameter sets for each scenario.

**Table 3.1** Model parameters for five offshore aquifer scenarios (see Figure 3.2 for a pictorial representation of geometric parameters).

Parameter	Description and units	Cross section A			Cross section B	
		Scenario 1	Scenario 2	Scenario 3	Scenario 4	Scenario 5
$H$	Aquifer thickness [m]	10	10	10	50	50
$H_l$	Aquitard thickness [m]	1	1	1	5	5
$H_s$	Depth of the sea above the aquitard [m]	20	20	20	20	25
$L_c$	Onshore aquifer length [m]	100	100	100	500	500
$L_s$	Offshore aquifer length [m]	145	145	145	2000	2000
$h_o$	Onshore head [m]	32	33	32	78	82.5
$z_s$	Sea level height above aquifer base [m]	31	31	31	75	80
$K$	Aquifer hydraulic conductivity [m/d]	10	25	10	10	40
$K_z$	Aquitard hydraulic conductivity [m/d]	0.5	0.5	0.05	0.01	0.025
$K:K_z$	Aquifer $K$ -aquitard $K_z$ contrast [-]	1:20	1:50	1:200	1:1000	1:1600
$n_e$	Effective porosity[-]	0.3	0.3	0.3	0.3	0.3
$\alpha_L$	Aquifer longitudinal dispersivity [m]	0.1, 0.25, 0.5, 0.75, 1, 2.5, 5, 10	0.1, 0.25, 0.5, 0.75, 1, 2.5, 5, 10	0.1, 0.25, 0.5, 0.75, 1, 2.5, 5, 10	1, 2.5, 5, 10, 20, 30, 40, 50	1, 2.5, 5, 10, 20, 30, 40, 50
$\alpha_L/\alpha_T$	Aquifer dispersivity anisotropy [-]	10	10	10	10	10
$\alpha_{Ll}$	Aquitard longitudinal dispersivity [m]	0.05	0.05	0.05	0.25	0.25
$\alpha_{Ll}/\alpha_{Tl}$	Aquitard dispersivity anisotropy [-]	10	10	10	10	10
$D_m$	Molecular diffusion [m <sup>2</sup> /d]	8.64E-05	8.64E-05	8.64E-05	8.64E-05	8.64E-05

Parameters were selected to obtain interfaces that remained sufficiently distant from the seaward and landward model limits, partly to avoid boundary effects. The aquifer  $K$ -aquitard  $K_z$  contrast, known to be a key controlling factor of subsea freshwater extent, increased from 1/20 in Scenario 1 to 1/1600 in Scenario 5. Adopted values of  $K$  (10 to 40 m/d) and  $K_z$  (0.025 to 0.5 m/d) are generally within the range of typical field values for subsea aquifers (e.g., 0.86 to 90 m/d; Knight et al., 2018) and aquitards ( $10^{-6}$  to 0.1 m/d; Knight et al., 2018), respectively, with the exception being the relatively high  $K_z$  value of 0.5 m/d adopted for Scenarios 1 and 2. We chose this relatively high value of  $K_z$  so that small aquifer  $K$ -aquitard  $K_z$  contrasts (i.e., 20:1 and 50:1; Scenarios 1 and 2, respectively) and near-shore tip locations were included in the range of conditions. Otherwise, parameters were derived from a review of other coastal aquifer modelling studies (e.g., Kooi and Groen, 2001; Smith, 2004, Werner, 2017a; Werner, 2017b, Solórzano-Rivas and Werner, 2018). The dimensionless variables  $\mu$  and  $l_f$  used in this study allow for comparison with field conditions as reported by Knight et al. (2018). Values of  $\mu$  used in Scenarios 1 to 5 are 0.19, 1.06, 0.52, 0.89 and 0.69, respectively, and the corresponding  $l_f$  values are 14 m, 22 m, 45 m, 500 m and 630 m. A wide range of field conditions are observed in the data of Knight et al. (2018), for which  $\mu$  values vary between 0.01 and 16 and  $l_f$  values range from 140 m to 770 m. The values of  $\mu$  used in all five scenarios are therefore relatively low albeit they fall within the range for realistic situations.  $l_f$  values from Scenarios 1 to 3 are below the lower limit of Knight et al.'s (2018) cases, whereas  $l_f$  values for Scenarios 4 and 5 are within the range of real-world cases.

It is well established that dispersion (in models) represents the largely unknown heterogeneity in the subsurface, and that its magnitude is proportional to the scale of the analysed domain (e.g., Gelhar et al., 1992; Bear and Cheng, 2010; Zech et al., 2015). Here, to test different values of dispersion parameters, the longitudinal dispersivity ( $\alpha_L$ ) and transverse dispersivity ( $\alpha_T$ ) were varied systematically. Within the aquifer, the following criteria were considered:

- The minimum value of  $\alpha_L$  was constrained by the recommended grid Peclet number ( $Pe_x$ : given by  $\Delta x/\alpha_L \leq 2$ ; Zheng and Bennett, 2002) to reduce artificial oscillations in SEAWAT's solution.
- The maximum value of  $\alpha_L$  was set to approximately 1/10 of the offshore aquifer length (e.g., Gelhar, 1992; Bear and Cheng, 2010).

- Given that flow near the mixing zone has a significant vertical component (e.g., Abarca et al., 2007), the maximum value of  $\alpha_L$  was further limited to the thickness of the aquifer (i.e., maximum  $\alpha_L \leq H$ ).
- A constant dispersivity anisotropy ratio ( $\alpha_L/\alpha_T$ ) of 10 was adopted. This is consistent with previous studies (e.g., Kooi and Groen, 2001; Smith, 2004; Badaruddin et al., 2017; Werner, 2017a).
- In order to evaluate if seawater circulation rates in offshore aquifers show the same non-monotonic relationship with dispersion as found by Smith (2004) for onshore aquifers, our dimensionless dispersion values (e.g.,  $\alpha_L/H$ ,  $\alpha_T/H$ ) were designed to cover the entire range used by Smith (2004), within the limits described above.

For the aquitard, each scenario used a single value for the longitudinal dispersivity ( $\alpha_{LI}$ ): 0.05 m for all models adopting Cross section A (i.e., Scenarios 1 to 3), and 0.25 m for models adopting Cross section B (i.e., Scenarios 4 and 5). Given that flow within the aquitard is predominantly vertical (e.g., Solórzano-Rivas and Werner, 2018),  $\alpha_{LI}$  was set according to the  $Pe_z$  ( $\Delta z/\alpha_{LI} \leq 2$ ) restriction of Zheng and Bennett (2002). Frind (1982) suggested that a normal contrast of dispersivity values between aquifer and aquitard is around three orders of magnitude (i.e.,  $\alpha_L/\alpha_{LI} = 1000$ ). In this study, given that  $\alpha_L$  varies and  $\alpha_{LI}$  is constant, the dispersivity contrast between aquifer and aquitard varies between one and three orders of magnitude for Cross section A, and between one and two orders of magnitude for Cross section B. The lowest aquifer-aquitard dispersivity contrast used in this study was also adopted by Huyakorn et al. (1987).

### 3.5 Output variables

The effects of dispersion on subsea aquifers were quantified in terms of the output variables described below and illustrated in Figure 3.4. Similar output variables have been used by others (e.g., Smith, 2004; Pool and Carrera, 2005; Abarca et al., 2007; Badaruddin et al., 2017).

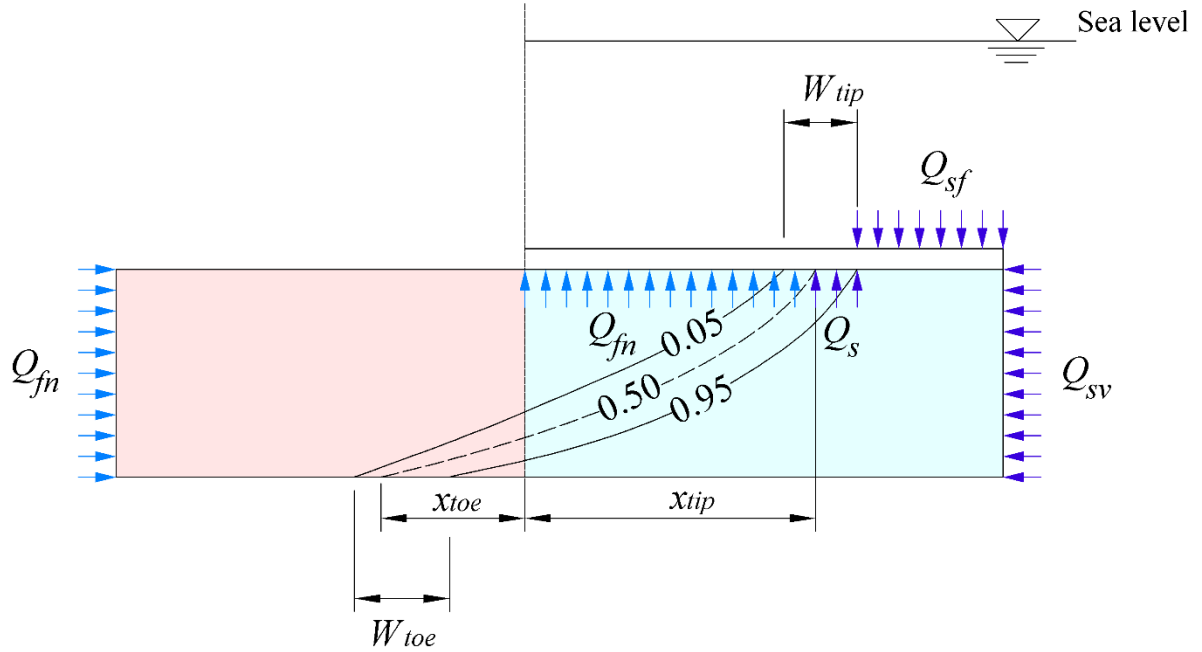


**Figure 3.4** Schematic of the variables used to describe the results of dispersive subsea aquifer simulations. Light blue and dark blue arrows represent the inflow/outflow of groundwater with salinity (relative to seawater) of  $<50\%$  and  $>50\%$ , respectively. Arrows lengths do not infer the rates of inflow and outflow. Pink and cyan shaded areas represent the onshore and offshore aquifers, respectively. Contour labels are salinities relative to seawater.

The tip penetration ( $x_{tip}$ ) and toe penetration ( $x_{toe}$ ) are defined by the steady-state location of the 0.5 isochlor at the top and bottom of the aquifer, respectively, measured from the shoreline (i.e., onshore and offshore values of  $x_{toe}$  are negative and positive, respectively; Figure 3.4). The dimensionless widths of the mixing zone at the aquifer top ( $W'_{tip}$ ) and bottom ( $W'_{toe}$ ) are defined as  $W_{tip}/H$  and  $W_{toe}/H$ , respectively, where  $W_{tip}$  and  $W_{toe}$  are the horizontal distances between the 0.05 and 0.95 isochlors at the top and bottom of the aquifer, respectively. A similar definition was used by Badaruddin et al. (2017). The onshore boundary was defined by  $h_o$ , while  $Q_f$  (see Figure 3.2) to the subsea aquifer was calculated rather than specified. We use  $Q_f$  and  $Q_{fn}$  for the analytically derived and numerically derived freshwater discharge rates, respectively.  $Q_{fn}$  is compared to  $Q_f$  using:

$$\Delta Q_f(\%) = \frac{(Q_{fn} - Q_f)}{Q_f} \times 100 \quad (3.1)$$

We expect that dispersion will influence the rate of seawater circulation, given the findings of Smith (2004) for onshore aquifers. Seawater circulation is induced by the entrainment of

seawater in the freshwater discharge to the sea, and requirements for balanced salt mass in the subsea aquifer under steady-state conditions (e.g., Cooper et al., 1964). Smith (2004) studied the phenomenon of seawater circulation within a two-dimensional cross-sectional model of onshore freshwater discharge towards the sea, and included a short offshore section of aquifer. His conceptual model differs from ours in that there is not an intervening aquitard separating the submarine aquifer from the sea in Smith's (2004) models. The absence of an offshore aquitard leads to very little offshore fresh groundwater, and rather, the interface tip remains near to the shoreline. For the purposes of analysing seawater recirculation patterns, Smith (2004) defined a dimensionless seawater flux ( $SC$ ), as:

$$SC(\%) = \frac{Q_s}{Q_{fn}} \times 100 \quad (3.2)$$

where  $Q_s$  is the rate of seawater flow [ $L T^{-2}$ ] from/to the sea.  $Q_s$  is made of two components, namely seawater inflow through the horizontal seafloor ( $Q_{sf}$ ) and through the vertical face of the continental shelf ( $Q_{sv}$ ).

### 3.6 Mixed convection analysis

Unstable buoyancy conditions in fluid motion arise when a denser fluid overlies a lighter one. Under certain circumstances, this can give rise to the onset of downward-moving plumes, typically in the shape of 'fingers'. When unstable problems are governed by both forced convection (i.e., due to hydraulic forces) and free convection (i.e., buoyancy or fluid density-driven forces), it is said to be a mixed-convective flow regime (e.g., Simmons et al., 2010). Solórzano-Rivas and Werner (2018) undertook a mixed-convection analysis in subsea aquitards subject to upward freshwater flow towards the seafloor. They used the boundary layer theory of Wooding et al. (1997), whereby a critical boundary Rayleigh number ( $Ra_\delta$ ) exists at which the buoyancy and dispersive forces are in equilibrium, forming a stable solute layer beneath the boundary. Solórzano-Rivas and Werner (2018) adopted for convenience a dispersion-independent form of Wooding et al.'s (1997)  $Ra_\delta$  (see below), which allowed them to avoid the need to quantify artificial, numerical dispersion within their 'zero-dispersion' SEAWAT simulations.

$$Ra_{\delta} = \frac{(\rho_s - \rho_f)K_z}{\rho_f q_z} \quad (3.3)$$

Here,  $q_z$  is the Darcy flux of vertical freshwater flow through the aquitard at the position where the 0.5 isochlor intercepts the base of the aquitard [ $L T^{-1}$ ]. A  $Ra_{\delta}$  of around 2 was obtained by Solórzano-Rivas and Werner (2018) for the conditions leading to half-seawater concentrations (i.e., the 0.5 isochlor) at the top of the offshore aquifer. This value of  $Ra_{\delta}$  was considered a predictor of the transition between freshwater and seawater within the aquitard, assuming predominantly vertical aquitard flow and low-dispersion conditions.

We extend the Rayleigh analysis of Solórzano-Rivas and Werner (2018), which focused on sharp-interface solutions, by studying mixed convective processes under varying degrees of dispersiveness. That is, values of  $q_z$  (where the 0.5-isochlor meets the aquifer top) were obtained from modelling results and used in equation (3.3) to explore whether the critical value of  $Ra_{\delta}$ , obtained for low-dispersion conditions by Solórzano-Rivas and Werner (2018), applies under more realistic levels of dispersiveness.

The  $Ra_{\delta}$  analysis described above is relevant to the development of boundary salt layers within aquitard sediments, whereas Smith and Turner (2001) proposed a modified Rayleigh number ( $Ra^*$ ) to assess the forces that cause water from a saline estuary to sink into an underlying freshwater aquifer, without an intervening aquitard. In their case, the groundwater beneath the estuary flows laterally. That aspect of their conceptual model is comparable to ours, except Smith and Turner (2001) did not consider the intervening aquitard (Figures 3.1 and 3.2). From numerical experimentation, Smith and Turner (2001) concluded that the critical  $Ra^*$  for the occurrence of saltwater below the estuary is approximately five. They proposed the following Rayleigh number formulation:

$$Ra^* = \frac{KH}{n_e q_z \alpha_L} \left( \frac{\rho_s - \rho_f}{\rho_f} \right) \left( \frac{U_+}{U_-} \right) \quad (3.4)$$

Here,  $n_e$  is the effective porosity [-] and  $U_+/U_-$  is the regional discharge ratio between the flow crossing the left-hand and right-hand boundaries (i.e., allowing for asymmetric flow to the estuary), respectively. Other parameters have been previously defined. In order to apply the Smith and Turner (2001) formulation to the conceptual model shown in Figure 3.2,  $q_z$  is taken

at the location of the 0.5-isochlor at the top of the aquifer (see equation 3.4) as a substitute for their uniform discharge across the riverbed (i.e.,  $U_d$  in the notation of Smith and Turner (2001)). We also assign  $U_+/U_-$  a value of one, so that the problem is treated as symmetric.

## 3.7 Results

### 3.7.1 Sensitivity to dispersion

#### 3.7.1.1 *Tip and toe penetration*

Figure 3.5 presents the steady-state locations of the 0.5 isochlor from five scenarios (see Table 3.1), showing the variability that arises with changes in dispersivity. The left column of graphs depicts the tip and toe location, while the right column shows interface shapes. Numerical results are compared with the Werner and Robinson (2018) analytical solution, which are the grey-coloured symbols and lines. Hereafter, we refer to the Werner and Robinson (2018) solution as the sharp-interface or analytical solution.

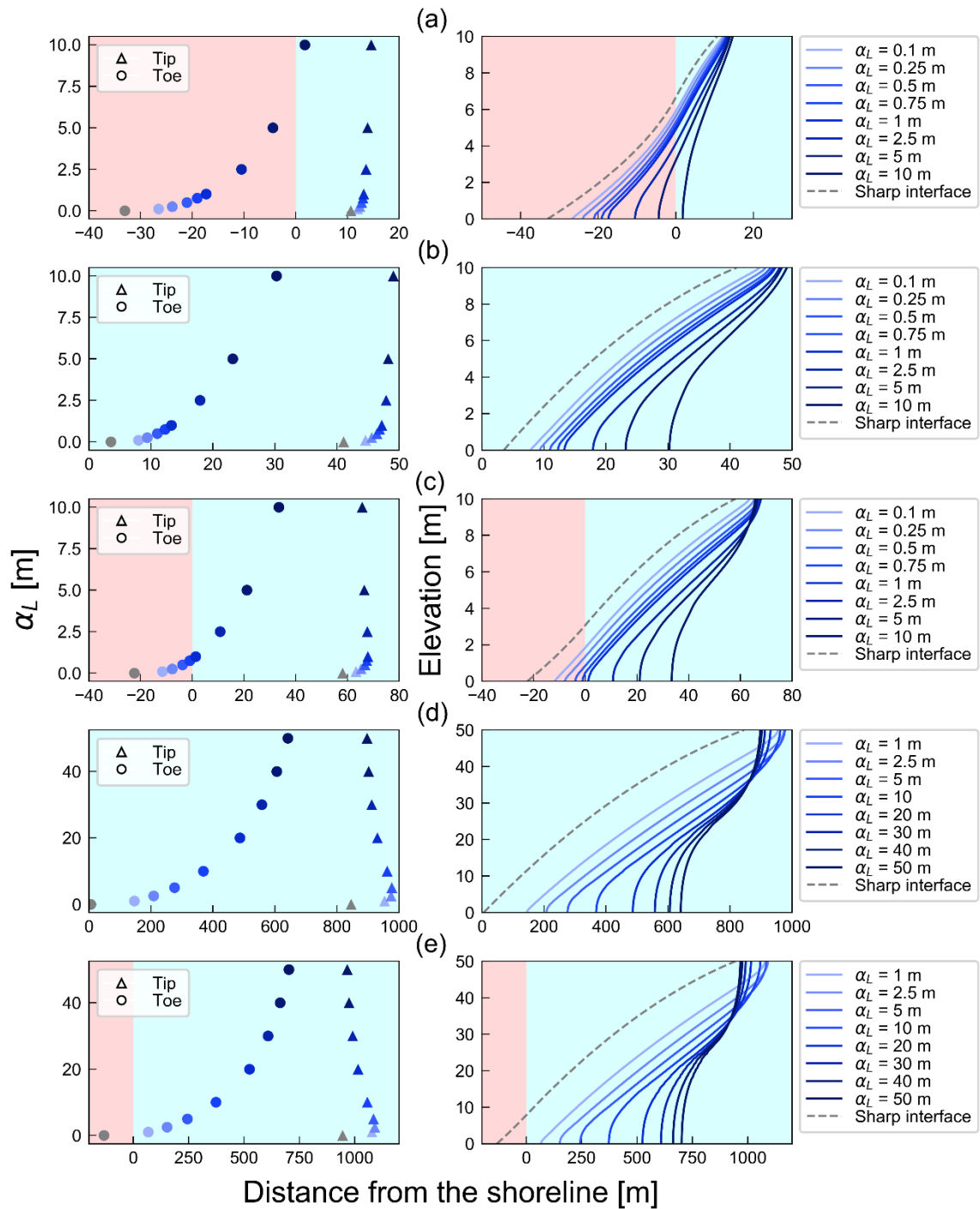


**Figure 3.5** Steady-state locations of the 0.5 isochlor (50% seawater salinity) for the five scenarios (see Table 3.1), where panels (a) to (e) are Scenarios 1 to 5, respectively. Tip and toe locations from each simulation are given in the left column of graphs, while interface shapes are shown in the right column. The parameterisation of  $\alpha_L$  is depicted by the colour of symbols and lines. Grey lines and symbols represent the sharp-interface solution, and the pink and cyan shaded areas identify the onshore and offshore domains, respectively.

The results show that the position of the 0.5 isochlor is significantly affected by dispersion. The left-column graphs of Figure 3.5 illustrate that  $x_{toe}$  has a monotonic relationship with dispersion, indicated by  $x_{toe}$  increases (i.e., seaward advance) with larger dispersivity. This is consistent with studies of the effects of dispersion on  $x_{toe}$  in onshore coastal aquifers (e.g., Volker and Rushton, 1982). The same general trend is observed for all  $K:K_z$  contrasts (i.e., Scenarios 1 to 5). The tip also moves seaward with increasing dispersivity, monotonically, in Scenarios 1 and 2. However, changes in  $x_{tip}$  with varying dispersivity show a non-monotonic relationship in Scenarios 3 to 5. That is, increasing dispersivity leads to more seaward  $x_{tip}$  values until a maximum is reached, and then  $x_{tip}$  retreats towards the shoreline with increasing dispersivity. Therefore, the trend in  $x_{tip}$  arising from changes to dispersivity depends on the  $K:K_z$  contrast. Figure 3.5 also shows that  $x_{toe}$  is more responsive to changes in dispersivity compared to corresponding changes in  $x_{tip}$ .

The largest  $K:K_z$  contrast (e.g., 1600:1 in Scenario 5; Figure 3.5e) and highest dispersivity values (e.g.,  $\alpha_L = 50$  m) lead to  $x_{tip}$  values that approach the sharp-interface  $x_{tip}$  position. This is in contrast to the notion devised from studies of onshore coastal aquifers that dispersion creates more extensive freshwater bodies and smaller seawater wedges relative to sharp-interface solutions. Instead, the contraction of the offshore freshwater extent with increased dispersion is similar behaviour to that of riparian freshwater lenses (Werner and Laattoe, 2016; Werner, 2017a). Thus, freshwater-seawater interfaces of offshore aquifers show dispersive behaviour that is a mixture of that observed in onshore coastal aquifers and within terrestrial freshwater lenses.

The responses in the tip and toe to changes in dispersion were quantified through sensitivity analysis, as presented in Table 3.2. We report the ‘traditional sensitivity’ (e.g., Robinson and Werner, 2017), given by  $S_{toe} = \frac{\Delta x_{toe} \alpha_L}{x_{toe} \Delta \alpha_L}$  and  $S_{tip} = \frac{\Delta x_{tip} \alpha_L}{x_{tip} \Delta \alpha_L}$  for the toe and tip, respectively.

**Table 3.2** Dimensionless sensitivities ( $S_{tip}$  and  $S_{toe}$ ) describing changes in the tip and toe with changes to  $\alpha_L$  (indicated by the shaded numbers) in the five scenarios described in Table 2.1. Negative values of  $S_{tip}$  indicate that increasing  $\alpha_L$  causes a decrease in  $x_{tip}$ , otherwise  $x_{tip}$  increases with  $\alpha_L$ .  $x_{toe}$  increased with  $\alpha_L$  in all cases, and therefore negative  $S_{toe}$  values indicate that  $x_{toe}$  is onshore.

$S_{tip}$ to changes in $\alpha_L$							
$\alpha_L$ [m] =	0.1-0.25	0.25-0.5	0.5-0.75	0.75-1	1-2.5	2.5-5	5-10
Scenario 1	0.024	0.028	0.040	0.033	0.021	0.024	0.049
Scenario 2	0.015	0.018	0.020	0.019	0.010	0.007	0.017
Scenario 3	0.022	0.023	0.020	0.014	-0.001	-0.017	-0.012
$\alpha_L$ [m] =	1-2.5	2.5-5	5-10	10-20	20-30	30-40	40-50
Scenario 4	0.014	0.002	-0.015	-0.033	-0.039	-0.033	-0.023
Scenario 5	0.008	-0.006	-0.026	-0.040	-0.047	-0.047	-0.034
$S_{toe}$ to changes in $\alpha_L$							
$\alpha_L$ [m] =	0.1-0.25	0.25-0.5	0.5-0.75	0.75-1	1-2.5	2.5-5	5-10
Scenario 1	-0.07	-0.12	-0.19	-0.27	-0.26	-0.58	-1.40
Scenario 2	0.12	0.17	0.23	0.25	0.23	0.29	0.30
Scenario 3	-0.22	-0.51	-1.47	-6.68	-5.05	0.96	0.59
$\alpha_L$ [m] =	1-2.5	2.5-5	5-10	10-20	20-30	30-40	40-50
Scenario 4	0.28	0.32	0.33	0.32	0.29	0.26	0.24
Scenario 5	0.83	0.60	0.53	0.41	0.32	0.27	0.23

Table 3.2 demonstrates that for all scenarios, the toe is more sensitive to dispersion than the tip, by around one-to-two orders of magnitude, consistent with the graphical representation of results in Figure 3.5. Specifically, the ratio of toe shift to tip shift (i.e.,  $\Delta x_{toe}/\Delta x_{tip}$ ) caused by changes in dispersivity, on average, is about 9:1 in our simulations. There is some evidence of patterns in  $S_{toe}$  behaviour with rising dispersivity and with increasing  $K:K_z$  contrast (recalling that  $K:K_z$  increases from Scenarios 1 to 5; Table 3.1), albeit the change in  $\alpha_L$  from 1 to 2.5 m in Scenarios 1 and 2 are anomalous to otherwise generalizable trends. That is,  $|S_{toe}|$  rises with increasing dispersivity in Scenarios 1 and 2, rises-then-falls in Scenarios 3 and 4, and falls in Scenario 5. Note that Scenarios 1 to 3 adopted a set of  $\alpha_L$  values that differed to those used in Scenarios 4 and 5 (see Table 3.1), and yet, the rising-then-falling trend in  $|S_{toe}|$  was nevertheless observed in both Scenarios 3 and 4. Despite the relationship between  $S_{tip}$  and dispersivity being rather complex, whenever negative value of  $S_{tip}$  were obtained (i.e., the tip shifted landward), the value of  $S_{toe}$  shows a downward trend (with increasing  $\alpha_L$ ), albeit this behaviour is based on only three simulations and is difficult to conceptualise in terms of physical causes.

### 3.7.1.2 *Width of the mixing zone*

The effect of dispersion on  $W'_{tip}$  and  $W'_{toe}$  for each scenario is illustrated in Figure 3.6. It is evident that  $W'_{tip}$  and  $W'_{toe}$  respond differently to changes in dispersivity. While an increase in dispersivity widens  $W'_{toe}$ ,  $W'_{tip}$  shows a surprising non-monotonic relationship with dispersivity. Even though both  $W'_{tip}$  and  $W'_{toe}$  show asymptotic behaviour with increasing  $\alpha_L$ ,  $W'_{tip}$  reaches a maximum in Scenarios 4 and 5, and subsequently a declining trend with increasing dispersivity is apparent. Also, the maximum  $W'_{tip}$  value is reached at lower dispersivity values as the  $K:K_z$  contrast increases (i.e., Scenario 5 reaches the maximum  $W'_{tip}$  at a lower dispersivity value than that of Scenario 4). For all but the lowest  $K:K_z$  contrast (Scenario 1),  $W'_{tip}$  and  $W'_{toe}$  differ the most under lower dispersivity, and appear to converge on similar values at higher dispersivity values.

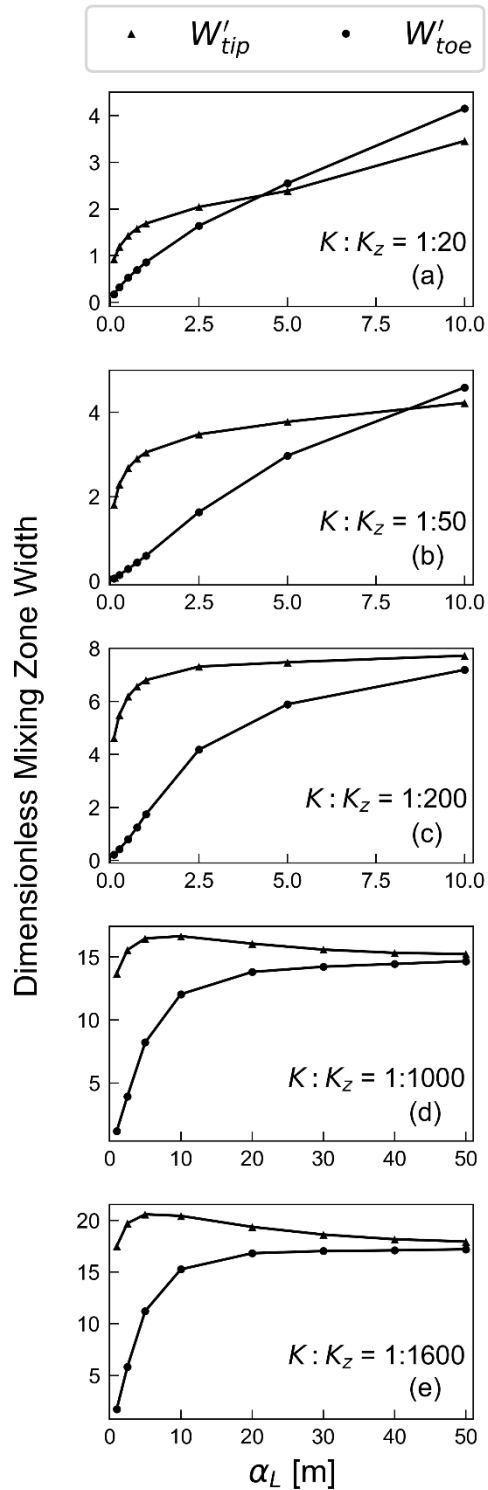


**Figure 3.6** Dimensionless mixing zone widths at the tip ( $W'_{tip}$ ) and toe ( $W'_{toe}$ ) for different values of dispersivity. The effects of changing the  $K:K_z$  contrast is demonstrated by differences in subfigures (a) to (e), which represent Scenarios 1 to 5 (the  $K:K_z$  ratio is shown in each subfigure), respectively.

Changes to the contrast in  $K$  and  $K_z$  play a significant role in the patterns of interface widening. For example, stronger  $K:K_z$  contrasts (i.e., increasing from Scenarios 1 to 5) lead to wider interfaces despite otherwise the same dispersivity values being adopted, as evident in higher values of both  $W'_{tip}$  and  $W'_{toe}$  (compare Figures 3.6a to 3.6c, and 3.6d to 3.6e). Specifically,  $W'_{tip}$  and  $W'_{toe}$  were 255% and 98% larger (respectively) in Scenario 3 relative to Scenario 1, and were 22% and 24% larger (respectively) in Scenario 5 relative to Scenario 4 (averaged across the simulations of each scenario). Also,  $W'_{toe}$  is much lower than  $W'_{tip}$  at low values of  $\alpha_L$  in the higher  $K:K_z$  scenarios (i.e., Scenarios 3 to 5), whereas in Scenario 1,  $W'_{tip}$  and  $W'_{toe}$  are much closer for all values of  $\alpha_L$ . Additionally,  $W'_{tip}$  exceeds  $W'_{toe}$  in all simulations except for higher values of  $\alpha_L$  in Scenarios 1 and 2. These results highlight the strong dispersive effect that is imposed by the aquifer-aquitard boundary, which, depending on the contrast between  $K$  and  $K_z$ , may cause more interface widening at the tip than the effect of varying the dispersivity values within reasonable limits.

### 3.7.1.3 *Change in freshwater discharge to the sea*

The effect of dispersion on  $\Delta Q_f$  (positive values indicate that numerical fluxes exceed analytical fluxes) is shown in Figure 3.7. Monotonic relationships between  $\Delta Q_f$  and dispersion were obtained, whereby an increase in  $\Delta Q_f$  represents an increase in  $Q_f$ , because  $Q_f$  is dispersion-independent. Figure 3.7 shows asymptotic behaviour for all cases except Scenario 1, in that for higher dispersivity values (i.e.,  $\alpha_L/H$  is greater than about 0.4),  $\Delta Q_f$  varies little with changes to dispersivity. The slope of the Scenario 1 curve gradually reduce with  $\alpha_L/H$ , and therefore, we expect that with higher values of  $\alpha_L/H$ , asymptotic behaviour is likely, although testing this would require the use of unrealistic  $\alpha_L$  values. The ratio  $K:K_z$  does not correlate to  $\Delta Q_f$ , demonstrated by the mixed order of scenarios with respect to  $\Delta Q_f$  (Figure 3.7).

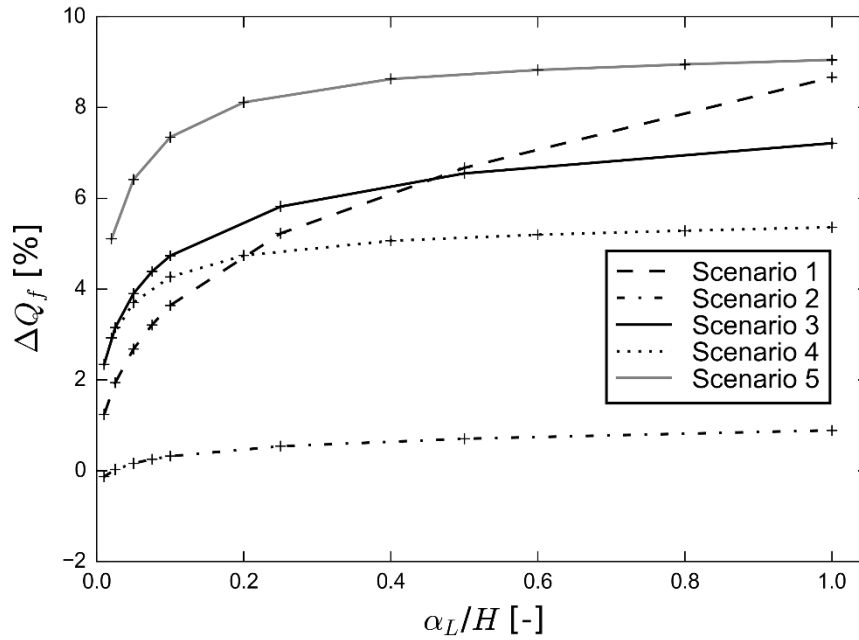


**Figure 3.7** Freshwater discharge deviation ( $\Delta Q_f$ ) attributable to dispersion effects, i.e., as a function of dimensionless dispersivity. Positive values of  $\Delta Q_f$  indicate that the numerically derived freshwater flux is larger than the corresponding analytically derived freshwater flux.

The very small negative  $\Delta Q_f$  value (i.e., -0.13%) at the start of the Scenario 2 curve, indicating that  $Q_f$  exceeds  $Q_{fn}$ , is a numerical artefact. We simulated Scenario 2 with no dispersion (i.e.,  $\alpha_L = 0$ ) in SEAWAT to explore the role of numerical aspects (e.g., artificial numerical dispersion, truncation error, etc.) in this initial negative value of  $\Delta Q_f$ . The resulting non-dispersive  $Q_{fn}$  value was 2.96 m<sup>3</sup>/d, compared to  $Q_f = 2.97$  m<sup>3</sup>/d from the analytical solution. This slight difference results in the small negative value for  $\Delta Q_f$  in Scenario 2 ( $\alpha_L/H = 0.01$ ). Using the non-dispersive  $Q_{fn}$  value as a substitute for  $Q_f$  (i.e., to allow the calculation of  $\Delta Q_f$  whereby small numerical nuances are consistent between simulations) in equation 3.1,  $\Delta Q_f$  for  $\alpha_L/H = 0.01$  would be 0.42% instead of -0.13%. Thus, we conclude that  $Q_{fn}$  increases consistently with dispersion across all scenarios.

#### 3.7.1.4 Seawater circulation

Figure 3.8 depicts the relationship between  $SC$  and dispersion (defined in terms of  $\alpha_T/H$  for ease of comparison to the onshore-aquifer results of Smith (2004)) for each scenario. The labelled values of  $\mu$  in Figure 3.8 are from the analytical solution. The results show that as dispersivity

increases,  $SC$  increases monotonically. This does not accord with the non-monotonic relationship observed for onshore aquifers by Smith (2004), who adopted similar ranges of  $\alpha_L/H$  and  $\alpha_T/H$  to those of the current study. Figure 3.8 also indicates that  $SC$  depends on  $\mu$ , showing an inverse correlation between the two variables. It is noteworthy that in Scenario 1, seawater moved within several circulation cells, while other scenarios involved only a single seawater circulation cell. The result shown in Figure 3.8 is based on the rate of seawater flux passing through the model domain, and therefore, the fluxes of any closed seawater recirculation bodies are not included in the values given for seawater circulation.

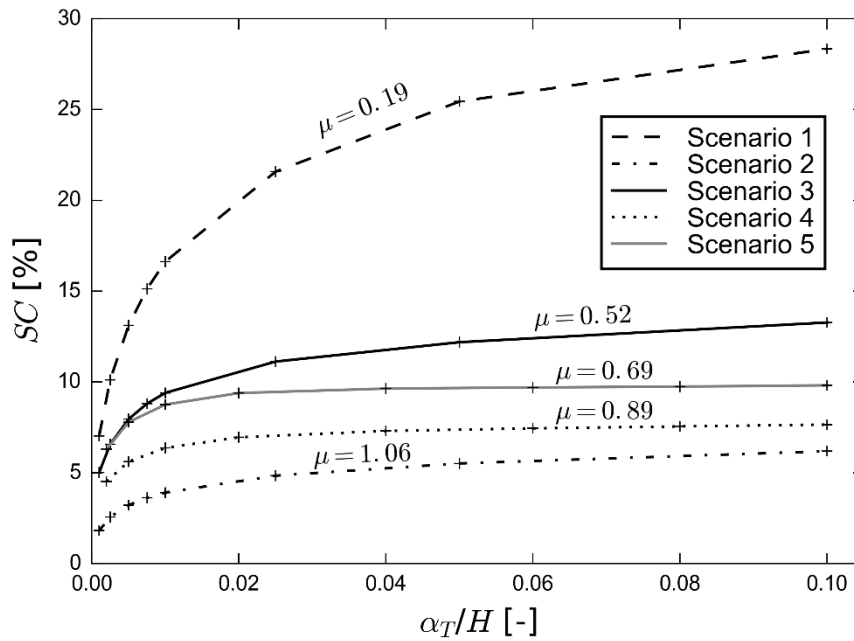


**Figure 3.8** Dimensionless seawater circulation rates ( $SC$ ) versus dimensionless dispersivity (given in terms of  $\alpha_T/H$ ). Curves are labelled with the analytical, sharp-interface value of  $\mu$ , showing that the vertical sequencing of the curves is correlated to  $\mu$  (i.e.,  $\mu$  increases from top to bottom).

While only the analytically derived  $\mu$  is labelled in Figure 3.8 for simplicity, the same relationship between  $\mu$  and  $SC$  occurs when  $\mu$  is estimated numerically (i.e.,  $Q_{fn}$  is used instead of  $Q_f$  to calculate  $\mu$ ). Values of numerically derived  $\mu$  as dispersion increases are given in the Discussion section.

### 3.7.1.5 Revisiting mixed-convection theory for dispersive conditions

Both forms of the Rayleigh number,  $Ra_\delta$  and  $Ra^*$  (Wooding et al., 1997; Smith and Turner, 2001) were determined from the numerical modelling results in accordance with the position at which the 0.5 isochlor crosses the top of the aquifer. The relationships between  $Ra_\delta$  and  $\alpha_L/H$ , and  $Ra^*$  and  $\alpha_L/H$  are shown in Figures 3.9 and 3.10, respectively. Both Rayleigh variants show inverse relationships with dispersion. However, the effect of the  $K:K_z$  contrast on relationships between  $Ra_\delta$  and  $Ra^*$ , and  $\alpha_L/H$  differ. That is, while  $Ra_\delta$  decreases as the  $K:K_z$  contrast increases, the opposite trend arises for  $Ra^*$ .

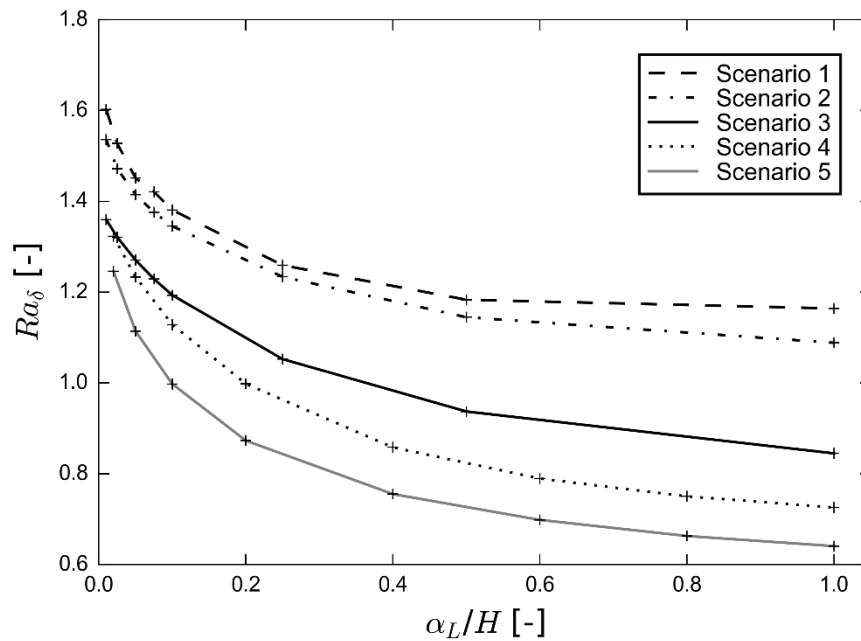


**Figure 3.9**  $Ra_\delta$  values versus dimensionless dispersivity.

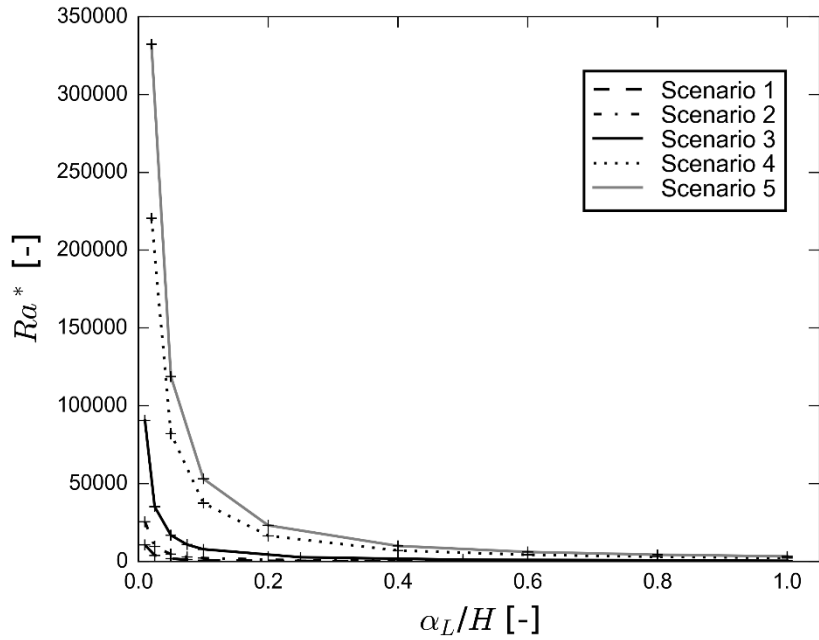


**Figure 3.10**  $Ra^*$  values versus dimensionless dispersivity.

Whereas Solórzano-Rivas and Werner (2018) obtained a single value of  $Ra_\delta$  for multiple non-dispersive situations, Figures 3.9 and 3.10 indicate that unique values of  $Ra_\delta$  and  $Ra^*$  are not forthcoming from our dispersive simulations. In Figure 3.9, the different curves tend to converge with increasing values of the Rayleigh number (and as  $\alpha_L/H$  decreases), while at high values of  $\alpha_L/H$ , there is significant spread in  $Ra_\delta$ . We also estimated  $Ra_\delta$  for Scenarios 2 and 4 when  $\alpha_L = 0$  m, obtaining values of 1.8 and 2, respectively. This is, in essence, consistent with the finding of Solórzano-Rivas and Werner (2018), who reported a value of  $Ra_\delta$  of around 2 for sharp-interface problems. The relationships depicted in Figure 3.10 indicate that a single value of  $Ra^*$ , for characterising mixed-convective processes in subsea aquifers, is not easily recognizable from our results.

### 3.7.2 Effect of the seafloor boundary condition

Table 3.3 compares output variables from models adopting one of the two different options for the solute boundary conditions of the seafloor (i.e., boundary conditions (a) and (b); see Section 3.3.2). For brevity, only the results from four simulations are presented in Table 3.3, namely Scenario 2 (with  $\alpha_L$  values of 0 m and 1 m) and Scenario 4 (with  $\alpha_L$  values of 0 m and 20 m). Simulations with  $\alpha_L = 0$  m are included to extend the analysis of Solórzano-Rivas and Werner

(2018), who adopted only boundary condition type (a) in their non-dispersive numerical modelling.

**Table 3.3** Effects of the seafloor boundary condition (where (a) represents flow direction-dependent salt mass flux, and (b) represents fixed concentration; see Section 3.3.2) on dispersive ( $\alpha_L = 1$  m and  $\alpha_L = 20$  m) and non-dispersive numerical solutions ( $\alpha_L = 0$  m) for Scenarios 2 and 4.

Model		Output variable	Boundary condition (a)	Boundary condition (b)	Discrepancy	
Scenario 2	$\alpha_L = 1$ m	$x_{tip}$ (m)	46.8	47.2	0.89%	
		$x_{toe}$ (m)	13.2	13.3	0.85%	
		$W'_{tip}$	3.0	3.0	1.7%	
		$W'_{toe}$	0.6	0.6	0.52%	
		$SC$ (%)	3.9	3.9	-0.68%	
		$\Delta Q_f$ (%)	0.4	0.3	-14%	
	$\alpha_L = 0$ m	$x_{tip}$ (m)	42.1	42.5	0.86%	
		$x_{toe}$ (m)	6.1	6.3	2.1%	
	Scenario 4	$\alpha_L = 20$ m	$x_{tip}$ (m)	925.8	930.2	0.47%
			$x_{toe}$ (m)	483.6	486.5	0.61%
$W'_{tip}$			15.9	16.1	0.78%	
$W'_{toe}$			13.7	13.8	0.99%	
$SC$ (%)			7.4	7.3	-1.3%	
$\Delta Q_f$ (%)			5.3	5.1	-3.6%	
$\alpha_L = 0$ m		$x_{tip}$ (m)	849.1	856.3	0.85%	
		$x_{toe}$ (m)	25.1	25.1	0.28%	

The negative sign in the discrepancy values of Table 3.3 shows that  $SC$  and  $\Delta Q_f$  values decrease when boundary condition (b) is used, whereas the tip and toe tend to increase when boundary condition (b) is used instead of (a). The decrease in  $SC$  by using boundary condition (b) is in agreement with the findings of Smith (2004), in his evaluation of seawater circulation in onshore aquifer settings. Discrepancies in  $x_{tip}$ ,  $x_{toe}$ ,  $W'_{tip}$ ,  $W'_{toe}$  and  $SC$  are not higher than 1.7%, whereas  $\Delta Q_f$  is modified significantly, i.e., the discrepancy equals 14% in Scenario 2 with  $\alpha_L = 1$  m.

## 3.8 Discussion

### 3.8.1 Dispersion effects on offshore interfaces

The different responses of the tip and toe to dispersion, as illustrated in Figure 3.5, are associated with changes in the freshwater-seawater interface slope. For example, the interface tends to become steeper (i.e., the horizontal separation between and toe and tip is reduced) as dispersivity increases. Steepening of the interface with increased dispersivity has been observed previously in onshore aquifers (e.g., Shoemaker, 2003; Abarca et al., 2007; Kerrou and Renard, 2009), and therefore, the same phenomenon in offshore aquifers is somewhat intuitive. The steepening of the interface as dispersivity increases is linked to the loss in density gradient caused by enhanced mixing between freshwater and seawater, as explained by Kerrou and Renard (2009) from their analysis of heterogeneity effects on seawater intrusion in onshore aquifers. They report rotation (steepening) of the interface as dispersivity (as a surrogate for heterogeneity) increases, leading to seaward movement of the toe. In the situation of offshore aquifers, rotation of the interface similarly causes seaward movement of the toe, but there is an accompanying landward movement of the tip in our results.

Unlike the monotonic behavior of  $x_{toe}$ , non-monotonic relationships in  $x_{tip}$  and  $W'_{tip}$  with dispersion are apparent. The complex behavior of  $x_{tip}$  is attributable to the multi-faceted influence of dispersion on the interface. That is, interface rotation occurs as the density effect weakens (causing the tip to move landward, as discussed above), while the same weakening of density effects (i.e., relative to dispersion) tends to push the interface seaward. The latter arises because the buoyancy force of the sea is effectively reduced, at least relative to other forces. The two effects (interface rotation and seaward shift) act on the tip in opposite directions and respond differently to dispersivity changes, leading to the multi-directional behaviour of  $x_{tip}$  observed in Figures 3.5c, 3.5d and 3.5e. The two factors (interface rotation and seaward shift) accompanying enhanced dispersivity both cause seaward movement of the toe, leading to the disparate behaviour of  $x_{toe}$  and  $x_{tip}$ .

The observed behaviour of  $W'_{tip}$  is dependent not only on dispersivity, but also on the  $K:K_z$  contrast, which also brings about enhanced mixing, as observed by Solórzano-Rivas and Werner (2018), and others (e.g., Frind, 1982; Lu et al., 2013; Sebben and Werner, 2016). Both

Frind (1982) and Solórzano-Rivas and Werner (2018) found that the  $K:K_z$  contrast caused enhanced mixing even though they adopted non-dispersive solute transport parameters in their numerical simulations. Dispersivity values and the effect of the  $K:K_z$  contrast are interrelated, because as the interface becomes steeper, the flow lines tend to also steepen, thereby changing the incident angle of flow at the aquifer-aquitard interface. This in turn influences the dispersive effect of refraction across the aquifer-aquitard interface (Sebben and Werner, 2016), creating complex relationships between  $W'_{tip}$ , dispersivity and the  $K:K_z$  contrast. The lower refractive effect under steeper angles at the aquifer-aquitard interface is the most likely cause of the unintuitive reduction in  $W'_{tip}$  as the dispersivity increase in Scenarios 4 and 5. The exact cause of this phenomenon remains an area of continuing research effort. Nevertheless, the important role of the  $K:K_z$  contrast in interface widening adds to the known dispersive phenomena of offshore coastal aquifers. The role of the  $K:K_z$  contrast in the widening of the toe ( $W'_{toe}$ ) is difficult to ascertain and appears much smaller relative to the role of dispersion in controlling  $W'_{toe}$ .

Michael et al. (2016) also found complex relationships between mixing zone extent and the level of heterogeneity. Michael et al. (2016) investigated the influence of geologic heterogeneity on offshore aquifers using three levels of horizontal geologic continuity (levels of heterogeneity). They compared heterogeneous and homogeneous representations of offshore aquifers; however, the same dispersivity was adopted in both cases. Hence, the effect of dispersion on mixing and other interface properties is difficult to ascertain since dispersivity surrogates for heterogeneity in numerical models. Nevertheless, they found in the heterogeneous numerical solutions that there is a non-monotonic relationship between the level of heterogeneity (i.e., low, medium and high) and the area of the mixing zone. If we consider that by increasing dispersivity in our numerical models, we simulate a higher level of local-scale heterogeneity, the interface behaviour observed in our study is generally consistent with that observed by Michael et al. (2016).

Given that empirical corrections to adjust sharp-interface estimates of interface extent to account for dispersion effects have been found for onshore situations (e.g., Pool and Carrera, 2011; Werner, 2017a), we sought similar types of correction factors for offshore aquifer situations. However, the more complex interrelationships among the different factors

controlling offshore freshwater extent, as described herein, confounded our attempts. Namely, we could not find a correlation that applied to all five scenarios. Therefore, dispersive correction factors for modifying sharp-interface estimates of offshore freshwater extent remain unavailable.

### 3.8.2 Dispersion effects on subsea fluxes

#### 3.8.2.1 *Subsea fresh groundwater discharge*

While freshwater flux changes (i.e.,  $\Delta Q_f$ ) increases with dispersion in all scenarios (Figure 3.7), the causal factors leading to differences in  $\Delta Q_f$  between Scenarios have proven difficult to characterise from the results obtained in our investigation. For example,  $\Delta Q_f$  values are largest in Scenario 5 and smallest in Scenario 2, and the relative ranking of  $\Delta Q_f$  curves (e.g., Figure 3.7) are not correlated to any of the parameter combinations (e.g.,  $\mu$ ,  $l_f$ ,  $\beta H/H$ ,  $K:K_z$ ) used to explain other phenomenon.  $\Delta Q_f$  values in Scenario 2 are at least 5 times smaller than in any of the other scenarios. The distinguishing features of Scenario 2, relative to other scenarios, is that Cross section A (i.e., the smaller of the two cross sections used) is adopted and the analytical, sharp-interface solution for Scenario 2 falls into the category of Analytical case II (i.e., the toe is offshore; Figure 3.5). The analytical solutions for Scenarios 1, 3 and 5 produce Analytical case I situations, while Scenario 4 (as with Scenario 2) is an Analytical case II situation. As Scenario 4 produces the second-lowest values of  $\Delta Q_f$ , it appears that the type of analytical case may play an important role in the response of freshwater discharge to the level of dispersion. Additionally, Scenario 1 shows the steepest  $\Delta Q_f$  gradient with respect to dispersion in Figure 3.7. This scenario is the only one where all numerical simulation results but one are onshore (i.e., consistent with the definition of Analytical case I). Other scenarios in which the analytical solution produces Analytical case I-situations have numerical, dispersive interface locations that are offshore (i.e., consistent with the definition of Analytical case II). Thus, in a way, Scenario 1 remains within the definition of Analytical case I, whereas Scenarios 3 (where half of the dispersive interfaces are offshore; see Figure 3.5) and 5 (where all dispersive interfaces are offshore; see Figure 3.5) shift from Analytical case I to II within the simulations undertaken within these scenarios. It would seem from this additional evidence that the analytical case type is related to the behaviour of  $\Delta Q_f$  in response to changes to dispersivity, whereby Analytical case I creates a stronger  $\Delta Q_f$  response to dispersivity changes.

The results given in Figure 3.7 (i.e.,  $\Delta Q_f$  increases with dispersion) indicate that offshore fresh groundwater discharge will be larger in aquifers with greater heterogeneity, if it is presumed that dispersivity typically represents the (unknown) heterogeneity of the porous medium at microscopic-to-local scales in solute-transport modelling. The same effect is unlikely to arise in density-independent solute transport problems, in which the dispersiveness of transport and the magnitude of flow are not coupled through water density variations, in contrast to the solute concentration-dependent velocity field of seawater intrusion problems (e.g., Volker and Rushton, 1982).

### 3.8.2.2 Seawater circulation rates

The relationship between  $\mu$  and  $SC$  shown in Figure 3.8 helps to elucidate the influencing factors driving  $SC$  in offshore aquifers. Smith (2004) proposed the mixed convection ratio  $V^* = KH\delta/Q_f$  to describe the potential for seawater circulation given a known rate of freshwater discharge towards the sea. According to Smith (2004),  $V^*$  relates the characteristic free convection velocity ( $\frac{K\delta}{n_e}$ ) to the characteristic forced convection velocity ( $\frac{Q_f}{Hn_e}$ ) whereby large values of  $V^*$  indicate that buoyancy forces are more dominant relative to advective forces. Badaruddin et al. (2017) used the inverse of  $V^*$  as the mixed convection ratio in their analysis of active seawater intrusion.  $V^*$  is correlated to both  $\mu$  and  $l_f$  (see Section 3.3.1), i.e.,  $\mu = \frac{l_f}{HV^*}$ . Table 3.4 shows the values of  $V^*$ ,  $SC$  and  $l_f$  for the different dispersion values used in each scenario (see Table 3.1 for scenario definitions).

**Table 3.4** Values of  $V^*$ ,  $\mu$  and  $SC$  for each scenario, where values of  $l_f$  are constant

$\alpha_T/H$	Scenario 1			Scenario 2			Scenario 3		
	$l_f = 14.142$ m			$l_f = 22.361$ m			$l_f = 44.721$ m		
	$V^*$	$\mu$	$SC$ [%]	$V^*$	$\mu$	$SC$ [%]	$V^*$	$\mu$	$SC$ [%]
0.001	7.349	0.192	7.0	2.109	1.060	1.8	8.421	0.531	5.0
0.002	7.299	0.194	10	2.106	1.062	2.6	8.355	0.535	6.6
5									
0.005	7.246	0.195	13	2.103	1.063	3.2	8.295	0.539	8.0
0									
0.007	7.209	0.196	15	2.101	1.064	3.6	8.257	0.542	8.8
5									
0.01	7.179	0.197	17	2.100	1.065	3.9	8.229	0.543	9.4
0.025	7.071	0.200	22	2.095	1.067	4.8	8.145	0.549	11
0.05	6.975	0.203	25	2.092	1.069	5.5	8.089	0.553	12
0.1	6.847	0.207	28	2.088	1.071	6.2	8.039	0.556	13
	Scenario 4			Scenario 5					
	$l_f = 500$ m			$l_f = 632.456$ m					
$\alpha_T/H$	$V^*$	$\mu$	$SC$ [%]	$V^*$	$\mu$	$SC$ [%]			
0.002	10.93	0.915	4.5	17.51	0.723	6.3			
0.005	10.84	0.922	5.6	17.29	0.732	7.8			
0.01	10.79	0.927	6.4	17.14	0.738	8.8			
0.02	10.74	0.931	7.0	17.02	0.743	9.4			
0.04	10.70	0.934	7.3	16.94	0.747	9.6			
0.06	10.69	0.935	7.4	16.91	0.748	9.7			
0.08	10.68	0.936	7.6	16.89	0.749	9.7			
0.1	10.67	0.937	7.7	16.87	0.750	9.8			

Table 3.4 demonstrates that for a given scenario (i.e., in which  $l_f$  and  $H$  are maintained constant, and only dispersivity varies),  $\mu$  is inversely proportional to  $V^*$ , and directly related to  $SC$ . However, the same relationship does not exist among the different scenarios (where  $l_f$  and  $H$  vary), where the relationship of  $SC$  with  $\mu$  is inversely correlated, and  $SC$  is non-monotonic with  $V^*$ . These results differ from those reported for onshore settings (e.g., Smith, 2004), where a monotonic relationship between  $SC$  and  $V^*$  was found. For example, while Scenario 3 has higher  $V^*$  values (i.e., 8.039) than Scenario 1 (i.e., 6.847), Scenario 1 has the highest  $SC$  value (see Table 3.4) despite the same dispersivity values (e.g.,  $\alpha_T/H = 0.1$ ) adopted in both scenarios. Therefore, while a higher  $SC$  would be expected for higher values of  $V^*$  in onshore aquifers, the same behaviour may not arise in offshore aquifers. This is because in offshore aquifers, the  $K:K_z$  contrast (affecting  $l_f$ ; see Section 3.3.1) is a significant factor in mixing zone, and therefore  $SC$ , trends.

Figure 3.8 shows a monotonic relationship between  $SC$  and dispersion in all scenarios. That is, the threshold of dispersivity proposed by Smith (2004) for onshore aquifers (i.e.,  $SC$  reduces when  $\alpha_T/H > 0.025$ ) that arises as a consequence of the non-monotonic  $SC$ -dispersion relationship was not observed. The  $SC$ -dispersion relationship for offshore aquifers may become non-monotonic at excessively high values of  $\alpha_T/H$ , but we found no reduction in  $SC$  for  $\alpha_T/H$  up to values of 0.1. Values of  $\alpha_T/H > 0.1$  likely represent physically unrealistic dispersion values (Gelhar et al., 1992).

Previous studies have identified that seawater circulation rates in onshore aquifers are mainly dependent on dispersion (e.g., Smith, 2004; Kerrou and Renard, 2009), and on  $Q_m$  (e.g., Pool et al., 2011). In this study, we have identified that seawater circulation rates in offshore settings depend on the interrelation of  $Q_m$ , dispersion and the  $K:K_z$  contrast. Additionally, Michael et al. (2016) found that multiple circulation cells arose in their heterogeneous models. They concluded that these circulation cells led to seawater circulation rates that would otherwise be less in homogeneous models, implying that homogeneous models are unlikely to create multiple circulation cells. However, we found multiple circulation cells in a selection of our simulations (e.g., in all simulations of Scenario 1), which adds to the findings of Michael et al. (2016).

### 3.8.3 Mixed convection analysis and boundary condition effects

Our mixed convection analysis of alternative Rayleigh number formulations (i.e.,  $Ra_\delta$  and  $Ra^*$ ) was unable to find a critical Rayleigh number that would reliably predict the transition between freshwater and seawater at the top of the aquifer, using non-zero dispersion parameters. This is in contradiction to the sharp-interface analysis of Solórzano-Rivas and Werner (2018). That is, the results depicted in Figure 3.9 indicate that the value of  $Ra_\delta$  equal to 2 proposed by Solórzano-Rivas and Werner (2018) for sharp-interface conditions does not apply in dispersive situations. Nonetheless,  $Ra_\delta$  approximately equal to 2 was obtained consistently in our non-dispersive simulations, in agreement with Solórzano-Rivas and Werner (2018). The decrease in Rayleigh numbers (i.e.,  $Ra_\delta$  and  $Ra^*$ ) as dispersivity increases demonstrates that buoyancy forces are dissipated (relative to advective forces) by dispersive mechanisms. This is consistent with the steepening of the interface slope and the generally seaward movement of the interface (at least in terms of the toe) as dispersivity increases, as illustrated in Figure 3.5.

Smith (2004) found that the type of concentration boundary condition had an important effect on onshore aquifers; namely, seawater circulation rates may be up to 1.6 times higher if the mass flux across the seafloor boundary depends on the ambient concentration instead of a constant concentration that produces accumulation of salt beneath the boundary. In our study, none of the simulated models using the constant concentration condition produced unphysical accumulation of salt in the aquitard in areas where freshwater discharges to the seafloor. This is most likely a consequence of the reduced dispersivity applied to the aquitard, whereas Smith (2004) adopted uniform dispersion parameters in his cases.

The choice of concentration boundary condition representing the seafloor had little impact on the interface location, the width of mixing zones and the seawater circulation rates, whereas a significant boundary condition effect was observed in terms of freshwater fluxes to the sea (see Table 3.3). The finding that the type of seafloor boundary condition affects freshwater discharge to the sea adds to Smith's (2004) conclusions about boundary condition effects of seawater circulation. Smith (2004) used specified-flux conditions at the onshore boundary, whereas in this study we used specified-head conditions, which allowed for the influence of boundary conditions and other factors on freshwater discharge to be evaluated. For the case when non-dispersive solute transport parameters were adopted, the interface toe location was hardly influenced (i.e., up to 2.1%; see Table 3.3) by the choice of offshore solute boundary condition. Therefore, the results of Solórzano-Rivas and Werner (2018) results are not dependent on their choice of boundary condition (i.e., flow direction-dependent salt mass flux).

### 3.9 Conclusions

The present study determined the effect of dispersion on the interface of subsea aquifers that contain fresh and saline groundwater. Dispersive numerical simulations of offshore groundwater flow have shown that the tip and toe respond differently to changes in dispersion. Increasing dispersivity resulted in more seaward toe positions, in a similar manner to that observed in the more widely studied onshore case. Conversely, the effect of dispersion on the tip location cannot be easily anticipated because of the non-monotonic relationship between dispersivity and  $x_{tip}$ . Surprisingly,  $W'_{tip}$  follows a non-monotonic relationship with dispersion, in a similar fashion to  $x_{tip}$ , such that a maximum value is reached with increasing dispersivity,

after which  $W'_{tip}$  decreases as dispersivity increases. This counterintuitive narrowing of the interface (at the tip) with dispersivity is caused by the dispersive effect of refraction across the aquifer–aquitard interface. Specifically, refractive dispersion strengthens when the incident angle is higher (or less steep), which occurs when the aquifer dispersion parameters are lower.

Given our inland boundary condition (i.e., specified head), it has been possible to investigate the dispersion effect on fresh groundwater discharge towards the sea (i.e.,  $Q_{fn}$ ), finding that larger dispersivity values cause increased  $Q_{fn}$ . Considering that dispersivity surrogates for heterogeneity, this indicates that heterogeneity plays an important role in fresh groundwater flow rates in density-coupled systems. The results also show that  $Q_{fn}$  is related to the type of analytical case (i.e., the four tip-toe situations defined by Bakker, 2006), whereby greater changes in  $Q_{fn}$  occur when dispersivity is increased if the interface is classified within the Analytical case I (i.e., the toe is onshore).

Seawater circulation rates show a monotonic relationship with dispersion, differing from the non-monotonic relationship observed in onshore aquifers by Smith (2004). This finding indicates that the critical dispersion value, whereby the influence of buoyancy forces on seawater circulation rates diminishes, differs from that proposed by Smith (2004) for onshore settings. This is mainly due to the influence of the aquifer-aquitard interface on dispersion effects, affecting  $SC$ . This study adds to the current body of knowledge on seawater circulation in coastal aquifers by demonstrating that  $SC$  in offshore settings is correlated to the  $K:K_z$  contrast, in addition to the  $SC$  parameter-dependencies identified in onshore coastal aquifer studies.

Other factors investigated in this study, including the evaluation of mixed-convective processes, demonstrate that the  $Ra_\delta$  proposed by Solórzano-Rivas and Werner (2018) for the sharp-interface simplification in offshore aquifers does not apply in dispersive conditions. This is because dispersion effects reduce the influence of buoyancy forces driven by density gradients, thereby lowering  $Ra_\delta$  as dispersivity increases. Additionally, it has been shown that the type of concentration boundary in subsea aquifers (for model set-ups similar to ours) likely have negligible effect on salinity distributions and seawater circulation rates, but may impact significantly the estimations of freshwater flow towards the sea.

Our attempts to find a dispersive correction factor to sharp-interface estimates that can be applied to all five scenarios were not successful. Further efforts may need to consider seeking dispersive correction factors for individual analytical case. More generally, the results presented in this analysis show that the response to dispersion of onshore aquifers do not necessarily apply to offshore aquifers, primarily due to the influence of the aquifer-aquitard boundary, which contributes significantly to the interplay between dispersive, buoyancy and advective forces. That is, refraction at the aquifer-aquitard boundary play a major role in controlling the extent of freshwater and freshwater-seawater mixing in the offshore aquifer.

## Chapter 4

### **Mixed-convective processes within seafloor sediments arising from fresh groundwater discharge**

Accepted for publication in *Frontiers in Environmental Science*: Solórzano-Rivas, S. C., Werner, A. D., Irvine, D. J. Mixed-convective processes within seafloor sediments arising from fresh groundwater discharge, 9. doi: 10.3389/fenvs.2021.600955.

*Approximate contribution of co-authors: S.C. Solórzano-Rivas (65%); Adrian Werner (25%); Dylan Irvine (10%).*

#### **4.1 Abstract**

The dependence of near-shore ecosystems on the freshwater component of submarine groundwater discharge (SFGD) is well recognized. Previous studies of SFGD have typically assumed that SFGD occurs through aquitards that are in direct contact with seawater. These studies provide no guidance on the distribution of freshwater discharge to the seafloor where SFGD occurs through sandy sediments, even though in most situations, seabed sediments are permeable. We find that SFGD may occur in unconfined, seafloor sediments as density-driven flow in the form of fingers, or otherwise, diffusive freshwater discharge is also possible. Unstable, buoyancy-driven flow within seabed sediments follows similar patterns (except inverted) to the downward free convection of unstable (dense over less-dense groundwater) situations. Consequently, the same theoretical controlling factors as those developed for downward mixed-convective flow are expected to apply. Although, there are important differences, in particular the boundary conditions, between subsea freshwater-seawater interactions and previous mixed-convective problems. Simplified numerical experiments in SEAWAT indicate that the behavior of fresh buoyant plumes depends on the aquifer lower boundary, which in turn controls the rate and pattern of SFGD to the seafloor. This work provides an important initial step in the understanding of SFGD behavior in regions of sandy seafloor sediments and analyses for the first time the mixed-convective processes that occur when freshwater rises into an otherwise saline groundwater body.

## 4.2 Introduction

Subsea fresh groundwater discharge (SFGD) is the release of freshwater from seafloor sediments, and has been identified as an important means to transport dissolved nutrients to the ocean, thereby having a significant influence on marine ecology and benthic organisms (e.g., Johannes, 1980; Moore, 1999). Knowledge of the salinity patterns in subsea sediments is important for several reasons, including for the understanding of benthic ecosystems in regions of SFGD, and for the design of SFGD measurement approaches. The distribution of groundwater discharge to the sea depends on the characteristics of geological formations. Fresh groundwater discharge to intertidal zones is often associated with unconfined aquifers, whereas SFGD, occurring beyond the intertidal zone, typically requires low-permeability confining units that act to limit freshwater-seawater mixing that would otherwise occur near the shoreline (e.g., Jiao et al., 2015; Michael et al., 2016). Predictions of the extent of subsea fresh groundwater typically assume that the low-permeability layers that preserve freshwater and allow SFGD to occur are in direct contact with seawater (e.g., Kooi and Groen, 2001; Bakker et al., 2017; Solórzano-Rivas and Werner, 2018; Werner and Robinson, 2018; Solórzano-Rivas et al., 2019). However, the seafloor more often comprises high-permeability sediments (>50% of the global shelf sediments have high permeability; Riedl et al., 1972). Yet, this configuration has not been widely considered in studies of SFGD.

The occurrence of freshwater in high-permeability sediments overlain by seawater, as occurs when SFGD passes through permeable seafloor sediments, creates a mixed-convective condition. That is, flow processes are expected to be controlled by both buoyancy-driven flow (i.e., free convection) driven by water density differences and hydraulic-driven flow (i.e., forced convection) arising from groundwater heads in subsea sediments that exceed those of the sea. Thus, solute distributions in subsea aquifers may resemble those of other mixed-convective situations. However, studies of mixed-convective or free-convective processes where buoyancy is created by salinity gradients usually involve descending plumes of higher-density fluid that contaminate underlying lower-density groundwater (e.g., Webster et al., 1996; Smith and Turner, 2001; Stevens et al., 2009; Xie et al., 2011). Conversely, the upward movement of lower-density groundwater (e.g., as expected to arise during SFGD) is rarely explored in the solute transport context, although upward, buoyancy-driven groundwater flow has received significant attention in the field of heat transport and geothermal phenomena. For example,

Kurylyk et al. (2018) utilized temperature-based methods to quantify submarine groundwater fluxes in seafloor sediments offshore of eastern Canada. However, their study suggested that the flow patterns inferred from seafloor temperature-depth profiles appear to be influenced by both density-driven and geothermal processes.

Perhaps the most pertinent prior investigation of mixed-convective transport accompanying SFGD is that of Moore and Wilson (2005), who were perhaps the first to recognize that SFGD may be driven by upward buoyancy forces. Based on temperature measurements of subsea groundwater (1.5 m below the seabed), Moore and Wilson (1990) interpreted that a sudden drop in the ocean temperature produced upward motion of warmer (i.e., less dense) groundwater to the ocean. However, previous research offers little guidance on the characteristics of free-convective or mixed-convective flow within seafloor sediments. In particular, whether mixed-convective flow within seafloor sediments can be characterized according to buoyancy theory developed for other unstable, solute transport conditions (e.g., leading to downward-moving fingers of higher density; e.g., Wooding et al., 1997) is unclear. This includes the application of several dimensionless variables that are used to categorize mixed-convective problems (e.g., Wooding et al., 1997; Simmons et al., 2010). Additionally, to our knowledge, no quantitative evaluation of mixed convection driven by the upward movement of lower-salinity groundwater has been reported in the literature. Rather, upward convection of lower-density groundwater has only been explored where buoyancy is created by temperature gradients (e.g., Irvine et al., 2015).

The aim of this study is to undertake a review of the existing buoyant theory, including non-dimensional numbers used to characterize mixed-convective flow, and explore whether this theory can be applied to SFGD through high-permeability seafloor sediments. A small number of highly idealized numerical simulations are used to provide an initial demonstration of freshwater-seawater mixing accompanying the rise of fresh buoyant plumes through permeable seafloor sediments. We expect that the upward movement of less-dense groundwater will show similar, albeit inverted, characteristics (e.g., buoyancy-driven fingers of freshwater) to the downward movement of more dense saltwater that has been comprehensively assessed in numerous prior investigations. The scope of this study does not include a systematic approach

to evaluate the controlling factors in the mixed-convective flow processes derived from SFGD through sandy seafloor sediments.

### 4.3 Conceptual model

Two hypothetical conceptual models of SFGD are considered, both of which involve freshwater-seawater mixing within high-permeability, seabed sediments, as shown in Figure 4.1. Model A represents the situation where the seafloor sediments are underlain by a higher-permeability freshwater source, whereas Model B involves underlying sediments of lower permeability (i.e., an aquitard). The former is intended to reflect the situation of SFGD where an underlying aquifer sub-crops to the seafloor and is overlain by sand, while the latter represents SFGD passing through a leaky aquitard into more permeable seafloor sediments.

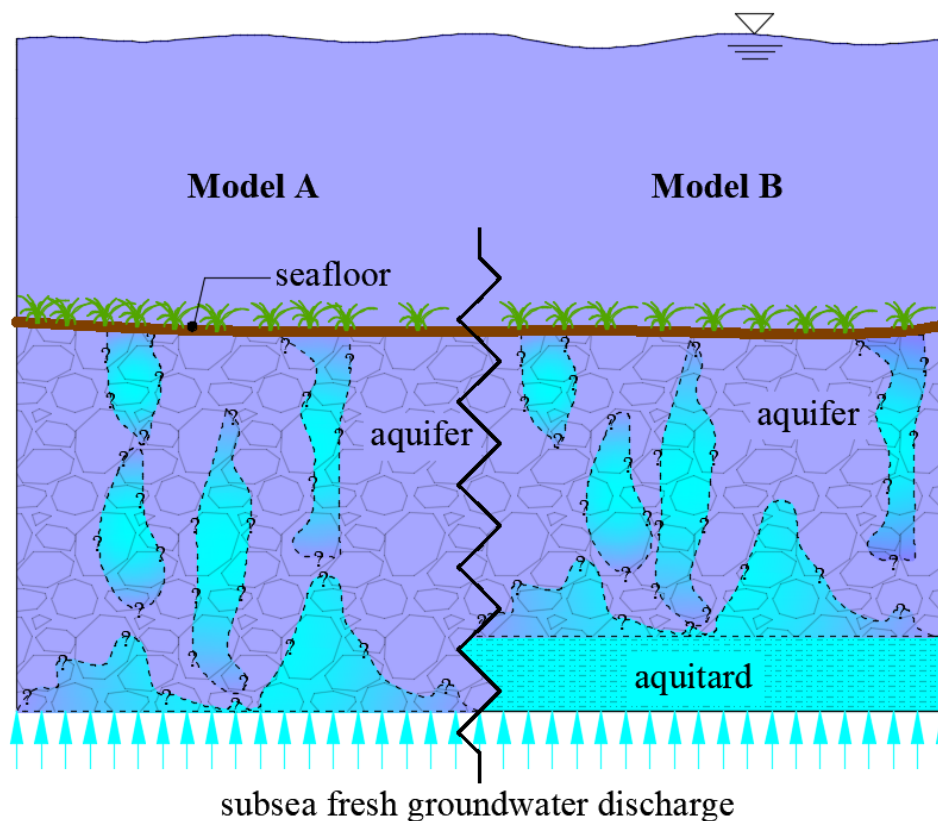


**Figure 4.1** Two conceptual models of a subsea unconfined aquifer subject to SFGD. Blue is freshwater, and purple is seawater. Model A (left) involves sandy sediments overlying a subcropping, higher-permeability aquifer, and Model B represents an aquitard overlain by sand.

An important unknown for the conceptual models considered here is the distribution of freshwater within the seafloor sediments. While Figure 4.1 shows buoyant freshwater plumes that take the shape of fingers, similar to classic unstable flow patterns for downward free convection, freshwater-seawater mixing may alternatively be dominated by dispersive process (at least theoretically), leading to different salinity patterns to those represented in Figure 4.1. Most field studies of SFGD adopt methods that assume that SFGD occurs in a distributed form (i.e., presuming dispersive freshwater-seawater mixing in seafloor sediments), with devices located on the seafloor (i.e., seepage meters) in regular grid patterns (e.g., Taniguchi et al., 2003; Michael et al., 2005; Kurylyk et al., 2018). However, the buoyant freshwater plumes that are hypothesized here (Figure 4.1) may require alternative measurement strategies. For example, the spacing between, and size of, freshwater plumes, should they occur, may influence the deployment of seepage meters.

Although freshwater plumes within seafloor sediments are expected to behave similarly to the well-studied downward-moving saltwater plumes of prior studies (e.g., Xie et al., 2011), there are important differences between the conceptual model of Figure 4.1 and previous analyses of downward-moving plumes. Consider for example the Elder problem (e.g., Elder et al., 2017), which was transformed to free-convective solute motion by Voss and Souza (1987), and is a common benchmarking problem for assessing numerical models. Various modifications of the Elder problem have occurred to explore other aspects of free convection problems. For example, Xie et al. (2010) introduced mechanical dispersion and changed the lower boundary condition to represent more realistic conditions, similar to the approach of Post and Kooi (2003). The conceptual model applied to SFGD (Figure 4.1) is, conceptually at least, an ‘inverse’ of the solute-based Elder problem, where the aquifer is initially seawater-filled and a source of constant freshwater is introduced at the bottom boundary. The initial seawater conditions in the aquifer allow for the transience of salinization to be observed. However, the boundary conditions differ to those of the Elder problem to improve the representation of the expected SFGD process. That is, specified-head boundaries are imposed at the top (seawater) and the bottom (freshwater), whereas the Elder problem uses no-flow boundary conditions at all edges and specified hydraulic heads at the top corners (e.g., Guo and Langevin, 2002). Thus,

the behavior of SFGD within seafloor sediments, under the conditions presented in Figure 4.1, cannot be inferred from previous studies. Further details of numerical models are provided in Section 4.5.

#### 4.4 Review of mixed-density non-dimensional numbers applicable to SFGD through seafloor sandy sediments

The characterization of buoyancy-induced flow associated with unstable systems has been the subject of extensive research. One of the most common non-dimensional numbers applied for this purpose is the Rayleigh number ( $Ra$ ) (e.g., Simmons et al., 2010).  $Ra$  is the ratio between buoyancy forces (inducing instabilities in the form of solute fingers) and dispersion forces (tending to resist the formation of unstable solute fingers). When freshwater and seawater interact,  $Ra$  can be defined as (e.g., Post and Koi, 2003):

$$Ra = \frac{K\Delta\rho H}{\rho_f D} \quad (4.1)$$

where  $K$  is the aquifer hydraulic conductivity [ $L T^{-1}$ ],  $\Delta\rho$  is the difference between the seawater ( $\rho_s$ ) and freshwater ( $\rho_f$ ) densities [ $M L^{-3}$ ],  $H$  is the aquifer thickness [ $L$ ], and  $D$  is hydrodynamic dispersion [ $L^2 T^{-1}$ ].  $D$  is equal to the sum of molecular diffusion ( $D_0$ , [ $L^2 T^{-1}$ ]) and mechanical dispersion, which is often simplified to  $\alpha_L v_L$ , where  $\alpha_L$  is the longitudinal dispersivity [ $L$ ] and  $v_L$  the advective flow velocity [ $L T^{-1}$ ] (i.e., transverse dispersivity,  $\alpha_T$ , is often neglected).

There are several alternative  $Ra$  formulations that have been reported in the literature. For example, some studies have presumed that  $D$  consists only of  $D_0$ , with mechanical dispersion neglected (e.g., Post and Kooi, 2003; Stevens et al., 2009; Simmons et al., 2010; Xie et al., 2011). These cases involve only free convection, i.e., hydraulic-driven convection is not considered. Alternative expressions for  $Ra$  have been developed for mixed-convection processes. For example, in mixed-convective problems examined by Simmons and Narayan (1997) and Smith and Turner (2001), both mechanical dispersion and molecular diffusion were included in their definitions of  $D$ . However, Simmons and Narayan (1997) adopted  $\alpha_T$  and Smith and Turner (2001) adopted  $\alpha_L$  in defining  $D$ . This study adopts the Smith and Turner (2001) definition of  $D$ .

The value of  $Ra$  has been used to predict the occurrence of unstable solute motion, typically in the form of solute fingers (e.g., Wooding et al., 1997). The critical  $Ra$  is defined as the threshold value at which buoyancy forces overcome dispersion forces that inhibit finger formation. This threshold value differs depending on conditions in which free convection occurs. For example, in the case of free convection in hydrogeological settings, Stevens et al. (2009) and Moore and Wilson (2005) refer to the critical  $Ra$  of  $4\pi^2$  (i.e., for the appearance of solute fingers) reported by Lapwood (1948) for temperature gradients in porous media. However, alternative critical  $Ra$  values are offered by other authors for free convection problems. According to van Reeuwijk et al. (2009), the historical incongruency in critical  $Ra$  estimates is related to such aspects as the numerical approach, governing equations, and slight differences in the initial conditions. They suggest that the critical  $Ra$  for free convection involving solutes is zero (in other words, solute fingers form without the need for a ‘dispersive boundary layer’; see below).

Applications of  $Ra$  theory to mixed-convective processes include the study of Simmons and Narayan (1997), who imposed linearly varying hydraulic heads across the top boundary, to induce lateral flow (i.e., flow parallel to the solute source boundary). The transverse dispersion created by this lateral flow was incorporated into the stabilizing dispersive force in assessing the critical  $Ra$ . By incorporating  $\alpha_{TVL}$  in  $D$ , Simmons and Narayan (1997) include forced convection (i.e.,  $v_L$ ) in the definition of  $Ra$ . They found that the critical  $Ra$  ranged between 300 and 500 under these conditions. Smith and Turner (2001) considered a somewhat similar situation to that of Simmons and Narayan (1997), except fresh groundwater discharged to the upper solute boundary condition (i.e., the estuary) in Smith and Turner’s (2001) analysis of estuary-aquifer interaction. They obtained a critical  $Ra$  value of 5 for the onset of finger development. Solórzano-Rivas and Werner (2018) adopted the Smith and Turner (2001) formulation for the analysis of freshwater discharge through subsea aquifers, and found a critical  $Ra$  of about 2 for the salinization of submarine aquitards overlying fresh offshore aquifers. The application of  $Ra$  to mixed-convection problems introduces challenges in establishing general values for the critical  $Ra$ , given differences in the representation of forced convection in defining  $Ra$  across the abovementioned studies.

Wooding et al. (1997) analyzed the development of boundary layers within mixed-convective flow systems (i.e., where freshwater flows upwards towards a saltwater boundary; see Plate 1

figure in Wooding et al. (1997)). They derived an expression for the steady-state boundary layer thickness,  $\delta$  [L], defined as the thickness of solute formed (by dispersion) in the presence of upward freshwater flow,  $q_z$  [L T<sup>-1</sup>], as:

$$\delta = \frac{D_0}{q_z} \quad (4.2)$$

Wooding et al. (1997) combined equations (4.1) and (4.2), by equating  $H$  to  $\delta$  (i.e., conceptually, this is the case where the boundary layer encompasses the entire aquifer thickness), to define a boundary-layer Rayleigh number,  $Ra_\delta$ , namely:

$$Ra_\delta = \frac{K\Delta\rho\delta}{\rho_f D} \quad (4.3)$$

The critical  $Ra_\delta$  is therefore defined by the thickness of  $\delta$  that leads to the onset of unstable solute fingers. Wooding et al. (1997) undertook laboratory experiments using a Hele-Shaw cell to determine the critical  $Ra_\delta$ , including different rates of lateral inflow at the right boundary and vertical outflow to the top, and using various inclination angles of the cell. They also performed numerical experiments that reproduced the two-dimensional flow and solute transport behavior observed in the Hele-Shaw experiment. From the laboratory and numerical experiments, they found  $Ra_\delta$  values between 8.9 and 9.8, concluding that a good estimate for the critical  $Ra_\delta$  is approximately 10.

Another widely used non-dimensional parameter for the characterization of mixed-convective processes is the mixed convection ratio ( $M$ ).  $M$  describes the relationship between buoyancy-driven forces and hydraulic-driven forces as (e.g., Simmons et al., 2010):

$$M = \frac{\left(\frac{\Delta\rho}{\rho_f}\right)}{\left(\frac{\Delta h}{\Delta l}\right)} \quad (4.4)$$

where  $\frac{\Delta h}{\Delta l}$  [-] is the hydraulic gradient over a distance  $\Delta l$ . An alternative expression for  $M$ , through substitution of Darcy's Law, is given by Smith (2004), as:

$$M = \frac{K\Delta\rho}{\rho_f q_z} \quad (4.5)$$

By combining equations (4.2) and (4.3), it is apparent that  $Ra_s$  and the formulation for  $M$  given in (3.5) are the same, i.e.,  $M = Ra_s$ . Surprisingly, this has not been reported previously to the authors' knowledge. The implications of this are that critical values for  $Ra_s$  also apply to  $M$ . However, there is no evidence that the equilibrium value of  $M = 1$  suggested by Simmons et al. (2010) (whereby if  $M$  is larger than 1 the problem is said to be free-convection dominated, and forced convection is thought to be the dominant process if  $M$  is less than 1) has application in terms of  $Ra_s$ . That is,  $Ra_s = 1$  has not been reported as a significant value previously. It follows that the onset of instabilities is not predictable through comparison of free and forced convective forces (i.e., through the use of  $M$ ), as expected given the role that dispersion plays in instability initiation. Nevertheless, Stevens et al. (2009) applied  $M$  to the assessment of the occurrence of unstable solute fingering processes that accompany free convection on Padre Island (USA). The site experiences intense evaporation rates and shallow water table conditions, creating large density gradients and low horizontal hydraulic gradients. They found values of  $M$ , based on application of equation (4.4), that were much larger than 1 (i.e., by one and two orders of magnitude), although numerical values of  $M$  were not reported. Stevens et al. (2009) interpreted unstable flow structures from resistivity surveys, although these were difficult to conclusively establish. Thus, the application of  $M$  to the prediction of unstable fingering remains unproven.

#### **4.5 Numerical simulation of SFGD**

Here, the conceptual models illustrated in Figure 4.1 are adopted, except the situation is assessed whereby the sandy seafloor sediments are presumed to be originally filled with seawater. Numerical modeling, using SEAWAT (governing equations are found in Guo and Langevin, 2002; not repeated here for brevity), was used to assess two simple situations of SFGD through sandy seafloor sediments. The two cases (Models A and B; see Figure 4.2) involve contrasting mixed-convective forces arising from the inclusion or omission of an underlying aquitard. This is reflected in the corresponding values of  $Ra$  and  $Ra_s$ , which are reported for each case and compared to previously reported critical values (Wooding et al., 1997; Smith and Turner, 2001) in Section 4.4. The calculation of  $Ra$  and  $M$  for Model B does not include the aquitard thickness (i.e., only  $H$  is regarded as per the formula (1) definition).

Figure 4.2 is a simplified section showing two possible configurations of a subsea aquifer subjected to SFGD, which is homogeneous, isotropic, and of length  $L$  [L] and thickness  $H$  [L]. The upper boundary represents seawater immediately above the seafloor, simulated by a high hydraulic conductivity (i.e., 100,000 m/d) and a specified-head condition equal to  $z_s$ , assigned to the top row of the model. SEAWAT converts  $z_s$  to a constant pressure (Langevin et al., 2008) reflecting the column of overlying seawater, of density  $\rho_s$ . The solute concentration condition in this top layer depends on the flow direction, whereby seawater concentration (i.e., solute concentration = 1) was assigned to any inflowing water, whereas discharge to the sea occurs at the ambient groundwater concentration. This type of solute concentration condition avoids salt accumulation at the boundary in an unrealistic manner (i.e., upstream dispersion; Irvine et al., 2021) and is consistent with the approach of Solórzano-Rivas and Werner (2018). The lower freshwater boundary condition differs between Models A and B. In Model A, the lower boundary reflects a situation where an underlying layer of higher permeability occurs, containing freshwater. That is, there is no restriction to the entry of freshwater through the lower boundary of Model A, represented by a specified-head condition equal to  $h_f$ , which was converted to a constant pressure (by SEAWAT) based on a water density of  $\rho_f$ , as shown in Figure 4.2. In Model B, the lower boundary is composed of lower-permeability sediments (i.e., reflecting aquitard material) of thickness  $H_i$ , with the specified head  $h_f$  imposed on the bottom row of the model (i.e., the base of the aquitard). The solute concentration of the lower boundary for both Models A and B was set to freshwater (i.e., solute concentration = 0), although this depends on the flow direction in a similar manner to the upper boundary.

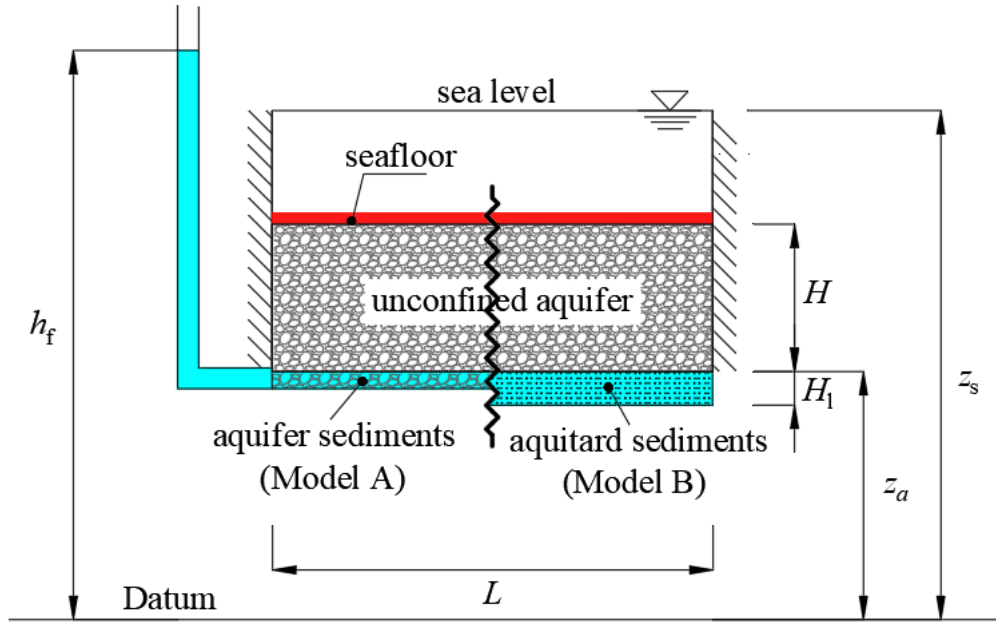


**Figure 4.2** Conceptual models for the numerical implementation of SFGD through an unconfined subsea aquifer, where the left side shows sandy sediments overlying a subcropping, higher-permeability aquifer, and Model B represents an aquitard overlain by sand. Red and blue represent seawater and freshwater boundary conditions, respectively. The equivalent freshwater head at the base of the aquifer, when the aquifer is seawater-filled (i.e., the initial condition), is shown as  $h_f$ .

No-flow boundaries on the left and right edges of the model domain reflect mostly vertical flow processes. Post et al. (2007) and Langevin et al. (2008) offer the following formulation for vertical flow,  $q_z$ , under mixed-density conditions:

$$q_z = -K \left[ \frac{\Delta h_f}{\Delta l} + \frac{\rho_a - \rho_f}{\rho_f} \right] \quad (4.6)$$

where  $\rho_a$  is the average density between  $\rho_s$  and  $\rho_f$  [ $M L^{-3}$ ] and  $\frac{\Delta h_f}{\Delta l}$  is the hydraulic gradient (in terms of equivalent freshwater heads) over a distance  $\Delta l$ .

The aquifer is assumed to be initially full of seawater but is underlain by a fresh groundwater source. The lower boundary head of both models is chosen so that the initial condition is hydraulically stable, primarily to reflect the free-convective situation (i.e., neglecting forced convection) that occurs in the Elder problem and its many variants, thereby providing opportunities to compare upward buoyancy-driven flow to the downward movement of solute

fingers observed by others (e.g., Xie et al., 2011). That is, the hydraulic head of the fresh groundwater source is equal to the equivalent freshwater head,  $h_f$ , at the bottom of aquifer (at the beginning of each scenario). Considering an initial seawater hydrostatic condition,  $h_f$  is given by  $\frac{\rho_s}{\rho_f} z_s - \frac{\rho_s - \rho_f}{\rho_f} z_a$  (where  $z_s$  and  $z_a$  are defined in Figure 4.2). Consequently, the only forces driving flow (initially) are buoyancy forces, because the hydraulic gradient is initially zero. Thus, at the beginning of the scenarios, equation (4.6) reduces to:

$$q_z = -K \left[ \frac{\rho_a - \rho_f}{\rho_f} \right] \quad (4.7)$$

Equation (4.7) is usually referred to as the convective velocity (e.g., Simmons et al., 2010). Vertical flow velocities in the numerical model, from the initial time-step, were found to be consistent with equation (4.7) (results not shown for brevity).

Although the initial condition is a free convective condition, density changes due to the introduction of freshwater through the lower boundary create head gradients that induce boundary inflows, and the system becomes mixed convective. This differs to the free convection Elder problem, which is bounded by no-flow conditions, including the upper salt source boundary. Thus, although our situation is initially free convective, the situation becomes mixed convective during the course of simulations.

The model is a two-dimensional domain represented by a finite-difference grid of uniform discretization, both vertically and horizontally, of  $\Delta z = \Delta x = 0.1$  m. Three cases are evaluated for each model (i.e., a total of six numerical simulations) to briefly explore the role of dispersion in the mixed-convective processes associated with SFGD through the seafloor sediments, namely a Base Case with  $\alpha_L = 0.1$  m, Case 1 with  $\alpha_L = 0.5$  m and Case 2 with  $\alpha_L = 1$  m. These values fall within the range of “moderate” and “high” reliability values recommended by Zech et al. (2015). The criteria to define “moderate” and “high” reliability dispersivity values is given in Gelhar et al. (1992). Other parameters used in all three cases for Model A are:  $\{H, L, z_a, z_s, h_f, K, \rho_f, \rho_s, D_0, \alpha_L/\alpha_T, \varepsilon\} = \{50 \text{ m}, 100 \text{ m}, 80 \text{ m}, 160 \text{ m}, 162 \text{ m}, 2.5 \text{ m/d}, 1000 \text{ kg/m}^3, 1025 \text{ kg/m}^3, 8.64 \times 10^{-5} \text{ m}^2/\text{d}, 10, 0.2\}$ , where  $\varepsilon$  [-] is effective porosity. The three cases of Model B differ to those of Model A in that  $K_a$  is 0.001 m/d and  $H_l$  is 1 m, where  $K_a$  is the aquitard hydraulic conductivity. The parameters adopted here correspond to typical, field-scale values

used in other SFGD-related studies (e.g., Solórzano-Rivas and Werner, 2018; Knight et al., 2018). Timescales for numerical models to reach steady state or quasi-steady state conditions differed between Models A and B, as shown in Section 4.6. Consequently, Model A was simulated for 5 years and Model B for 100 years. Timescales for freshwater to reach the seafloor depend on the velocities of rise of buoyant freshwater fingers. We adopted the tip of the highest buoyant finger (HBF) to characterize mixed convective velocities (assuming time-constant velocities) in a similar way to the approach of Xie et al. (2011). The tip was defined by the 0.85 isochlor (i.e. 85% of seawater concentration).

## **4.6 Results and discussion**

### **4.6.1 The influence of the lower boundary**

Figures 4.3, 4.4 and 4.5 show simulations results from the Base Case, Case 1 and Case 2, respectively. Each figure presents the results of Model A (i.e., where no aquitard is included; left column) and Model B (i.e., where an aquitard underlies the aquifer; right column) at different times. The bottom row in all three figures represents the steady-state conditions, which in the case of Model B is a dynamic equilibrium, also referred to as quasi-steady state. That is, the Model B distribution of SFGD within seafloor sediments is temporally unstable, involving finger patterns that change in time.

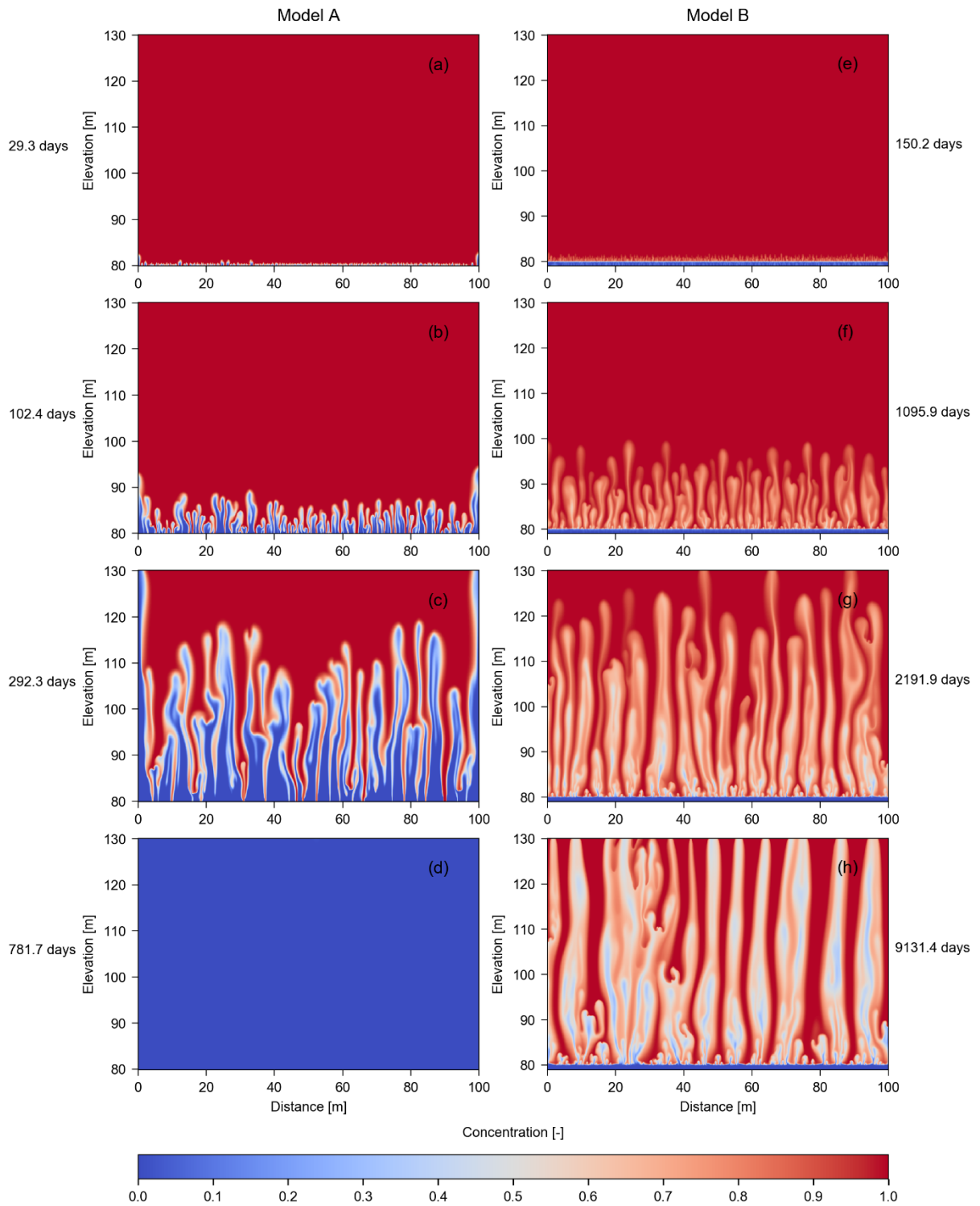


**Figure 4.3** Salinity distributions in seafloor sediments obtained from simulations of the Base Case (i.e.,  $\alpha_L = 0.1$  m;  $\alpha_T = 0.01$  m) of Model A (left column) and Model B (right column). Concentration values represent the relative seawater concentration, where 0 and 1 are freshwater and seawater, respectively. The bottom left subplot depicts steady state results, while the bottom right subplot shows a quasi-steady state salinity distribution.

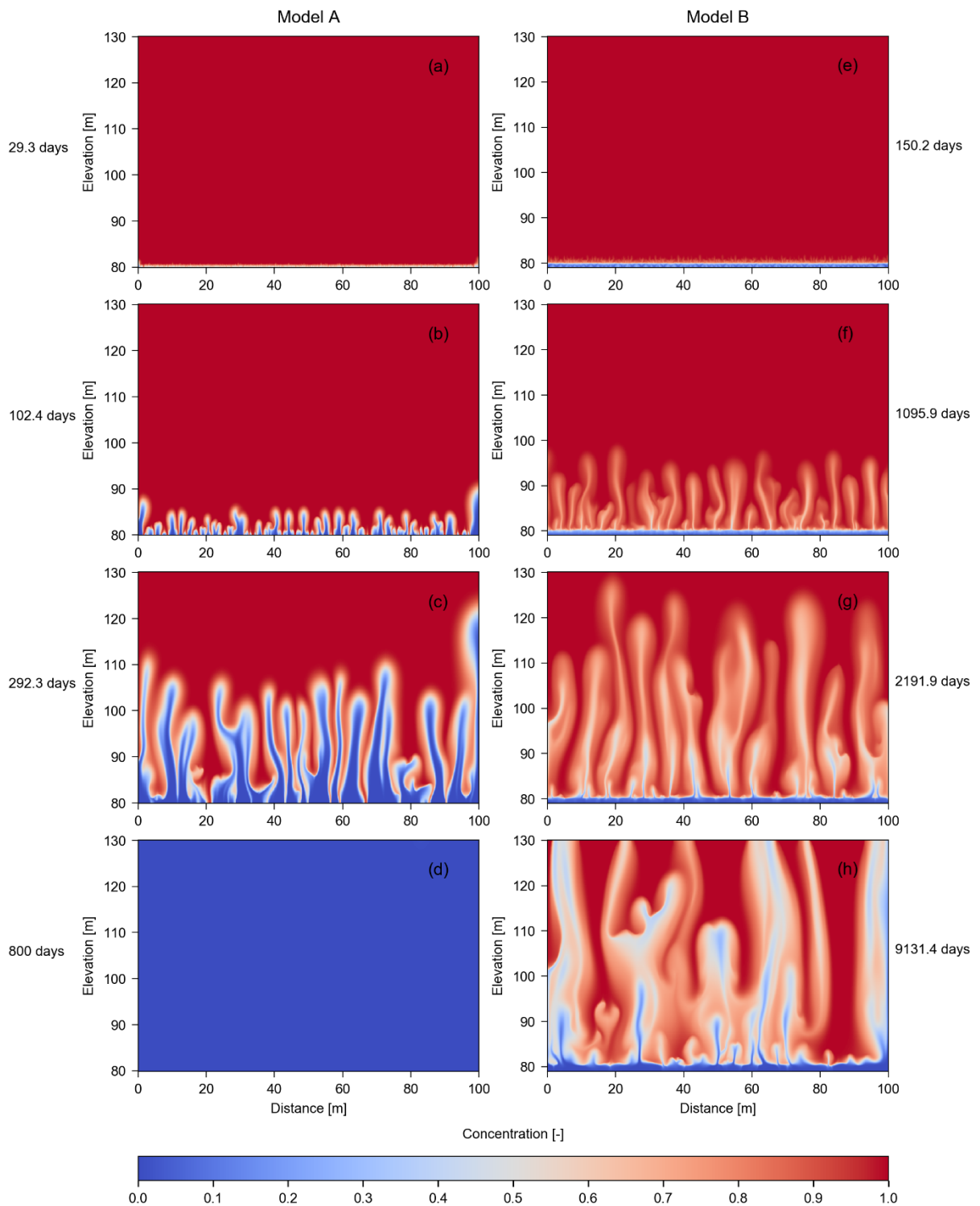


**Figure 4.4** Salinity distributions in seafloor sediments obtained from simulations of Case 1 (i.e.,  $\alpha_L = 0.5$  m;  $\alpha_T = 0.05$  m) of Model A (left column) and Model B (right column). Concentration values represent the relative seawater concentration, where 0 and 1 are freshwater and seawater, respectively. The bottom left subplot depicts steady-state results, while the bottom right subplot shows a quasi-steady state salinity distribution.

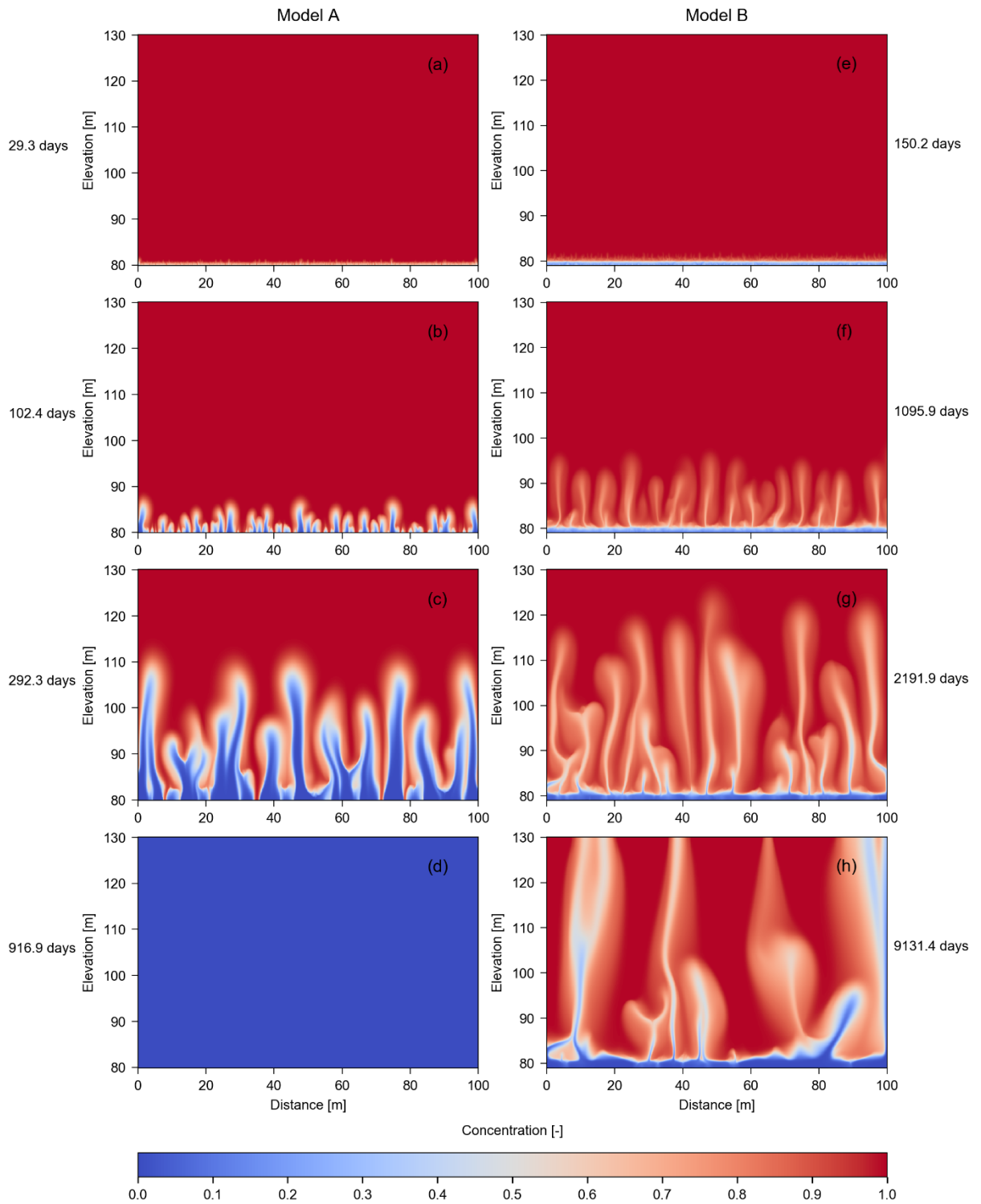


**Figure 4.5** Salinity distribution in seafloor sediments obtained from simulations of Case 2 (i.e.,  $\alpha_L = 1$  m;  $\alpha_T = 0.1$  m) of Model A (left column) and Model B (right column). Concentration values represent the relative seawater concentration, where 0 and 1 are freshwater and seawater, respectively. The bottom left subplot depicts steady-state results, while the bottom right subplot shows a quasi-steady state salinity distribution.

Figures 4.3 to 4.5 highlight substantial differences in mixed-convective processes caused by the existence (or not) of a leaky aquitard below the subsea aquifer. The most important difference between Models A and B, in the context of SFGD characteristics, is that unstable solute patterns persist under quasi-steady state in Model B, whereas in Model A, the flow instabilities are temporary, and the system reaches a steady state condition in which the aquifer is completely fresh. The occurrence of the leaky aquitard creates other important differences in mixed convective processes. For example, freshwater fingers produced from Model A are fresher, for fingers of a comparable height, to those produced by Model B (e.g., Figures 4.3c and 4.3g). This leads to sharper freshwater-saltwater interfaces in Model A results. The timescales for the rise of buoyant fingers also differ between Models A and B. For example, the time to obtain freshwater fingers of a roughly similar height differs substantially, as evident in the timing of 292.3 days for Figure 4.4c (Model A) and 2191.9 days for Figure 4.4g (Model B). Thus, the lower aquitard in Model B significantly restricts finger speeds, which is an intuitive outcome. HBF in Model A for the Base Case, Case 1 and Case 2 reaches elevations of 119.15 m, 110.95 m and 110.75 m in Figures 4.3c, 4.4c, and 4.5c, respectively. These represent average finger speeds of 48.9 m/year, 38.7 m/year, and 38.4 m/year. Lower velocities are produced in all three cases of Model B. That is, HBF heights were 129.85 m, 127.15 m and 120.95 m in Figures 4.3g, 4.4g and 4.5g, leading to velocities of 8.31 m/year, 7.86 m/year and 6.82 m/year, respectively. There is evidence of boundary effects in Model A, associated with the vertical no-flow boundaries, that was also observed by Xie et al. (2011). Greater velocities of fingers adjacent to no-flow boundaries are attributed to the absence of the host fluid (i.e. seawater) moving in the opposite direction to the buoyant fingers, which is otherwise expected to retard the finger upwelling speed. For that reason, fingers adjacent to vertical boundaries were neglected in assessing HBF speeds.

According to Xie et al. (2011), the theoretical velocity of fingers is 13.1 m/year, based on  $(\Delta\rho K/\rho_f \varepsilon) \times f$ , where  $f$  (0.115) is the Xie et al. (2011) corrective factor to the theoretical convective velocity (i.e., the ratio between equation (4.7) and  $\varepsilon$ ). Interestingly, the Xie et al. (2011) corrected convective velocity, which neglects the leaky layer in Model B, is closer to the results in Model B (i.e., 8.31 m/year, 7.86 m/year and 6.82 m/year), compared to the finger velocities in Model A (i.e., 48.9 m/year, 38.7 m/year, and 38.4 m/year). However, finger velocities in Model A could be better predicted applying values of  $f$  that fall within the range

of corrective factors proposed by Post and Kooi (2003) and Wooding (1969) (i.e., 0.22 and 0.446, respectively).

Figure 4.6 illustrates the temporal variability in total solute mass within model domains, for the six scenarios considered in this study. The fluctuations in total mass in Model B are caused by mixed-convective instabilities, which persist as quasi-steady state conditions, as discussed above. The time for Model A to reach steady-state conditions (approximately 2 years) is much less than the time required for Model B to reach quasi-steady state conditions (approximately 10 years). This is consistent with the difference between buoyant fingering speeds found in Models A and B, as discussed above. The larger velocities in Model A (e.g., 48.9 m/year, 38.7 m/year, and 38.4 m/d in Figures 4.3c, 4.4c, and 4.5c) led shorter timescales to reach steady state compared to Model B, in which velocities were 8.31 m/year, 7.86 m/year and 6.82 m/year (Figures 4.3g, 4.4g and 4.5g).

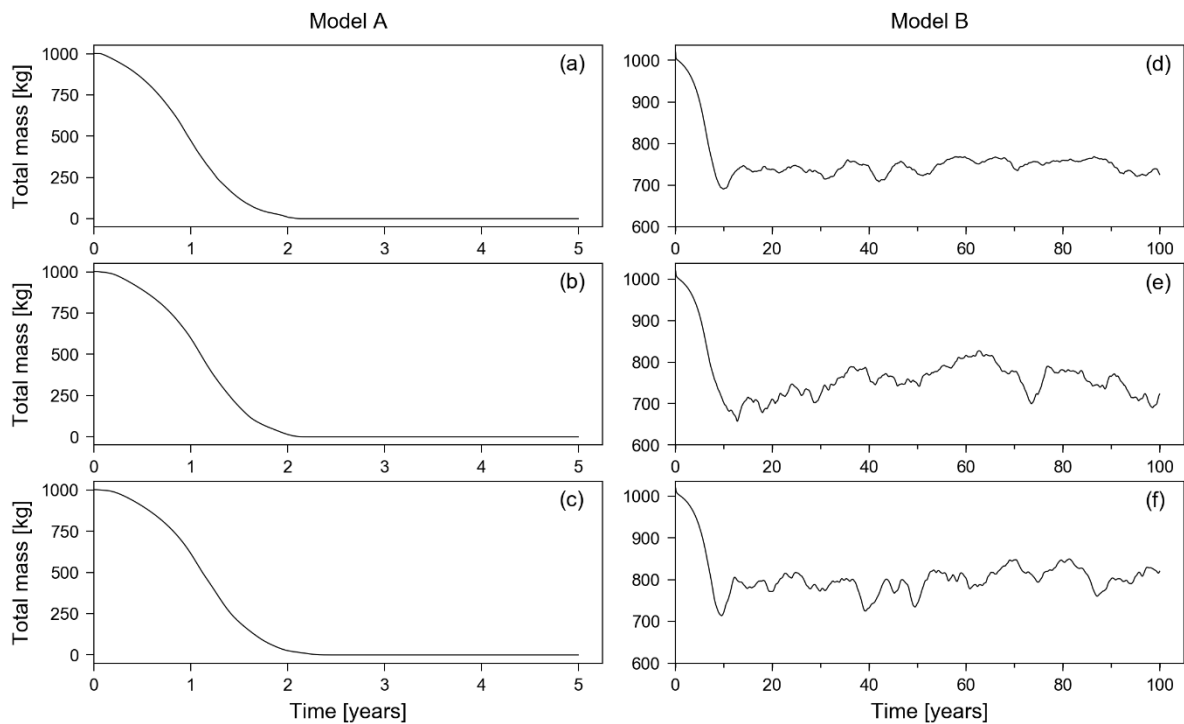


**Figure 4.6** Numerical model results of total solute mass with time. (a) and (d) Base Case (i.e.,  $\alpha_L = 0.1$  m;  $\alpha_T = 0.01$  m); (b) and (e) Case 1 (i.e.,  $\alpha_L = 0.5$  m;  $\alpha_T = 0.05$  m); and (c) and (f) Case 2 (i.e.,  $\alpha_L = 1$  m;  $\alpha_T = 0.1$  m). The left column represents cases of Model A and the right column represents cases of Model B.

#### **4.6.2 The influence of dispersion**

Figure 4.6 shows that variations in dispersion had no noticeable impact on the time required to reach steady and quasi-steady state conditions. This is consistent with the relatively small change between cases (i.e., from Base Case to Case 2) in buoyant fingering speeds, as observed also by Xie et al. (2011). The little influence of dispersion on buoyant fingering speeds is also in accordance with the definition of the theoretical convective velocity proposed by Xie et al. (2011), which neglects dispersion. While dispersion has an unimportant role in the speed of buoyant finger rise, dispersion does appear to influence the quasi-steady state buoyant fingering patterns associated with mixed-convective processes (Figures 4.3 to 4.5).

Figure 4.7 compares the three cases (i.e., Base Case, Case 1 and Case 2) of Model B, showing quasi-steady state salinity distributions in profile, and the temporal variation in SFGD solute concentration at the seafloor using a timeframe of 85 years. Subplots 7a, 7b and 7c correspond to Figures 4.3h, 4.4h and 4.5h, respectively.

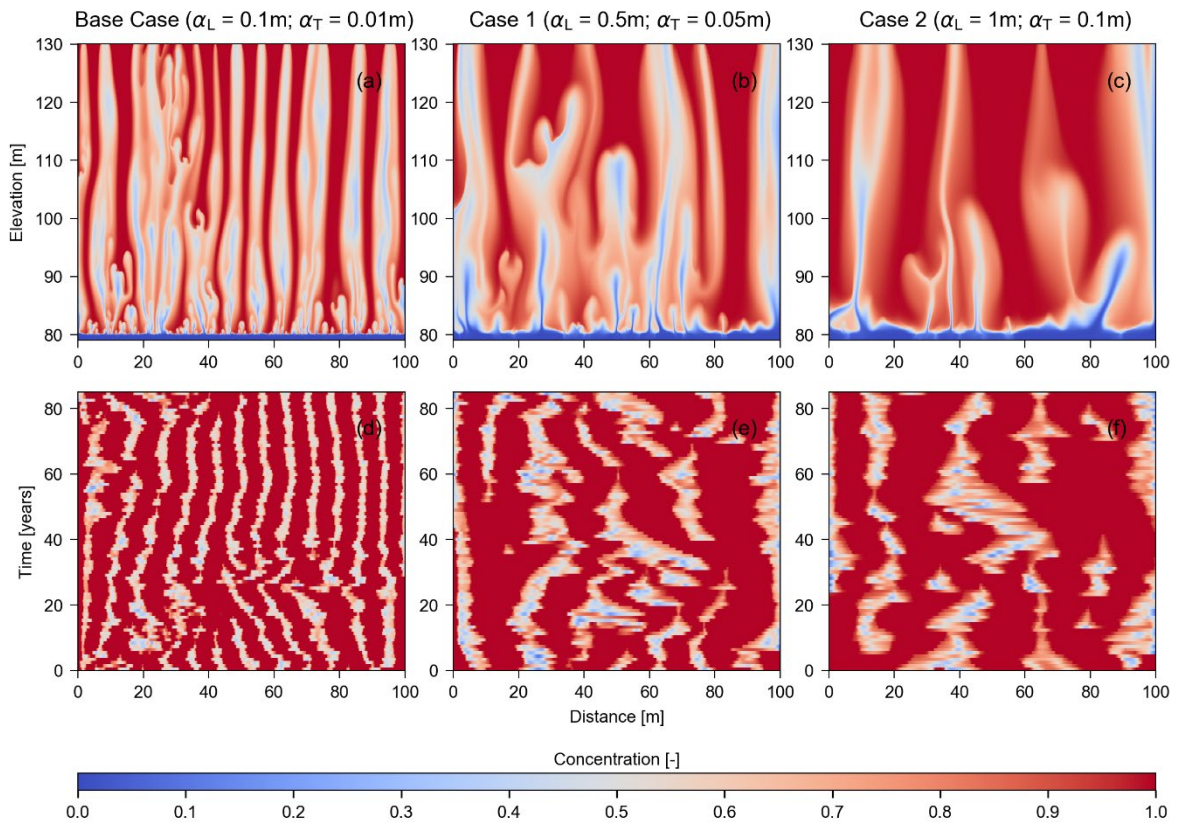


**Figure 4.7** Salinity distribution in profile (subplots (a) to (c); top row) and temporal variation of solute concentration (subplots (d) to (f); bottom row) in seafloor sediments obtained from Model B simulations: Subplots are (from left to right) the Base Case, Case 1 and Case 2. Concentration values represent the relative seawater concentration, where 0 and 1 are freshwater and seawater, respectively. All subplots show a quasi-steady state salinity distribution.

Figure 4.7 shows that the number of fingers reaching the seafloor decreases with increasing dispersion due to the widening of fingers; a similar observation to those of Xie et al. (2011) for dense, downward-moving fingers.

The temporal and spatial variability in the salinity distribution across the sea floor have important implications for the direct measurement of SFGD. For example, the deployment and size of seepage meters (e.g., Burnett et al., 2006) in areas where mixed-convective processes occur require consideration of the spatial variability in freshwater discharge, given the irregular distributions of SFGD in Figures 4.3 to 4.7. Mixed-convective flow leads to regions of freshwater upwelling and seawater downwelling, and therefore, SFGD measurement methods that can detect seafloor fluxes in both directions (inflow and outflow) may assist in detecting

mixed-convective phenomena. Additionally, the duration of seepage meter placement should consider the temporal variation of SFGD created by mixed convective processes. Freshwater upwelling appeared to be relatively stable over durations of days-to-weeks, but may vary substantially over longer timeframes, at least for the cases illustrated in Figure 4.7.

The non-dimensional parameters  $Ra$  and  $M$  were determined, using equations (4.1) and (4.5), respectively, from the quasi-steady state results of Model B. The steady-state solution of Model A has no density gradients within the aquifer (i.e., the aquifer is freshwater-filled), and therefore, both  $Ra$  and  $M$  (and  $Ra\delta$ ) are zero. Given that the system is forced-convection dominated, SFGD to the seafloor under the Model A conditions will be diffusive or uniformly distributed.

For the application of equation (4.5) to estimate  $M$  for Model B, an average  $q_z$  (across the bottom aquifer) over about 85 years of quasi-steady state conditions was used, based on the numerical results. The need to know  $q_z$  in applying equation (4.5) to estimate  $M$  (or  $Ra\delta$ ), as a predictor of buoyancy-driven flow, is potentially problematic for the purposes of designing SFGD monitoring systems (e.g., deployment of seepage meters), because rates of SFGD are typically not known prior to seepage meter deployment. For example, Stevens et al. (2009) estimated  $M$  by applying equation (4.4), which requires the vertical hydraulic gradient (based on localized measurements of hydraulic heads and salinities from bore data) rather than  $q_z$ . Nevertheless, where mixed convective processes occur in seafloor sediments, the vertical hydraulic gradient is also difficult to ascertain considering the changes in location and temporal variations of SFGD caused by buoyancy forces. Alternative approaches to estimating  $q_z$ , such as the application of geochemical tracers (e.g., Taniguchi et al., 2019), may overcome difficulties in measuring hydrogeological variables within seafloor sediments.

The steady-state value of  $q_z$  is  $2.9 \times 10^{-3}$  m/d in the Base Case (Figure 4.7a),  $2.9 \times 10^{-3}$  m/d in Case 1 (Figure 4.7b), and  $2.3 \times 10^{-3}$  m/d in Case 2 (Figure 4.7c). These values are within the range of values of  $q_z$  (i.e.,  $4.6 \times 10^{-6}$  m/d –  $3.1 \times 10^{-3}$  m/d) inferred from data reported by Knight et al. (2018), assuming uniformly distributed discharge along the aquitard. While the values of  $M$  for the three cases of Model B vary within the same order of magnitude (i.e., 22 to 27), the range of values of  $Ra$  is wider (i.e., 2031, 431 and 264 for the Base Case, Case1 and Case 2,

respectively). These values indicate that the flow system in Model B is free-convection dominated. That is,  $M > 1$ , and the critical values of  $Ra_\delta$  (or  $M$ ) and  $Ra$  (i.e., 10 and 5, respectively) are also exceeded, indicating that unstable solute motion is likely to occur. Therefore, the occurrence of unstable flow in the current cases are consistent with critical values proposed in the literature for downwards salinization (e.g., Wooding et al., 1997; Smith and Turner, 2001). However, further investigation is warranted to ascertain if those critical values can be generally applied to SFGD through sandy seafloor sediments.

## 4.7 Conclusions

This research highlights that the occurrence of SFGD in permeable seafloor sediments potentially involves unstable flow processes, with important implications for SFGD measurement and the understanding of seafloor ecosystems. This study provides insight into SFGD measurement approaches, since we have demonstrated that for the cases considered here, SFGD measurements through the deployment of seepage meters will depend on the placement and measurement duration of seepage meters. Predicting whether unstable flow processes occur is theoretically plausible based on our overview of the most common non-dimensional numbers (i.e.,  $Ra_\delta$ ,  $Ra$ , and  $M$ ) used previously to characterize mixed-convection processes in groundwater. Simplified numerical models that represent submarine aquifers settings show that SFGD can occur in the form of upward freshwater fingers, analogous to the inverse downward movement of dense solute fingers. We found that the critical values of  $Ra_\delta$  and  $Ra$  proposed in the literature for solute convection apply to the two cases analyzed in this study, although, further investigation is needed to generalize the use of those critical values to SFGD through sandy seafloor sediments. That is, further research into SFGD through high-permeability sediments is warranted to constrain the application of non-dimensional numbers for predicting unstable conditions, given the substantial differences between stable and unstable salinity patterns and distributions of SFGD to the seafloor. The results of this study show that the pattern of SFGD through high-permeability sediments containing seawater is controlled by the lower boundary, intended to represent either an underlying aquifer or aquitard. The numerical results also showed quasi-steady temporal fluctuations in the SFGD pattern behavior, for the case involving a low-permeability layer beneath the seafloor aquifer.

## Chapter 5

### **Applicability of analytical solutions to tidal propagation in circular islands**

Accepted for publication in *Journal of Hydrology*: Solórzano-Rivas, S. C., Werner, A. D. Applicability of analytical solutions to tidal propagation in circular islands. *Journal of Hydrology*, 589. doi:10.1016/j.jhydrol.2020.125136.

*Approximate contribution of co-authors: S.C. Solórzano-Rivas (75%); Adrian Werner (25%).*

#### **5.1 Abstract**

The propagation of tides into coastal aquifers is an important phenomenon in the migration of coastal contaminants, for the representation of shoreline boundary conditions in regional-scale groundwater models, and for the estimation of aquifer properties based on tidal amplitude attenuation and/or phase increase. In this study, an analytical solution to the propagation of tidal fluctuations in a radial flow field, applicable to circular islands, is compared to the existing straight-coastline (“Ferris”) solution. The analytical solution is compared to numerical simulation (using SEAWAT) of a simple-harmonic ocean tide and its propagation within a circular island. This represents the first attempt to combine a previous correction that allows SEAWAT to simulate axisymmetric flow and a modification to SEAWAT to create tidal boundary conditions. Bench testing the analytical solution against the numerical model confirms the numerical approach. The circular-island solution is compared to the Ferris solution in terms of tidal amplitude decay and phase shift. Whereas amplitude decay from the Ferris solution is valid only for near-shore locations within circular islands, the Ferris solution produces reasonable phase lag estimates for typical aquifer diffusivities and for most locations within circular islands. By comparing the Ferris and circular island solutions, we propose a correction factor to the Ferris solution that allows it to be applied in circular boundary settings. This extends the application of the widely applied Ferris solution to a broader range of situations.

## 5.2 Introduction

Tidal propagation in coastal aquifers has been shown to be an important phenomenon in studies of coastal contaminant transport and seawater intrusion, and for the field estimation of aquifer diffusivity (e.g., Ferris, 1951; Werner and Lockington, 2006; Pool et al., 2014). The development of methodologies to predict the transmission of tides in coastal aquifers has been the subject of significant research attention (e.g., Jacob, 1950; Ferris, 1951; Jiao and Tang, 1999; Li and Jiao, 2001; Chuang and Yeh, 2007; Guo et al., 2010). Consequently, several analytical solutions to groundwater tidal propagation have been devised.

Ferris (1951) provided the most popular analytical solution for estimating the characteristics (amplitude and phase) of groundwater oscillations caused by ocean tides. The analytical solution (hereafter termed the “Ferris solution”) is based on the analogous work of Ingersoll et al. (1948) for the conduction of heat in solids, and that of Jacob (1950), who was the first to present an analytical solution to groundwater fluctuations in response to a tidal force. It applies to aquifers with hydraulic diffusivity,  $\alpha$  [ $L^2 T^{-1}$ ], that is constant in space and time (i.e., homogeneous, confined-aquifer conditions), and vertical, straight, infinitely long coastlines. Hydraulic diffusivity is the ratio between transmissivity,  $T$  [ $L^2 T^{-1}$ ], and storativity,  $S$  [-] (e.g., Merritt, 2004), or hydraulic conductivity,  $K$  [ $L T^{-1}$ ], and specific storage,  $S_s$  [ $L^{-1}$ ] (e.g., Depner and Rasmussen, 2016). The Ferris solution has been applied to islands with somewhat orbiculate, rounded, curvilinear or irregular shorelines (e.g., Banerjee and Sarwade, 2008; Rotzoll and El-Kadi, 2008; Chattopadhyay et al., 2014.). However, it is currently unclear whether the curvature of these islands invalidates the use of the Ferris solution.

An analytical solution to tidal propagation in circular islands is an important tool to estimate aquifer properties. The remoteness and strong influence of tides on many small islands often hampers the determination of their aquifer properties using standard methods, such as pump tests. Williams et al. (1970) presented the first attempt to assess the effect of tidal propagation within circular islands in their technical report on tidal effects in Hawaii. They studied the influence of tides on groundwater flow through analytical, physical (i.e., polyurethane foam tank) and electric analogue models. The conceptual models of Williams et al. (1970) include straight coastlines, consistent with the Ferris solution, and circular boundaries. Physical and

electrical analogue models were used to evaluate the straight-coastline analytical solutions. Townley (1995) also presented a set of analytical solutions for periodic aquifer flow including circular boundaries. Trefry (1999) applied Townley's (1995) methodology to extend it to aquifers of composite structure.

The objective of this work is to describe an analytical solution for the response of groundwater hydraulic heads to oceanic tidal fluctuation in aquifers with circular boundaries – i.e., circular islands. Although the solution presented here is an existing solution; the evaluation of the Ferris solution to curved coastlines was not assessed in previous studies (i.e., Williams et al., 1970; Townley, 1995). Likewise, the same underlying assumptions (i.e., homogenous, isotropic, confined aquifer) that apply to the Ferris solution are adopted. The analytical solution for circular boundaries is analogous to heat conduction theory developed by Carslaw and Jaeger (1959), which provides the basis for the mathematical development of the current solution. We compare the analytical solution to a numerical solution using a modified version of SEAWAT (Post, 2011). The numerical model adopts Langevin's (2008) radial adaptation to SEAWAT parameters, thereby leading to the first published attempt to simulate tidal propagation in circular islands combining the Langevin (2008) approach to radial flow simulation and the modified version of SEAWAT (Post, 2011) that provides for a tidal boundary condition. The present study aims to provide guidance on the application of straight boundary-based analytical solutions to tidal propagation where shorelines are circular by exploring the accuracy of the Ferris solution when applied to curved coastlines.

### **5.3 Conceptual model**

Figure 5.1 shows a cross section (in radial coordinates) through a homogeneous, circular island that is confined and of uniform geometry. The same conceptual model was used by Ferris (1951), except Cartesian rather than radial coordinates are adopted. The cross-section length is the radius of the island ( $a$ ), and axisymmetric flow is assumed. Figure 5.1 is bounded to the left and right by the centre of the island and the ocean, respectively. The seaward boundary is defined by a simple harmonic tidal signal, and water density variations are neglected. Numerically, the centre of the island is defined by a no horizontal flow boundary condition.

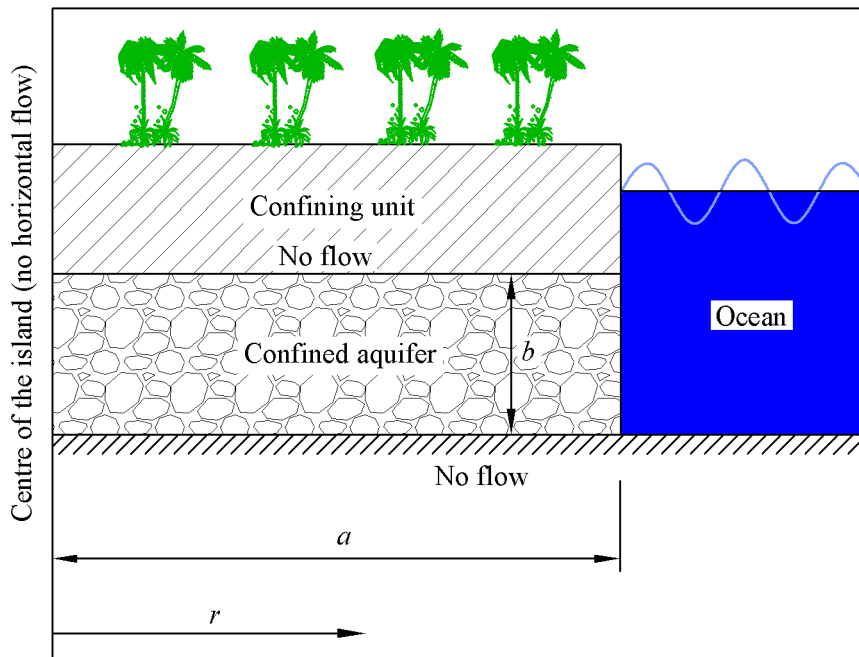


**Figure 5.1** Conceptual model of a circular island subjected to tidal forcing at the shoreline, where  $b$  is the aquifer thickness,  $r$  is the radial distance from the centre of the island, and  $a$  is the island radius.

Despite the fact that island aquifers are generally unconfined with shallow watertables (e.g., Werner et al., 2017), confined aquifer conditions are often presumed for the sake of mathematical tractability (e.g., Bear, 1979, p. 115). That is, the groundwater flow equation for a phreatic aquifer (i.e., the Boussinesq equation) is linearized by adopting the Dupuit approximation and assuming a constant average  $T$  (i.e., first method of linearization of Bear, 1979, p. 115), which is reasonable where watertable fluctuations are small relative to the saturated thickness from the base of the aquifer (e.g., Ferris, 1951). Thus, the Ferris solution may be applied to unconfined aquifers for relatively small tidal amplitudes. Erskine (1991) supported the use of Ferris (1951) in a coastal unconfined aquifer in the UK, where the groundwater tides observed at different distances from the shoreline appeared to follow the same trends that are described by the Ferris solution. Serrano and Workman (1998) explored the difference between adopting the linearized and nonlinear Boussinesq equation for an unconfined aquifer subject to the tidal influence of a river. They compared results to observed groundwater heads and found that both approaches provided similar results except when the

ratio of the amplitude of the river tide to the average aquifer thickness was higher than about 0.16, for which the nonlinear Boussinesq equation better represented head changes.

## 5.4 Circular-island solution

Here, we develop the circular-island analytical solution (i.e., Williams, 1970; Townley, 1995) to seek functional relationships between the circular and Ferris solutions. Following the assumption of small tidal amplitudes, the circular-island solution is found by solving the one-dimensional, axisymmetric groundwater flow equation in radial coordinates (e.g., Bear, 1979, p. 116):

$$\frac{\partial^2 h}{\partial r^2} + \frac{1}{r} \frac{\partial h}{\partial r} = \frac{S}{T} \frac{\partial h}{\partial t} \quad (5.1)$$

Here,  $h$  is the groundwater hydraulic head [L],  $t$  is time [T],  $S$  is storativity and  $T$  is transmissivity [ $L^2 T^{-1}$ ]. Tidal conditions of constant amplitude and period are adopted as boundary conditions, given by:

$$h|_{r=a} = A_0 \sin(\omega t) \quad (5.2)$$

where  $A_0$  is the constant tide amplitude [L] at the shoreline, and  $\omega$  is the angular frequency [rad  $T^{-1}$ ].

By setting (e.g., Carslaw and Jaeger, 1959, p. 193):

$$h = \Im\{\Theta(r)e^{i\omega t}\} \quad (5.3)$$

where  $\Theta$  is a complex function and  $\Im$  indicates the imaginary part of it. Equation (5.1) can be expressed as:

$$\frac{\partial^2 \Theta}{\partial r^2} + \frac{1}{r} \frac{\partial \Theta}{\partial r} - i\beta^2 \Theta = 0 \quad (5.4)$$

where  $\beta = \sqrt{\omega S/T}$ . Equation (5.4) is solved with the boundary condition of  $\Theta = A_0$  at  $r = a$  (see Figure 5.1). At the centre of the island the value of  $\Theta$  is finite (e.g., Carslaw and Jaeger, 1959,

p. 327). According to Townley (1995), this solution leads to a no-flow condition at the island centre. The solution to (5.4), is provided for heat conduction in solids by Carslaw and Jaeger (1959, p. 328) using the Laplace transformation method:

$$\Theta = \frac{I_0(\gamma r)}{I_0(\gamma a)} A_0 \quad (5.5)$$

where  $I_0$  is a Modified Bessel function of the first kind of order zero (e.g., Abramowitz and Stegun, 1965, p. 374), and  $\gamma = \beta\sqrt{i}$ . Townley (1995) also solved equation (5.4) in terms of Modified Bessel functions, whereas Williams et al. (1970) in terms of Kelvin functions (e.g., Abramowitz and Stegun, 1965, p. 379). However, both expressions are equivalent. The derivation provided in this article arrives at a solution of the same form as that given by Townley (1995).

By combining equations (5.3) and (5.5), head fluctuations are given (in radial coordinates) as (e.g., Bruggeman, 1999, p. 204):

$$h = \Im \left\{ \frac{I_0(\gamma r)}{I_0(\gamma a)} A_0 e^{i\omega t} \right\} \quad (5.6)$$

Applying Euler's formula (e.g.,  $e^{i\omega t} = \cos\omega t + i\sin\omega t$ ), trigonometric functions and the complex solution of equation (5.5), equation (5.6) can be rearranged for the imaginary part only, as:

$$h = A_0 \sqrt{c^2 + d^2} \sin(\omega t - \varphi) \quad (5.7)$$

where:

$$c = \Re \left\{ \frac{I_0(\gamma r)}{I_0(\gamma a)} \right\} \quad (5.8)$$

$$d = \Im \left\{ \frac{I_0(\gamma r)}{I_0(\gamma a)} \right\} \quad (5.9)$$

$$\varphi = \tan^{-1}(-d/c) \quad (5.10)$$

Here,  $\Re$  indicates the real part of the complex solution,  $\varphi$  is the phase lag [rad] relative to the ocean tide. The lag of groundwater tides in time units is given by  $t_{\text{lag}} = \varphi/\omega$  [T].

It follows from equation (5.7) that decay in the amplitude of groundwater head fluctuations ( $A_g$ ) with distance from the shoreline of a circular island is given by:

$$A_g = A_0 \sqrt{c^2 + d^2} \quad (5.11)$$

The  $A_g/A_0$  ratio is commonly known as tidal efficiency (e.g., Carr and van der Kamp, 1969).

## 5.5 Numerical model

Numerical comparison of the circular-island analytical solution is undertaken using SEAWAT, modified by Post (2011) to allow tidal boundary conditions (i.e., the PBC package) to be simulated. Mulligan et al. (2011) and Post (2011) demonstrated the effectiveness of the PBC package to simulate tidal boundary conditions. Other studies have also adopted this approach (e.g., Heiss and Michael, 2017; Trglavcnik et al., 2017). Post (2011) used the following equation to define the tidal boundary head (simplified to a single tidal constituent and without the complications that are introduced by seepage face development):

$$h = h_0 + A_0 \cos(\omega t - \varphi_0) \quad (5.12)$$

Here,  $h_0$  is a reference tidal stage [L] and  $\varphi_0$  is the phase lag at the boundary [rad]. To make equation (5.12) equivalent to the analytical solution (equation (5.7)),  $h_0 = 0$  and  $\varphi_0 = \pi/2$ .

The comparison between numerical and analytical solutions was undertaken for a hypothetical island of  $a = 500$  m, with top and bottom aquifer elevations of 10 m and 60 m below sea level, respectively. The selection of the model dimensions was subjected to computation times. The horizontal discretization was  $\Delta x = 0.1$  m (i.e., 5001 columns). Given the underlying assumption of one-dimensional flow adopted by the circular-island solution, the numerical model layout comprises only one layer. The simulation was run for 100 days using 20,000 time steps of

constant duration. The methodology described by Langevin (2008) was applied to adjust the input parameters of SEAWAT to represent radial flow coordinates. This involves multiplying hydraulic conductivity ( $K$ ) and the storage coefficient ( $S$ ) by  $2\pi r$ . The hydraulic parameters, before adjustment to radial coordinates, are:

- $K = 200$  m/d (value within the range of the Holocene sediments in atoll islands, e.g., Werner et al., 2017); leading to  $T = 10,000$  m<sup>2</sup>/d.
- $S = 0.1$  (value within the range for unconfined aquifers, e.g., Lohman, 1972).
- $\alpha = T/S = 100,000$  m<sup>2</sup>/d.

The ocean tide was defined by  $A_0 = 0.9$  m and  $\omega = 4\pi$  rad/day (i.e., period = 12 hours).

Three locations from the shoreline were selected for comparison between analytical and numerical approaches. The root-mean-square error (RMSE) was used as a measure of goodness-of-fit of heads. The RMSE for heads is given by  $\left[\frac{1}{n}\sum_{j=1}^n (h_{nj} - h_{aj})^2\right]^{1/2}$ , where  $h_{nj}$  and  $h_{aj}$  are heads at time step  $j$  from the numerical and analytical solutions, respectively, and  $n$  is the number of time steps used for the comparison. The period of comparison was 90 to 91 days, at which time the amplitude and phase had stabilised (i.e., “dynamic equilibrium” conditions were reached). Harmonic analysis was used to estimate numerical values of  $A_g$  and  $\varphi$ , based on a least-squares approach (e.g., Bloomfield, 1976). The absolute errors of the amplitude  $|A_{gn} - A_g|$  and phase  $|\varphi_n - \varphi|$  were used to assess differences between numerical and analytical results, where  $A_{gn}$  and  $\varphi_n$  are respectively the amplitude and phase from the numerical solution.

## 5.6 The Ferris solution versus the circular-island solution

Ferris (1951) proposed that for an infinitely straight coastline, the solution to groundwater fluctuations due to tidal effects in a homogenous, isotropic aquifer is:

$$h_F = A_0 e^{-\beta(a-r)/\sqrt{2}} \sin\left(\omega t - \frac{\beta(a-r)}{\sqrt{2}}\right) \quad (5.13)$$

where the term  $(a - r)$  represents the distance from the shoreline. This solution presumes that the phase lag at the shoreline is zero. Hereafter, the subscript “F” identifies variables obtained from the Ferris solution. From equation (5.13), amplitude decay is described by Ferris (1951) as:

$$A_{gF} = A_0 e^{-\beta(a-r)/\sqrt{2}} \quad (5.14)$$

And the expression for  $\varphi_F$  within the argument of equation (5.13) is (Ferris, 1951):

$$\varphi_F = \varphi_0 + \beta(a - r)/\sqrt{2} \quad (5.15)$$

Comparing equations (5.14) and (5.15), it is clear that the two variables  $A_{gF}$  and  $\varphi_F$  are exponentially related. Conversely, in the case of the circular-island solution (i.e., equations (5.10) and (5.11)), the relationship between  $A_g$  and  $\varphi$  is more complex. The applicability of the Ferris solution to circular boundaries is assessed by comparing the ratios  $A_{gF}/A_g$  and  $\varphi_F/\varphi$ .

The comparison between the Ferris and circular-island solutions was undertaken for a hypothetical island of  $a = 500$  m. The total simulation time was 100 days subdivided into 10,000 uniform time steps (contrary to the analysis in the previous section, where 20,000 time steps were used). Four alternative values of  $\alpha$  were tested, namely 250 m<sup>2</sup>/d, 2500 m<sup>2</sup>/d, 30,000 m<sup>2</sup>/d and 100,000 m<sup>2</sup>/d, according to average values from published case studies, e.g., Garden Island (Australia; Trefry and Bekele, 2004) and Gran Canaria (Spain; Cabrera and Custodio, 2004). To explore the role of island size (radius) in controlling the tidal effect, the Ferris and circular-island solutions were compared for radii between 50 and 2000 m.

## 5.7 Results and discussion

### 5.7.1 Comparison of the numerical solution and circular-island analytical solution

Figure 5.2 shows the comparison between numerically and analytically derived groundwater tides. Figure 5.2a presents the temporal hydraulic head variations at three locations within an

island of radius  $a = 500$  m (other input parameters are given in Section 5.5). Figure 5.2b shows the variation (with distance) in  $A_g/A_0$ ,  $A_{gn}/A_0$  and the absolute difference between  $A_{gn}$  and  $A_g$ , while Figure 5.2c shows variation (with distance) in  $\varphi_n$ ,  $\varphi$ , and the absolute difference between  $\varphi_n$  and  $\varphi$ .

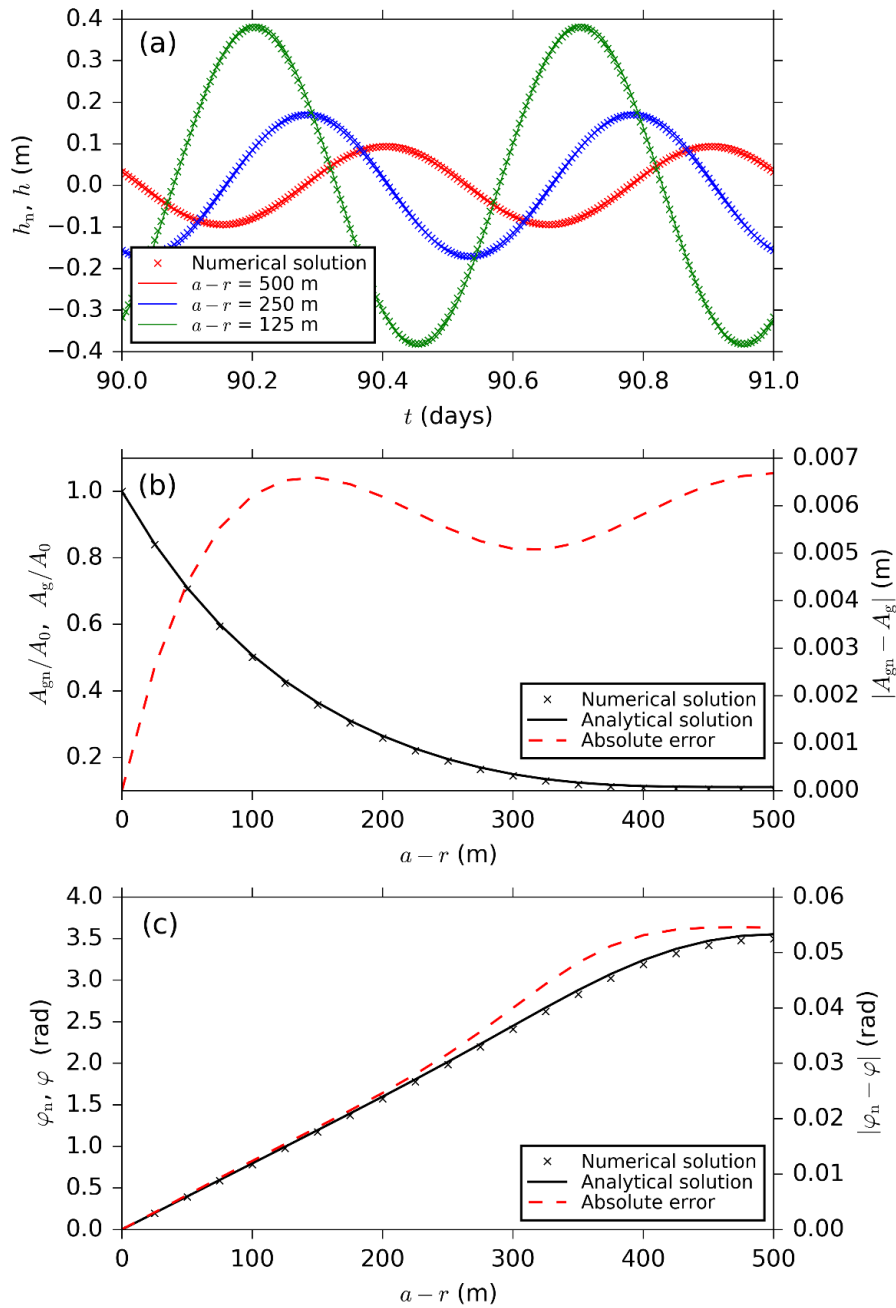


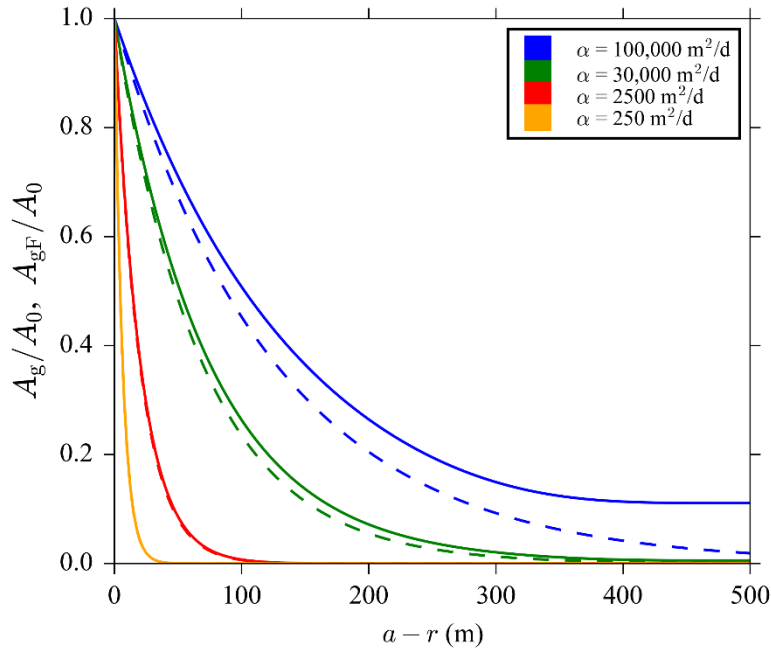
**Figure 5.2** Results for the propagation of groundwater tides within a circular island of radius  $a = 500$  m showing the match between the circular-island analytical solution (solid lines) and numerical modelling (symbols). Comparisons are given for: (a) hydraulic head oscillations at three locations, (b) tidal efficiency variation with  $r$ , and (c) phase variation with  $r$ . Red dashed

lines in (b) and (c) represent the absolute differences in amplitude ( $|A_{gn} - A_g|$ ) and phase ( $|\varphi_n - \varphi|$ ), respectively. Note that  $a - r = 0$  represents the shoreline and  $r = 0$  represents the island centre. The subscript “n” indicates the numerical solution results.

There is excellent agreement between dynamic equilibrium-state groundwater fluctuations obtained with the circular-island analytical solution and the numerical solution (Figure 5.2a), as indicated by RMSE values at the three locations of: 0.0057 m ( $a - r = 500$  m), 0.0052 ( $a - r = 250$  m) and 0.0059 m ( $a - r = 125$  m). The non-linear trend in the RMSE values with distance is consistent with the non-linear trends in the absolute differences (analytical versus numerical) in tidal efficiency and phase (i.e., Figures 5.2b and 5.2c). Given that absolute errors are small (e.g., maximum  $|A_{gn} - A_g| = 6.7 \times 10^{-3}$  m and the maximum  $|\varphi_n - \varphi| = 5.5 \times 10^{-2}$  rad), the numerical model applying the Langevin (2018) methodology to represent radial flow coordinates, and the Post (2011) SEAWAT package to simulate periodic boundary conditions, is bench tested.

### 5.7.2 Comparison of the Ferris and circular-island analytical solutions

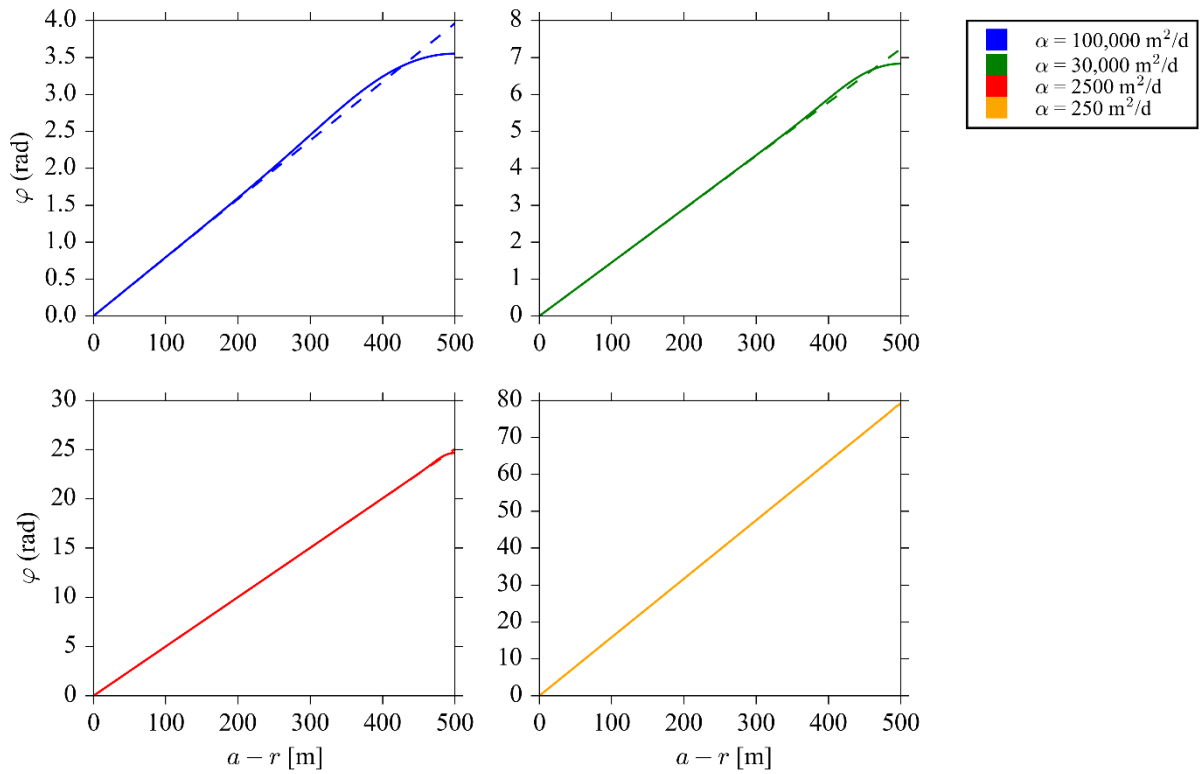
The Ferris and circular-island solutions are compared in Figure 5.3, which shows  $A_g/A_0$  and  $A_{gF}/A_0$  with distance, for four different  $\alpha$  values but otherwise the same hypothetical example used in the previous subsection (i.e.,  $a = 500$  m).



**Figure 5.3** Comparison of Ferris (dashed lines) and circular-island (solid lines) solutions in terms of the tidal efficiency with distance from the island coastline. Results are given for an island of size  $a = 500$  m and considering four different  $\alpha$  values. Note that  $a - r = 0$  represents the shoreline and  $a - r = 500$  represents the island centre.

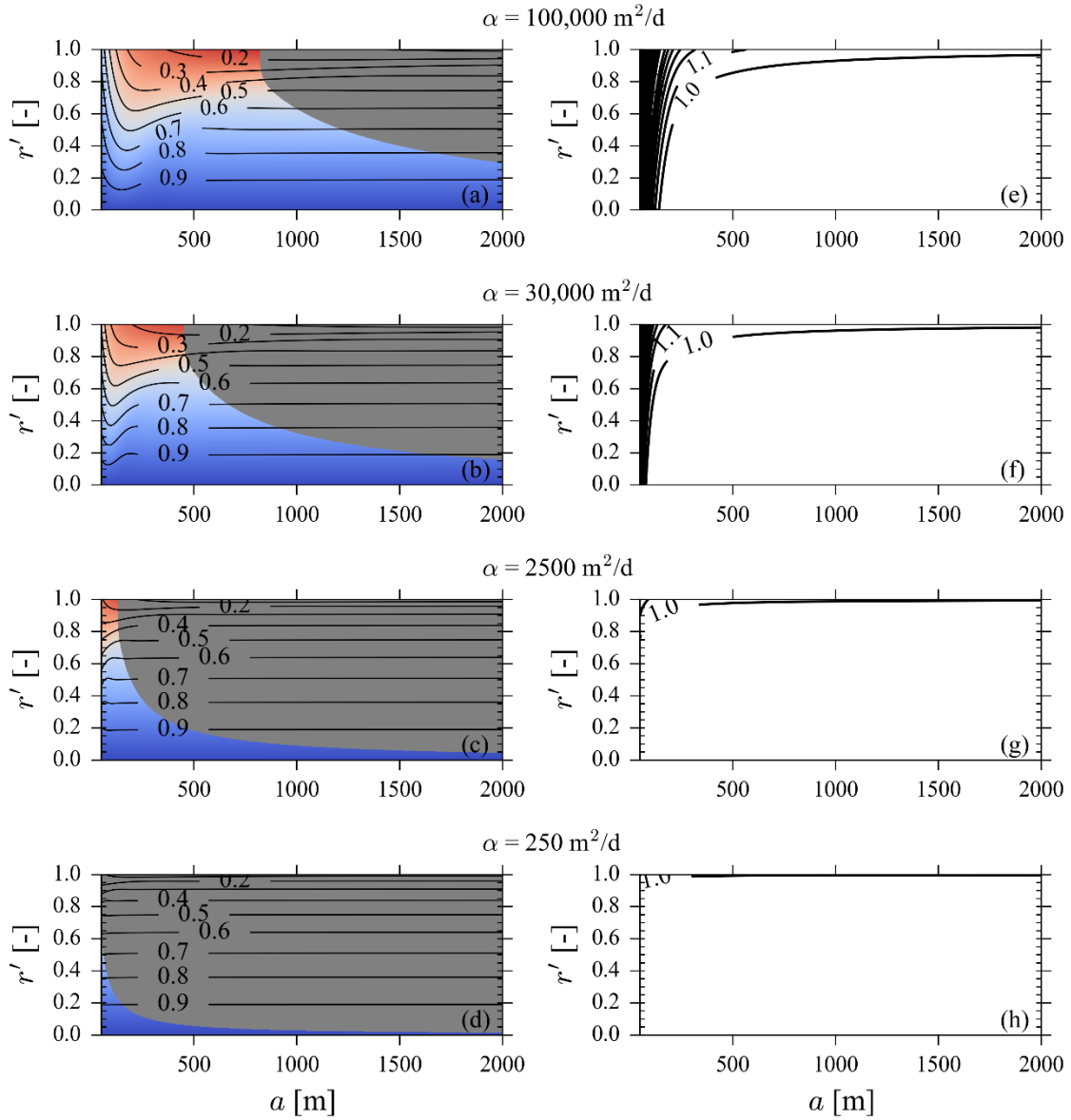
Figure 5.3 shows that tides propagate greater distances from the shoreline with increasing  $\alpha$  (for both Ferris and circular-island solutions), as expected. The Ferris solution underestimates the tidal propagation when applied to the circular island setting, as evident from amplitudes that are lower than those from the circular-island solution. The underestimation is greater for higher values of  $\alpha$ .

Figure 5.4 compares Ferris and circular-island solutions in terms of  $\varphi$ , showing the spatial trends for four  $\alpha$  values, again for an island of  $a = 500$  m. The phase lag reduces as  $\alpha$  increases, as expected (Ferris, 1951). The phase lag reduction is almost linear with distance from the shoreline in both the Ferris and circular-island solutions. The close match in  $\varphi$  obtained using the Ferris and circular-island solutions (Figure 5.4) is surprising given that amplitude decay differs between the two solutions (Figure 5.3). For higher  $\alpha$  values (i.e.,  $\alpha = 30,000$  m<sup>2</sup>/d and 100,000 m<sup>2</sup>/d), the circular-island solution departs from the Ferris solution in a nonlinear fashion such that  $\varphi$  tends to be overestimated by the Ferris solution at distances close to the island centre.



**Figure 5.4** Comparison of  $\varphi$  estimated with the Ferris (dashed lines) and circular-island (solid lines) solutions with distance from the shoreline for an island of  $a = 500$  m and four values of  $\alpha$ . Dashed lines are entirely obscured by solid lines in the lower plots (i.e.,  $\alpha = 250$  and  $2500$  m<sup>2</sup>/d). Note that  $a - r = 0$  represents the shoreline and  $a - r = 500$  represents the island centre.

Figure 5.5 shows spatial distributions of  $A_{gF}/A_g$  (left column) and  $\varphi_F/\varphi$  (right column) for four different  $\alpha$  for variable island radii (between 50 and 2000 m). Given the different island radii used in creating Figure 5.5, a dimensionless inland distance ( $r'$ ) is used, where  $r' = (a - r)/a$ , for which 0 represents the shoreline and 1 the centre of the island. The grey zone in the left panels of Figure 5.5 identifies the region where  $A_g$  estimated with the circular-island solution is less than or equal to 1 cm (noting that  $A_0 = 0.90$  m), which we consider below detectable limits with typical water level measurement devices (e.g., considering a pressure transducer with 10 m of measuring range and accuracy of 0.1%; In-Situ Inc., 2017).



**Figure 5.5** Spatial distribution of  $A_{gF}/A_g$  (left column; (a) to (d)) and  $\phi_F/\phi$  (right column; (e) to (h)) for island radii ( $a$ ) between 50 and 2000 m (a total of 976 island radii were used in creating Figure 5.5) for four different  $\alpha$  values.  $r' = 0$  represents the shoreline and  $r' = 1$  the centre of the island. The grey shading indicates where  $A_g \leq 1$  cm. Solid lines represent points of equal  $A_{gF}/A_g$  ratio.

Results in Figure 5.5 demonstrate that the Ferris solution, when applied to circular boundaries, underestimates  $A_g$  with distance from the shoreline, as all contours are lower than 1. Assuming an error of 10% (i.e.,  $A_{gF}/A_g \approx 0.9$ ), the Ferris solution appears to provide acceptable results for distances from the shoreline of up to  $\sim 20\%$  of  $a$ . In the grey regions of Figure 5.5, differences between the Ferris and circular-island analytical solutions are considered inconsequential

because tides are effectively immeasurable (i.e.,  $A_g \leq 1$  cm), albeit this is a function of the ocean tidal amplitude ( $A_0 = 0.9$  m in the current case). The contour patterns highlight that the circular-island and Ferris solutions have an asymptotic relationship (in terms of  $A_{gF}/A_g$ ) as  $a$  increases, as evident in contours that are effectively horizontal for higher values of  $a$ . This is somewhat surprising, because the error in using the Ferris solution to study tidal propagation in circular islands was expected to be smaller for larger islands, i.e., as the curvature of the island reduces. However, the results show that this error manifests as a virtually constant distribution in  $A_{gF}/A_g$  with relative inland distance for islands larger than about 500 m in radius (i.e.,  $a > 500$  m). Remarkably, the same  $A_{gF}/A_g$  values (i.e., as  $a$  increases for the same relative distances from the shoreline) are observed in the four panels of the left column in Figure 5.5 (i.e., see right vertical axis of 5a to 5d), implying that this ratio is independent of  $\alpha$ . This is explained by the asymptotic expansion for large arguments ( $Z$ ) of the Modified Bessel functions of the first kind of order zero (Section 5.4), for which only the first term is considered (e.g., Abramowitz and Stegun, 1965, p. 377):

$$I_0(Z) \approx \frac{e^Z}{\sqrt{2\pi Z}} \quad (5.16)$$

where  $Z$  for the circular-island solution depends on  $\omega$ ,  $S$ ,  $T$ ,  $r$ , and  $a$  (Section 5.4). Substituting equation (5.16) into equation (5.5), the values of  $c$  and  $d$  in equation (5.7) are given by the following functions:

$$c \approx \sqrt{a/r} e^{\beta(r-a)/\sqrt{2}} \cos \beta(r-a)/\sqrt{2} \quad (5.17)$$

$$d \approx \sqrt{a/r} e^{\beta(r-a)/\sqrt{2}} \sin \beta(r-a)/\sqrt{2} \quad (5.18)$$

Passing the expressions of  $c$  and  $d$  into equation (5.11) produces a function for the circular-island amplitude, for large  $Z$ :

$$A_g \approx A_0 e^{\beta(r-a)/\sqrt{2}} \sqrt{a/r} \quad (5.19)$$

Combining equations (5.19) and (5.14) produces:

$$A_{gF}/A_g \approx \sqrt{r/a} \quad (5.20)$$

This shows that for large  $Z$  values, the ratio between the Ferris and circular-island amplitudes is a simple function of the relative distances from the shoreline. Equation (5.20) also shows that  $A_{gF}/A_g$  is independent of  $\alpha$  (for large  $Z$ ). If Equation (5.20) is solved for  $A_g$ , a correction factor to the Ferris solution to be applied in circular boundaries (for large  $Z$ ) is obtained:

$$A_g \approx A_{gF}\sqrt{a/r} \quad (5.21)$$

The right column of Figure 5.5 shows that the Ferris and circular-island solutions are generally well-matched in terms of  $\varphi$  prediction, except for small islands with relatively high  $\alpha$  values. Avoiding  $\varphi$  errors of 10% in the application of the Ferris solution to circular islands requires that the island radius is greater than 90 m for  $\alpha \geq 30,000$  m<sup>2</sup>/d and the locations close to the island centre are not evaluated. The minimum  $\varphi_F/\varphi$  values for the four cases shown in the right column of Figure 5.5 (i.e., 100,000 m<sup>2</sup>/d, 30,000 m<sup>2</sup>/d, 2500 m<sup>2</sup>/d and 250 m<sup>2</sup>/d) are 0.90, 0.90, 0.93 and 0.98, respectively (these values are  $> 0.9$  and are therefore not shown by the 0.1 contour interval where the smallest contour is 1.0). These values demonstrate the good agreement in phase lag prediction between the Ferris and circular-island solutions in most situations and locations. The simplified asymptotic expansion of the zeroth-order Modified Bessel function given in equation (5.16) helps also to demonstrate the good agreement between  $\varphi_F$  and  $\varphi$ , observed in the right column of Figure 5.5. Substituting equations (5.17) and (5.18) into equation (5.10), produces a function for the circular-island phase (for large  $Z$ ):

$$\varphi = -\beta(a - r)/\sqrt{2} \quad (5.22)$$

Equation (5.22) is equivalent to equation (5.15), presuming that the phase lag at the shoreline is zero. This accounts for the excellent agreement between  $\varphi$  and  $\varphi_F$  for large  $Z$ , as depicted in the right column of Figure 5.5. The previous simplification to estimate  $A_g$  and  $\varphi$  for large arguments of the zeroth-order Modified Bessel functions has not been presented in previous literature (e.g., Williams et al., 1970; Townley, 1995).

## 5.8 Conclusions

An existing circular-island analytical solution (i.e., Williams et al., 1970; Townley, 1995) has been studied to assess the application of the Ferris solution to circular boundaries. The circular-analytical solution has been re-derived and presented using alternative functions with respect to the previous literature. The analytical solution is also compared to numerical experiments using the modified SEAWAT version that allows for periodic boundary condition (Post, 2011). This is the first study to simulate tidal propagation in circular islands where the axisymmetric correction proposed by Langevin (2008) and the modified SEAWAT version for tidal boundary conditions (Post, 2011) are combined. The results obtained in this study demonstrate an excellent agreement between analytical and numerical solutions, providing a new benchmark for numerical models simulating axisymmetric flow and applying a tidal boundary condition.

The results obtained from comparing the circular-island analytical solution and the Ferris solution lead to the following recommendations on the application of the Ferris solution to orbicular-shaped islands: (1) the Ferris solution estimates the phase lag more accurately than it estimates the amplitude decay, i.e.,  $\varphi_F/\varphi \approx 1$ ; (2) the Ferris solution can satisfactorily (i.e., within 10% error) be applied to calculate amplitude decay for distances from the shoreline of up to about 20% of the island radius; (3) the error in using the Ferris solution to study tidal propagation in circular islands does not decrease with the size of the island, as it could be expected given the reduction in the curvature of the island; (4) for island parameters that provide large  $|Z|$  (i.e.,  $|Z| \geq 2$ ; where  $Z$  is the argument of the Modified Bessel functions of the first kind of order zero), the amplitude decay can be estimated by applying a correction factor to the Ferris solution. The correction factor has been demonstrated to be a constant of proportionality between the two solutions, equal to  $\sqrt{a/r}$ . The study results show that  $|Z| \geq 2$  is associated primarily with relatively large islands (i.e.,  $a > 500$  m). It follows that for large  $a$ , the relationship between the Ferris and circular-island solutions is independent of  $\alpha$ .

The correction factor to the widely used Ferris solution, so that it applies to orbiculate-shaped islands, is an important advance in assessing aquifer properties for island settings, particularly given the advantages of tidal-based approaches over aquifer-testing methods such as pumping,

and also noting that errors of up to 60% ( $A_{gF}/A_g \approx 0.4$ ) may be incurred as the island centre is approached using the standard Ferris solution.

## Chapter 6

### Estimating hydraulic properties from tidal propagation in circular islands

Accepted for publication in *Journal of Hydrology*: Solórzano-Rivas, S. C., Werner, A. D., Irvine, D. J. Estimating hydraulic properties from tidal propagation in circular islands, 598. doi: 10.1016/j.jhydrol.2021.126182.

*Approximate contribution of co-authors: S.C. Solórzano-Rivas (75%); Adrian Werner (15%); Dylan Irvine (10%).*

#### 6.1 Abstract

Observations of tidal propagation in coastal aquifers allow for rapid, low-cost quantification of aquifer parameters that are integrated over significant distances. Previous methods for aquifer property estimation from tidal propagation have focussed on continental aquifers and assumed straight, infinite shorelines. A recent investigation has proposed a correction to the Ferris analytical solution for straight shorelines ('Ferris solution') to be applied under radial flow conditions. In this work, an existing analytical solution as a function of radial flow conditions ('circular solution') and the corrected Ferris solution are applied for the first time to obtain aquifer diffusivity in orbiculate-shaped islands. Inversion of the circular solution (to obtain diffusivity) requires iterative methods, which are applied to synthetic island aquifers with known diffusivity values ranging between 150,000 m<sup>2</sup>/d and 500,000 m<sup>2</sup>/d. The circular solution was tested for both confined and unconfined conditions and for tidal periods ranging from around 8 to 24 hours. Known aquifer diffusivity values were reproduced within 2.5% of known values, even where randomised noise was added to synthetic groundwater tidal signals, and for both confined and unconfined aquifer conditions. Application of the corrected Ferris solution was found to be reliable for both confined and unconfined conditions, with discrepancies in aquifer diffusivity < 1% and < 2.5%, respectively, including with noise added to the groundwater tidal signals. The methodology presented in this work to estimate aquifer diffusivity in orbiculate-shaped islands is an improvement over classic approaches (e.g., the Ferris solution). In particular, the radial-flow correction to the Ferris solution provides for

simple calculations of aquifer diffusivity of similar accuracy to the more complex radial analytical solution.

## **6.2 Introduction**

The knowledge of aquifer hydraulic properties is essential to understand and predict groundwater responses to hydrologic stresses. Evaluating the aquifer properties of islands is particularly important, because groundwater is often the only source of freshwater, and the vulnerability of island aquifers to degradation from anthropogenic and environmental factors is often very high (e.g., White and Falkland, 2010; Werner et al., 2017). For example, the salinization of pumping wells on islands is common because fresh groundwater typically occurs as relatively thin lenses, that float above saltwater (e.g., Werner et al., 2013). Mitigating water quality degradation on islands therefore requires effective water management based on reasonable estimates of aquifer properties.

Field-based estimates of aquifer hydraulic properties are commonly obtained by actually stressing the aquifer and observing its response in a given period of time; for example, in the form of pumping tests (e.g., Theis, 1935). Alternatively, “passive” forms of aquifer testing may be undertaken, such as the measurement of the fluctuations in coastal groundwater levels caused by ocean tides. Aquifer properties control the tidal propagation, which is manifested in aquifers as attenuation in the tidal amplitude and lag in the tidal phase, relative to the ocean tide. Extracting information about aquifer properties from tidal groundwater fluctuations was first proposed by Ferris (1951), based on earlier work by Jacob (1950). Compared to pumping tests, tidal aquifer testing requires significantly less infrastructure, and in most circumstances, provides integrated knowledge (i.e., spatially averages) of aquifer properties over larger scales than can feasibly be obtained from pumping tests.

The analytical solution (hereafter referred to as the “circular solution”) to periodic, radial flow within circular, homogeneous aquifers first appeared in the report of Williams et al. (1970) and was subsequently analysed by Townley (1995), who expressed the mathematical solution in terms of Modified Bessel functions (e.g., Abramowitz and Stegun, 1965). Williams et al. (1970) derived the solution through application of Kelvin functions (e.g., Abramowitz and Stegun,

1965). Despite the different functions used, the two solutions are equivalent. The circular solution has not been applied previously to determine aquifer properties (i.e., of islands), whereas the Ferris solution is used routinely in the estimation of aquifer hydraulic diffusivity (e.g., Jha et al., 2003; Banerjee et al., 2008; Zhou, 2008; Rotzoll et al., 2013; Chattopadhyay et al., 2014, Xun et al., 2015). Aquifer hydraulic diffusivity ( $\lambda$  [ $L^2 T^{-1}$ ]) is defined by  $\lambda = T/S$ , where  $T$  is transmissivity [ $L^2 T^{-1}$ ] and  $S$  is storativity [-]. The Ferris solution has the advantage of allowing direct calculation of  $\lambda$ , whereas the circular solution requires iterative methods to obtain  $\lambda$  from tidal signals.

Solórzano-Rivas and Werner (2020) recently compared the circular solution to the widely used analytical solution of Ferris (1951) (hereafter the “Ferris solution”), which applies to straight coastlines. Solórzano-Rivas and Werner (2020) demonstrated that application of the Ferris solution to tidal propagation in curved boundaries may be valid (within 10% error) for distances from the shoreline of up to about 20% of the island radius; however, it may incur errors of up to 80% towards the island centre. They also provided a relationship between the Ferris and circular solutions for the estimation of tidal amplitude decay and phase shift and adopted this as a correction factor to the Ferris solution.

Previous studies indicate that values of  $\lambda$  inferred from field-based observations of groundwater tidal amplitude differ to  $\lambda$  values obtained from field-based phase lag observations (e.g., Ferris, 1951; Smith, 1999; Rotzoll et al., 2008; Rotzoll et al., 2013). Trefry and Bekele (2004) used numerical modelling to identify different possible reasons for discrepancies between  $\lambda$  values obtained from the amplitude and phase. For instance, they tested different scenarios to represent a range of simplified real-world factors, such as unconfined flow, density-dependent flow, anisotropic aquifer properties, boundary geometry variability, and aquifer heterogeneity. They found that among the different explored processes, the dominant cause of inconsistent  $\lambda$  values (between amplitude-based and phase lag-based predictions) was aquifer heterogeneity. Specifically, they found that layering (variation in hydraulic conductivity with depth, adopting a high- $K$  bottom layer and a low- $K$  top layer) caused the largest discrepancy in  $\lambda$  estimates inferred from tidal amplitude and phase lag values. The above complexities of real-world settings are potential sources of “noise” in groundwater tides, which add to the challenges of extracting parameter estimates from tide-based approaches.

The objective of the present work is to demonstrate and critically assess the application of the circular solution to the estimation of aquifer hydraulic properties (i.e.,  $\lambda$ ) of orbiculate islands. The analysis is divided into four parts that reflect the study objectives: (1) The method is applied to a complex groundwater tide created by the combined effects of multiple ocean-tide constituents. The resulting multi-constituent (i.e., “compound”) groundwater tide is produced by applying the circular solution and assuming superposition. Rotzoll et al. (2008) also applied a compound tide using two tidal constituents to assess the applicability of their analytical solution to the estimation of aquifer properties. (2) A sensitivity analysis is undertaken to assess relationships between the predicted  $\lambda$  value and the tidal characteristics (i.e., amplitude and phase). (3) The Solórzano-Rivas and Werner (2020) correction factor (to the Ferris solution to allow its application to circular islands) for estimating  $\lambda$  is evaluated as a replacement to the circular solution. (4) The circular solution (devised for confined-aquifer conditions) is tested for applicability to unconfined aquifer conditions.

## **6.3 Methods**

### **6.3.1 Circular solution to tidal propagation**

Tidal propagation in a homogeneous, isotropic circular aquifer (i.e., an orbiculate-shaped island) can be resolved by solving the one-dimensional, axisymmetric groundwater flow equation (with tidal boundary conditions) in radial coordinates (Williams et al., 1970; Townley, 1995; Solórzano-Rivas and Werner, 2020). Here, the aquifer is assumed to be confined and of uniform geometry. Most island aquifers containing freshwater are more likely to be unconfined, especially for small-to-medium islands (e.g., Werner et al., 2017). Thus, the application of the confined aquifer solution to unconfined aquifers is an approximation, which we evaluate. Figure 6.1 shows a schematic island cross section in radial coordinates, subject to a tidal force at the seaward boundary.

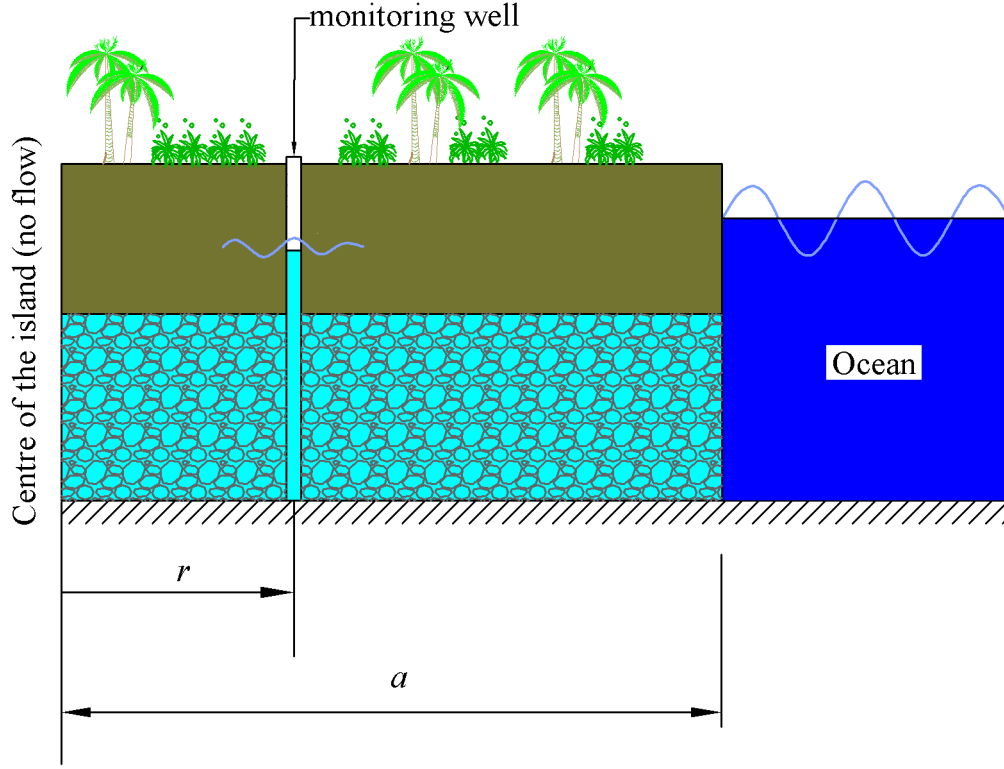


**Figure 6.1** Schematic of the conceptual model adopted by the circular solution (i.e., confined conditions), showing a vertical cross section of a circular island subjected to tidal forcing at the shoreline (i.e., ocean tide), where  $r$  is the radial distance from the centre of the island, and  $a$  is the island radius. The monitoring well within the aquifer allows for observations of tidal groundwater heads.

The circular solution, described by Solórzano-Rivas and Werner (2020), is given as:

$$h(t) = A_g \sin(\omega t - \varphi) \quad (6.1)$$

where:

$$A_g = A_0 \sqrt{c^2 + d^2} \quad (6.2)$$

$$c = \Re \left\{ \frac{I_0(\gamma r)}{I_0(\gamma a)} \right\} \quad (6.3)$$

$$d = \Im \left\{ \frac{I_0(\gamma r)}{I_0(\gamma a)} \right\} \quad (6.4)$$

$$\varphi = \tan^{-1}(-d/c) \quad (6.5)$$

Here,  $h$  is the groundwater elevation [L] with respect to mean sea level (MSL),  $A_g$  is the groundwater tidal amplitude [L],  $A_0$  is the tidal amplitude at the shoreline [L],  $\omega$  is the tidal angular frequency [rad T<sup>-1</sup>],  $t$  is time [T], and  $\varphi$  is the phase lag [rad] relative to the ocean tide.  $\Re$  and  $\Im$  indicate the real and imaginary parts (respectively) of the complex-valued function  $\frac{I_0(\gamma r)}{I_0(\gamma a)}$ ,  $I_0$  is the Modified Bessel function of the first kind of order zero (e.g., Abramowitz and Stegun, 1965), and  $\gamma$  is  $\beta\sqrt{i}$ , where  $\beta = \sqrt{\omega S/T}$ , and  $S$  and  $T$  are the storativity [-] and transmissivity [L<sup>2</sup> T<sup>-1</sup>], respectively.

### 6.3.2 Generation of synthetic ocean tides

Ocean tides comprise different tidal constituents. For example, the seven constituents: M<sub>2</sub>, S<sub>2</sub>, N<sub>2</sub>, K<sub>1</sub>, K<sub>2</sub>, P<sub>1</sub> and O<sub>1</sub> account for more than approximately 80% of real-world tides (Kvale, 2012). In this study, a synthetic compound tide, created as the sum of three tidal constituents, is used for the shoreline boundary condition, as outlined in Table 6.1. Constituent 1 is the oceanic semidiurnal lunar tide M<sub>2</sub> (tidal period,  $\tau = 12.42$  hours). M<sub>2</sub> is the principal tidal constituent in oceanic tides with the largest amplitude tidal potential (Doodson, 1954). Constituent 2 is the lunar-solar diurnal principal constituent K<sub>1</sub> ( $\tau = 23.93$  hours) and Constituent 3 is the compound tide MK<sub>3</sub> that arises from the combination of M<sub>2</sub> and K<sub>1</sub> when they pass through shallow-water depths (e.g., Luick, 2004). MK<sub>3</sub> is adopted because the amplitude and velocity of ocean tides are disturbed in shallow sea depths due to the friction effects, thereby altering the otherwise simple harmonic characteristics of the tides that occur in deeper waters (e.g., Godin, 1972). These effects can be treated as the appearance of new harmonics of the original frequency, defined as shallow-water tides (e.g., Gallagher and Munk, 1971; Godin, 1972; Stewart, 2008). Godin (1972) recommended as normal practice the inclusion of shallow-water constituents in the analysis of tides that reach the coastline, because they are always present in seawater bodies of shallow depth, including estuaries and bays, as long as these are hydraulically connected to the ocean. This approach is an improvement over previous studies that test tidal propagation methods, because these almost exclusively neglect shallow-water tides.

**Table 6.1** Amplitudes ( $A_0$ ), periods ( $\tau$ ) and frequencies ( $f$ ) of the constituents forming the synthetic tides of the current study.

Constituent name	$A_0$ [m]	$\tau$ [hour]	$f = 1/\tau$ [cycles/hour]
M <sub>2</sub>	1.3	12.42	0.0805
K <sub>1</sub>	0.9	23.93	0.0418
MK <sub>3</sub>	0.5	8.18	0.1222

### 6.3.3 Tidal propagation – ‘Observed’ groundwater tides

A base case model was developed for a hypothetical, small island of  $a = 3000$  m, and three scenarios were considered to represent different values of  $\lambda$  (i.e.,  $\lambda_1 = 150,000$  m<sup>2</sup>/d,  $\lambda_2 = 350,000$  m<sup>2</sup>/d and  $\lambda_3 = 500,000$  m<sup>2</sup>/d). These values are within the normal range of  $T/S$  found for real islands (e.g., Trefry and Bekele, 2004; Cabrera and Custodio, 2004). The circular solution was then applied to create data (i.e., synthetic tidal groundwater hydrographs) that we treat as surrogates for field observations, using these parameters. Observed data were produced at three inland locations; namely, at distances from the shoreline equal to 10%, 20% and 30% of the island radius (i.e.,  $0.1a$ ,  $0.2a$  and  $0.3a$ ) for both confined and unconfined conditions.

The circular solution was used to create compound tidal conditions through the application of superposition, whereby compound oceanic tides are taken as the sum of individual constituents (i.e., M<sub>2</sub>, K<sub>1</sub> and MK<sub>3</sub>). Superposition applies to confined-aquifer problems because of linearity in the relevant theory, whereas tidal propagation in unconfined aquifers is non-linear, although it is common practice to linearise unconfined groundwater flow for mathematical convenience (Bear, 1979).

The application of the circular solution (and superposition) to the propagation of a compound tidal signal was firstly compared to the results of confined-aquifer numerical simulations to confirm the methodology, similar to the verification undertaken by Solórzano-Rivas and Werner (2020) for a single tide. Numerical modelling adopted a version of SEAWAT modified by Post (2011) to allow the simulation of tidal boundary conditions, namely through implementation of the Periodic Boundary Condition (PBC package) using the methodology described by Langevin (2008) to adjust the input parameters of SEAWAT to represent radial flow coordinates. The PBC package allows the user to define a multiple-constituent tide at the

shoreline boundary. Comparison between the numerical model and the analytical solution showed an excellent match, as expected. For example, at the distance from the shoreline equal to  $0.3a$  and the  $\lambda_2$ -scenario (i.e.,  $350,000 \text{ m}^2/\text{d}$ ), the root-mean-square error (RMSE) was  $0.004 \text{ m}$  (see Table 6.1 for tidal amplitudes). Solórzano-Rivas and Werner (2020) showed the same good agreement between analytical and numerical results using SEAWAT (Post, 2011) when only one tidal constituent was used.

Numerical models using SEAWAT (Post, 2011) were used to create tidal propagation in unconfined conditions, for which superposition does not strictly apply, thereby restricting the application of superposition in assessments of compound tides based on analytical solutions. The same three  $\lambda$ -scenarios (i.e.,  $150,000 \text{ m}^2/\text{d}$ ,  $350,000 \text{ m}^2/\text{d}$  and  $500,000 \text{ m}^2/\text{d}$ ) used with confined conditions were analysed in the numerical modelling of unconfined aquifers. Unconfined simulations involved tidal variations in the aquifer thickness, which creates fluctuations in  $T$ , while storativity remains time-invariant. We adopted the same storativity in both unconfined and confined numerical models (even though specific yield in unconfined aquifers is typically several orders of magnitude higher than the storativity of confined aquifers) to isolate the effects of tidal depth changes on the application of the circular solution to unconfined conditions. To reproduce those three  $\lambda$ -scenarios in a fluctuating water table, the numerical model was designed so the time-averaged aquifer thickness over one tide period is  $10 \text{ m}$ , considering that the model bottom elevation is  $-10 \text{ m}$ , the top model elevation is  $+2 \text{ m}$ , and mean sea level has an elevation of  $0 \text{ m}$ . However, unconfined aquifer simulations to generate observed groundwater tides adopted a monochromatic tidal signal, using only the  $K_1$  constituent, which travelled further into the unconfined aquifer (due to its lower tidal frequency,  $f$ , Table 6.1) than the other higher-frequency tides. This led to groundwater tidal amplitudes that were higher than the minimum threshold for field measurement with a standard water level logger (i.e.,  $A > 1 \text{ cm}$ ) at the three inland locations and three  $\lambda$ -scenarios. For example, groundwater amplitudes from the tidal constituent  $M_2$  and the largest diffusivity scenario (i.e.,  $500,000 \text{ m}^2/\text{d}$ ) were less than  $1.5 \text{ mm}$  at the three locations (results shown at Table A9 in Appendix A).

The observations of synthetic groundwater tides obtained through application of the radial analytical solution to the three inland locations are termed “theoretical observations” hereafter.

The groundwater tides obtained from numerical modelling are described as “numerical observations”. Field measurements of coastal groundwater tides invariably show the influence of non-tidal factors, due to, for example, time-variant recharge and pumping, spatial heterogeneity, measurement error, and aquifer geometry variability (e.g., Erskine, 1991). To reflect these departures from the idealised sinusoidal signals inherent in theoretical and numerical observations, random noise was added to these otherwise idealised signals. The resulting new sets of observed data are referred to as “theoretical observations with noise” and “numerical observations with noise”. Noise was generated in two steps. First, a random uniform distribution over the range -0.025 m to 0.025 m was created to represent device error and other complications in the measurement process, based on typical pressure transducer error (adopting 50 m of measuring range and accuracy of  $\pm 0.05\%$ ; In-Situ Inc., 2020). A second set of random values was generated using a normal distribution of mean equal to 0.00 m and standard deviation of 0.01 m to emulate other complicating factors on groundwater levels. The two random error time-series were then added to theoretical and numerical observations. While the choice of noise parameters is effectively arbitrary, the noise statistical properties selected here produced synthetic groundwater tides that appear from visual inspection as roughly similar to real-world groundwater hydrographs (e.g., Merrit, 2004; Xun et al., 2006). Figure 6.2 shows an example of two hypothetical groundwater tides based on theoretical observations and theoretical observations with noise.

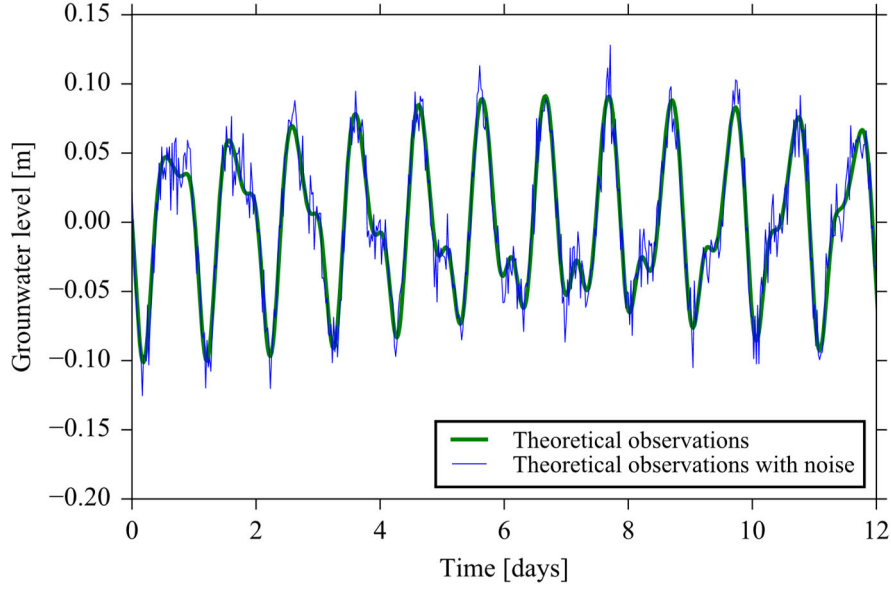


**Figure 6.2** Two examples of synthetic groundwater tides, representing a distance from the shoreline equal to  $0.2a$ , for the  $\lambda_1$ -scenario (i.e.,  $\lambda = 150,000 \text{ m}^2/\text{d}$ ). The green line represents theoretical observations and the blue line shows theoretical observations with noise. Groundwater levels are relative to mean sea level.

### 6.3.4 Harmonic analysis

Harmonic analysis of synthetic groundwater tides was undertaken to obtain ‘observed’ groundwater amplitudes and phase lags (e.g., Figure 6.2), for every tidal component, i.e., the  $M_2$ ,  $K_1$  and  $MK_3$  constituents. This was achieved using discrete linear least-squares estimation (LSE) (e.g., Kay, 1993). Amplitudes and phase lags from theoretical observations are denoted as  $A_{g,obs}$  and  $\varphi_{obs}$ , respectively. Corresponding parameters for other synthetic time-series include:  $A'_{g,obs}$  and  $\varphi'_{obs}$  (theoretical observations with noise),  $A_{n,obs}$  and  $\varphi_{n,obs}$  (numerical observations), and  $A'_{n,obs}$  and  $\varphi'_{n,obs}$  (numerical observations with noise).

LSE presumes that the observed groundwater tides can be described by (e.g., Boon and Kiley, 1978):

$$y(t) = \sum_{j=1}^n A_{gj} \cos(\omega_j t - \varphi_{obsj} - \pi/2); t = 0, \Delta T, 2\Delta T, \dots, (N-1)\Delta T \quad (6.6)$$

where  $y$  is the groundwater level [L] with respect to MSL,  $j$  is the tidal constituent,  $n$  is the total of tidal constituents analysed (i.e.,  $n = 3$ ), and  $N$  is the total number of data points, such that  $N = t_s/\Delta T$ , where  $t_s$  and  $\Delta T$  are the total simulation time and sampling time step, respectively.  $\Delta T$  was set to 30 min. Equation (6.6) adopts a cosine function and subtracts  $\pi/2$  from the argument (rather than the sine function of equation (6.1)) to conform with the approach of Boon and Kiley (1978). While the formulations presented in this section are expressed as functions of  $A_{g,obs}$  and  $\varphi_{obs}$ , the same harmonic analysis was applied to obtain  $A'_{g,obs}/\varphi'_{obs}$ ,  $A_{n,obs}/\varphi_{n,obs}$  and  $A'_{n,obs}/\varphi'_{n,obs}$ .

A convenient way to express equation (6.6) for LSE procedures is as follows:

$$y(t) = \sum_{j=1}^n \alpha_{1j} \cos(\omega_j t) + \sum_{j=1}^n \alpha_{2j} \sin(\omega_j t); t = 0, \Delta T, 2\Delta T, \dots, (N-1)\Delta T \quad (6.7)$$

Here,  $\alpha_{1j} = A_{g,obsj} \cos(\varphi_{obsj} + \pi/2)$  and  $\alpha_{2j} = A_{g,obsj} \sin(\varphi_{obsj} + \pi/2)$ .

Equation (6.7) can be expressed in matrix notation (represented by bold fonts) as  $\mathbf{y} = \mathbf{H}\hat{\boldsymbol{\theta}}$ , where  $\mathbf{H}$  is a matrix of dimensions  $N \times 2n$  composed of the sine and cosine terms in Equation (6.7), and  $\hat{\boldsymbol{\theta}}$  is the least squares approximation of  $\alpha_{1j}$  and  $\alpha_{2j}$ , with dimensions  $2n \times 1$ , that can be computed as (e.g., Kay, 1993):

$$\hat{\boldsymbol{\theta}} = (\mathbf{H}^T \mathbf{H})^{-1} \mathbf{H}^T \mathbf{y} \quad (6.8)$$

where the superscripts  $T$  and  $-1$  in equation (6.8) indicate the matrix transpose and inverse, respectively. Then, the observed tidal parameters,  $A_{g,obs}$  and  $\varphi_{obs}$ , can be estimated as:

$$A_{g,obsj} = \sqrt{\alpha_{1j}^2 + \alpha_{2j}^2} \quad (6.9)$$

$$\varphi_{obsj} = \tan^{-1}(\alpha_{2j}/\alpha_{1j}) - \pi/2 \quad (6.10)$$

Given the form of equation (6.10)  $\varphi_{obs}$  does not increase monotonically with distance, as occurs in reality. Rather, phase lags greater than  $2\pi$  are output as  $\varphi_{obs} - 2\pi$ . This differs from the Ferris

solution, whereby the phase lag increases monotonically with distance, as expected. Although this has no implications for the inverse problem of estimating  $\lambda$  using the circular solution, it affects  $\lambda$  estimation from the corrected Ferris solution, which requires the complete phase lag. That is, we account for the number of tidal cycles that have transpired in estimating  $\lambda$  using the corrected Ferris solution, where the phase lag exceeds a tidal cycle, i.e.,  $\varphi_{\text{obs}} > 2\pi$ .

It is expected that the observed groundwater amplitudes and phase lags obtained from harmonic analysis of theoretical observations with noise and numerical observations both with and without noise (i.e.,  $A'_{\text{g,obs}}/\varphi'_{\text{obs}}$ ,  $A'_{\text{n,obs}}/\varphi'_{\text{n,obs}}$  and  $A_{\text{n,obs}}/\varphi_{\text{n,obs}}$ ) will show some departures from the corresponding theoretical observations,  $A_{\text{g,obs}}$  and  $\varphi_{\text{obs}}$ . These departures were estimated and expressed as relative errors, as follows:

$$E_A = \frac{(A'_{\text{g,obs}} - A_{\text{g,obs}})}{A_{\text{g,obs}}} \times 100 \quad (6.11)$$

$$E_\varphi = \frac{(\varphi'_{\text{obs}} - \varphi_{\text{obs}})}{\varphi_{\text{obs}}} \times 100 \quad (6.12)$$

Equations (6.11) and (6.12) also apply for discrepancies between  $A_{\text{n,obs}}$ ,  $\varphi_{\text{n,obs}}$ ,  $A'_{\text{n,obs}}$ ,  $\varphi'_{\text{n,obs}}$  and the corresponding  $A_{\text{g,obs}}$  and  $\varphi_{\text{obs}}$  values.

### 6.3.5 Determination of $\lambda$ through application of the circular solution

In the case of the circular solution,  $\lambda$  can only be determined through iterative methods, since  $T$  and  $S$  are part of the argument ( $\gamma$ ) of the Modified Bessel functions (see equations (6.2) and (6.3)), which cannot be directly inverted. Here, an optimization technique is used; namely, the Nelder- Mead Simplex method (Nelder and Mead, 1965), which is applied within the algorithm implemented in the Python function `scipy.optimize.fmin`. Parameter estimation is performed by the minimisation of two objective functions,  $O_a(\lambda_A)$  and  $O_p(\lambda_\phi)$ , which represent discrepancies between model-estimated and observed diffusivity values of the tidal amplitude ( $\lambda_A$ ) and phase lag ( $\lambda_\phi$ ), respectively. The objective functions are given by:

$$O_a(\lambda_A) = (A_{g,\text{obs}} - A_g)^2 \quad (6.13)$$

$$O_p(\lambda_\varphi) = (\varphi_{\text{obs}} - \varphi)^2 \quad (6.14)$$

where  $A_{g,\text{obs}}$  and  $\varphi_{\text{obs}}$  are obtained through harmonic analysis (Section 6.3.4), and  $A_g$  and  $\varphi$  are the values obtained from equations (6.2) and (6.5), respectively.

We first verified that the two objective functions given in equations (6.13) and (6.14) provide the same  $\lambda$  values as the original values used in the base case model that generated the synthetic observations (see Section 6.3.3). This was undertaken initially on theoretical observations (i.e., without noise) to provide a check on our implementation of the methodology and equations to determine  $\lambda$ . A perfect match was obtained (results are not shown here for brevity), thereby affirming the technique for ideal measurement datasets. The use of tidal parameters based on theoretical observations with noise (i.e.,  $A'_{g,\text{obs}}$  and  $\varphi'_{\text{obs}}$ ) is expected to lead to differences in the calculations of  $\lambda_A$  and  $\lambda_\varphi$  (i.e., from inversion) due to the influence of noise, as discussed earlier. In addition to objective functions based only on amplitude or phase lag misfit (i.e., equation (6.13) and equation (6.14), respectively), a multi-objective function was tested to explore values of  $\lambda$  that arise by combining both amplitude and phase lag misfit. The multi-objective function was determined as:

$$O_{a,p}(\lambda_{A,\varphi}) = (A_{g,\text{obs}} - A_g)^2 + (\varphi_{\text{obs}} - \varphi)^2 \quad (6.15)$$

Note that the amplitude and phase misfits are weighted equally in  $O_{a,p}(\lambda_{A,\varphi})$ , following the approach of Trefry and Bekele (2004). This approach was verified by the perfect match (e.g., errors  $< 10^{-8}\%$ ) obtained between the  $\lambda_{A,\varphi}$  estimates (i.e., by minimisation of equation 6.15) and the known  $\lambda$  values.

In this study, the three objective functions (i.e., equations (6.13), (6.14) and (6.15)) are applied to estimate  $\lambda$ , namely, when observed parameters (amplitude and phase lags) are extracted from observations (theoretical and numerical) with noise. The average diffusivity ( $\lambda_{\text{av}} = (\lambda_A + \lambda_\varphi)/2$ )

was also computed. The relative error,  $E_r$ , with respect to the known  $\lambda$  value, and identified as  $\lambda_{\text{specified}}$ , adopted in creating synthetic observations in the three scenarios studied (i.e., 150,000 m<sup>2</sup>/d, 350,000 m<sup>2</sup>/d and 500,000 m<sup>2</sup>/d) was then calculated as:

$$E_r = \frac{(\lambda_A - \lambda_{\text{specified}})}{\lambda_{\text{specified}}} \times 100 \quad (6.16)$$

$E_r$  values that apply to alternative methods for estimating  $\lambda$  were obtained by substituting  $\lambda_\phi$ ,  $\lambda_{A,\phi}$ , and  $\lambda_{\text{av}}$  into equation (6.16).

### 6.3.6 Sensitivity analysis

A sensitivity analysis was conducted to assess the sensitivity of diffusivity (i.e.,  $\lambda_A$  and  $\lambda_\phi$ ) to differences in  $A_{g,\text{obs}}$  and  $\phi_{\text{obs}}$ , to explore the effect of discrepancies in  $A'_{g,\text{obs}}$ ,  $\phi'_{\text{obs}}$ ,  $A_{n,\text{obs}}$ ,  $\phi_{n,\text{obs}}$ ,  $A'_{n,\text{obs}}$ , or  $\phi'_{n,\text{obs}}$  on the estimation of  $\lambda$ . Synthetic observations did not incorporate any noise. The following discrete form for non-dimensional local sensitivity (e.g., Robinson and Werner, 2017) was adopted:

$$S = \frac{p\Delta o}{o\Delta p} \quad (6.17)$$

Here,  $S$  is the non-dimensional local sensitivity,  $p$  is the input parameter (i.e.,  $A_{g,\text{obs}}$  or  $\phi_{\text{obs}}$ )  $o$  is the output parameter (i.e.,  $\lambda_A$  or  $\lambda_\phi$ ) and  $\Delta$  represents a discrete change. Applying a central finite-difference approximation and assuming that  $\delta = \frac{\Delta p}{p}$ , equation (6.17) can be written as:

$$S = \frac{o(p+\Delta p) - o(p-\Delta p)}{2o\delta} \quad (6.18)$$

In this study, a value of  $\delta$  of 0.005 (0.5%) was adopted.

### 6.3.7 Application of the Solórzano-Rivas and Werner (2020) correction factor

Solórzano-Rivas and Werner (2020) found that when the aquifer properties lead to magnitudes of  $|\gamma r| \geq 2$  and  $|\gamma a| \geq 2$ ,  $\varphi \approx \varphi_F$  and  $A_g \approx A_{gF} \sqrt{a/r}$ , where  $A_{gF}$  and  $\varphi_F$  are the amplitude tide and phase lag (respectively) estimated by the Ferris solution. This allows for the application of the Solórzano-Rivas and Werner (2020) correction factor to the Ferris solution, which provides for a simpler calculation of  $\lambda$ , whereby amplitude-based and phase lag-based estimates of  $\lambda$ , i.e.,  $\lambda_{AF}$  and  $\lambda_{\varphi F}$ , respectively, are as follows:

$$\lambda_{AF} \approx \frac{\omega(r-a)^2}{2 \left[ \ln \left( \frac{A_{g,obs} \sqrt{r}}{A_0 \sqrt{a}} \right) \right]^2} \quad (6.19)$$

$$\lambda_{\varphi F} \approx \frac{\omega(a-r)^2}{2\varphi_{obs}^2} \quad (6.20)$$

The average diffusivity, ( $\lambda_{avF} = (\lambda_{AF} + \lambda_{\varphi F})/2$ ), is also included as an additional approach to  $\lambda$  estimation. To assess the correction factor applicability, the relative errors between the different approaches (i.e.,  $\lambda_{AF}$ ,  $\lambda_{\varphi F}$ ,  $\lambda_{avF}$ ) and the specified  $\lambda$  in the three  $\lambda$ -scenarios (i.e., 150,000 m<sup>2</sup>/d, 350,000 m<sup>2</sup>/d and 500,000 m<sup>2</sup>/d) was computed as equation (6.16).

Solórzano-Rivas and Werner (2020) found that the error in applying the Ferris solution (without correction) to tidal propagation in circular aquifers is about 10% for inland distances of  $0.2a$ , beyond which larger errors were obtained with increasing inland distance. Here, we extend the calculation of Ferris solution errors by determining the island size for which the error in the Ferris solution is 1%. This was achieved using a least-squares optimization technique applied to the M<sub>2</sub>-constituent,  $\lambda_2$ -scenario, and adopting inland distances (where the Ferris solution error is 1%) of 300 m, 600 m and 900 m.

The following flowchart (Figure 6.3) provides an explanation of the type of observed data (i.e., theoretical observations, theoretical observations with noise, numerical observations and numerical observations with noise) adopted for the application of both the circular solution and

corrected Ferris solution in the estimation of  $\lambda$ . Figure 6.3 shows the procedure for both confined and unconfined conditions.

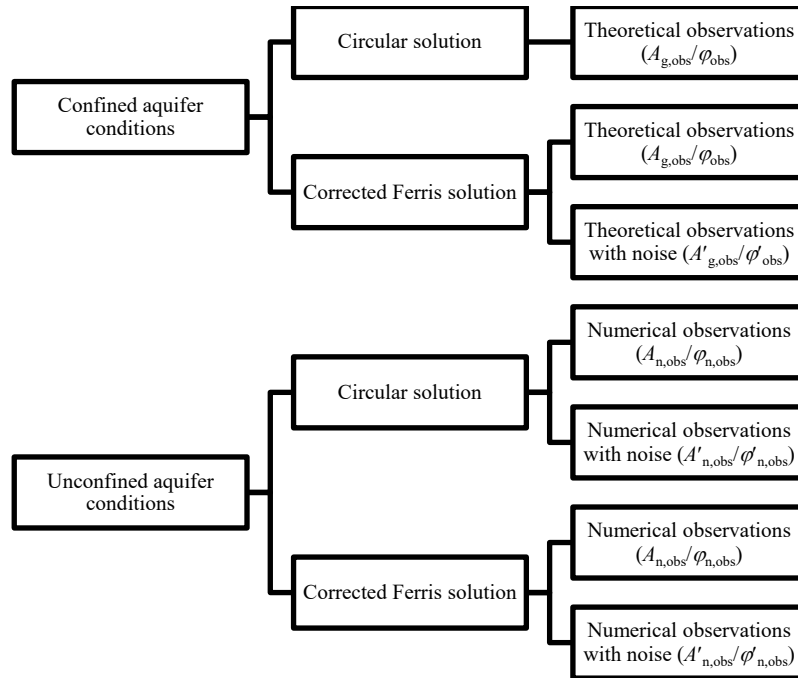


**Figure 6.3** Schema of input data for the application of the circular solution and the corrected Ferris solution in the estimation of  $\lambda$  for both confined and unconfined aquifer conditions.

## 6.4 Results and Discussion

### 6.4.1 Assessment of harmonic analysis of observed data

This section presents the observed amplitude and phase lags estimated from harmonic analysis of the different synthetic times series, including for both confined and unconfined aquifer conditions. Table 6.2 shows the observed tidal parameters under confined conditions, that is, parameters from harmonic analysis of theoretical observations ( $A_{g,obs}$  and  $\varphi_{obs}$ ) and of theoretical observations with noise ( $A'_{g,obs}$  and  $\varphi'_{obs}$ ), and the relative difference between them. Values of  $A_{g,obs}$  or  $A'_{g,obs}$  lower than 2.5 cm are within the likely bounds of uncertainty of field measurements, considering a pressure transducer with 50 m measuring range and accuracy of  $\pm 0.05\%$  (e.g., In-Situ Inc., 2020). Results shown in Table 6.2 correspond to the observations at

locations equal to  $0.1a$ ,  $0.2a$  and  $0.3a$  for every tidal constituent and for the three  $\lambda$ -scenarios specified in the base case model.

**Table 6.2** Comparison of parameters obtained from harmonic analysis of theoretical observations and of theoretical observations with noise under confined conditions. Signals that have moved into the next tidal cycle are denoted by \*. Results based on amplitudes smaller than 2.5 cm (i.e., within the limits of measurement techniques) are denoted by †.

$\lambda$ - scenario [m <sup>2</sup> /d]	Distance from the shoreline	Constituent ( $A_0, \tau$ )	Theoretical observations		Theoretical observations with noise		Relative error	
			$A_{g,obs}$ [m]	$\varphi_{obs}$ [rad]	$A'_{g,obs}$ [m]	$\varphi'_{obs}$ [rad]	$E_A$ [%]	$E_\varphi$ [%]
$\lambda_1 =$ <b>150,000</b>	$0.1a$	$K_1$	0.240	1.376	0.240	1.386	0.041	0.032
	$0.2a$	(0.9 m,	0.064	2.751	0.065	2.750	0.191	-0.043
	$0.3a$	23.93 hr)	0.017†	4.127†	0.017†	4.119†	-0.287†	-0.189†
	$0.1a$	$M_2$	0.203	1.909	0.204	1.910	0.125	0.077
	$0.2a$	(1.3 m,	0.032	3.818	0.032	3.807	0.627	-0.276
	$0.3a$	12.42 hr)	0.005†	5.727†	0.005†	5.711†	-7.58†	-0.280†
	$0.1a$	$MK_3$	0.050	2.352	0.050	2.357	-0.343	0.201
	$0.2a$	(0.5 m,	0.005†	4.704†	0.005†	4.696†	5.72†	-0.175†
	$0.3a$	8.18 hr)	0.001†	0.773*†	0.003†	0.217*†	-35.9†	71.9†
$\lambda_2 =$ <b>350,000</b>	$0.1a$	$K_1$	0.386	0.901	0.385	0.900	-0.148	0.004
	$0.2a$	(0.9 m,	0.167	1.802	0.166	1.800	-0.206	0.152
	$0.3a$	23.93 hr)	0.072	2.704	0.073	2.703	-0.202	0.281
	$0.1a$	$M_2$	0.393	1.250	0.393	1.250	0.021	0.024
	$0.2a$	(1.3 m,	0.120	2.500	0.120	2.502	0.116	-0.013
	$0.3a$	12.42 hr)	0.037	3.750	0.037	3.752	0.017	-0.104
	$0.1a$	$MK_3$	0.113	1.540	0.113	1.539	0.116	-0.047
	$0.2a$	(0.5 m,	0.026	3.080	0.026	3.075	-0.301	-0.169
	$0.3a$	8.18 hr)	0.006†	4.620†	0.006†	4.633†	-2.29†	0.277†
$\lambda_3 =$ <b>500,000</b>	$0.1a$	$K_1$	0.447	0.754	0.447	0.754	-0.127	-0.021
	$0.2a$	(0.9 m,	0.224	1.509	0.223	1.510	-0.206	0.100
	$0.3a$	23.93 hr)	0.113	2.264	0.113	2.268	-0.092	0.220
	$0.1a$	$M_2$	0.482	1.046	0.482	1.046	0.012	0.026
	$0.2a$	(1.3 m,	0.180	2.092	0.180	2.092	0.079	0.005
	$0.3a$	12.42 hr)	0.068	3.139	0.068	3.137	0.129	-0.054
	$0.1a$	$MK_3$	0.145	1.289	0.146	1.288	0.101	-0.025
	$0.2a$	(0.5 m,	0.043	2.577	0.043	2.574	-0.009	-0.141
	$0.3a$	8.18 hr)	0.013†	3.867†	0.012†	3.863†	-1.19†	-0.082†

Values in Table 6.2 show an attenuation of  $A_{g,obs}$  (and  $A'_{g,obs}$ ) and an increase of  $\varphi_{obs}$  (and  $\varphi'_{obs}$ ) with distance, as expected. Another expected outcome is the higher relative tidal efficiency,  $A_{g,obs}/A_0$  (and  $A'_{g,obs}/A_0$ ), for the  $\lambda_3$ -scenario (i.e., 500,000 m<sup>2</sup>/d) for all tidal constituents. Interpretation of phase lag results needed to account for the number of cycles that have occurred

at each location, for reasons given earlier. For example, the values marked with “\*” represent phase lags requiring adjustment to add complete cycles to the phase lag estimate arising from harmonic analysis. These were apparent from phase lags that did not increase monotonically with distance from the shoreline. For example, the phase lag reduces between  $0.2a$  and  $0.3a$  for the MK<sub>3</sub> constituent,  $\lambda_1$ -scenario because a new cycle had started prior to the wave reaching  $0.3a$  from the shoreline. The circular solution has the advantage of ignoring phase changes that were greater than a complete tidal cycle, and therefore the values with the “\*” in Table 6.2 were used (without any correction) for the inverse estimation of  $\lambda$  using the circular solution. However, correction through the addition of  $2\pi k$  (where  $k$  is the number of complete cycles that have occurred) was needed to account for phase changes in applying the correction factor to the Ferris solution for the estimation of  $\lambda$ .

The tidal parameters obtained using harmonic analysis of theoretical observations (i.e.,  $A_{g,obs}$  and  $\varphi_{obs}$ ; without noise added) perfectly matched (e.g., errors  $< 10^{-15}\%$ ) the values of  $A_g$  and  $\varphi$  obtained from the circular solution (i.e., applying equations (6.2) and (6.5)), as expected. This confirms the reliability of the harmonic analysis methodology. However, there were discrepancies in  $A'_{g,obs}$  and  $\varphi'_{obs}$  (i.e., relative to  $A_g$  and  $\varphi$ ) when harmonic analysis was applied to theoretical observations with noise. These discrepancies are expressed in terms of the relative errors,  $E_A$  and  $E_\varphi$ , given by equations (6.11) and (6.12), respectively. Table 6.2 shows that  $|E_A| > |E_\varphi|$  with some exceptions (i.e., for some cases with  $\lambda$  values of 350,00 and 500,000 m<sup>2</sup>/d), indicating that generally, harmonic analysis led to larger errors in amplitude than phase lag when analysing theoretical observations with noise. The reason for this difference in errors may be associated with the fact that noise influences groundwater levels without affecting the observation time. This is apparent, for example, in high tides in theoretical observations with noise that occur at similar times to those of theoretical observations without noise (see Figure 6.2), even though the high tide elevations differ. Given this, it is likely that the uncertainty in amplitude exceeds that of the phase.

Table 6.3 shows observed parameters (i.e., amplitude and phase lag) obtained from the harmonic analysis of unconfined aquifer observations when noise is not included, namely numerical observations. Results from numerical observations with noise, are presented in Table A8 in Appendix A. Table 6.3 shows the observed parameters  $A_{n,obs}$  and  $\varphi_{n,obs}$ , and Table A8

shows the observed parameters  $A'_{n,obs}$  and  $\phi'_{n,obs}$ . Results are given at the inland locations of  $0.1a$ ,  $0.2a$  and  $0.3a$  for the  $K_1$  constituent and all three  $\lambda$ -scenarios. Tables 6.3 and S8 also present relative errors ( $E_A$  and  $E_\phi$ ) in  $A_{n,obs}/\phi_{n,obs}$  and  $A'_{n,obs}/\phi'_{n,obs}$  with respect to the corresponding observed parameters,  $A_{g,obs}$  and  $\phi_{obs}$ , to assess the effect of applying the circular solution (which is formulated for confined conditions) to unconfined aquifers. Relative errors in amplitudes and phase lags are calculated using equations (6.11) and (6.12), respectively.

**Table 6.3** Parameters obtained from the harmonic analysis of numerical observations for unconfined conditions ( $A_{n,obs}$  and  $\phi_{n,obs}$ ) for the  $K_1$  constituent, and their respective relative errors. Amplitude values smaller than 2.5 cm are denoted by †.

$\lambda$ -scenario [m <sup>2</sup> /d]	Distance from the shoreline	Numerical observations		$E_A$ [%]	$E_\phi$ [%]
		$A_{n,obs}$ [m]	$\phi_{n,obs}$ [rad]		
$\lambda_1 = 150,000$	$0.1a$	0.237	1.361	-1.200	-1.024
	$0.2a$	0.063	2.725	-2.216	-0.991
	$0.3a$	0.017†	4.089†	-3.263†	-1.119†
$\lambda_2 = 350,000$	$0.1a$	0.383	0.892	-0.808	-1.024
	$0.2a$	0.164	1.784	-1.644	-1.039
	$0.3a$	0.071	2.678	-2.374	-0.955
$\lambda_3 = 500,000$	$0.1a$	0.444	0.747	-0.681	-0.999
	$0.2a$	0.221	1.493	-1.365	-1.054
	$0.3a$	0.110	2.241	-2.048	-0.999

A comparison of Tables 6.3 and A8 shows that the errors,  $E_A$  and  $E_\phi$ , are of the same order of magnitude when observations are with and without noise. This implies that the noise added to the numerical observations (i.e., of unconfined conditions) did not affect markedly the values of amplitude and phase lag obtained from harmonic analysis. Results in Tables 6.3 shows that  $|E_A|$  decreases with increasing  $\lambda$  and increases with inland distance from the shoreline. On the other hand, the range in  $|E_\phi|$  is smaller (-0.7% to 1.1%; see Table 6.3) than the range in  $|E_A|$  (-0.7% to 3.3%). It is noteworthy that in both situations (Tables 6.3 and A8), all relative errors are negative, implying that groundwater tides in unconfined aquifers experience more attenuation of tidal amplitude than in confined aquifers, even though the same value of storativity was adopted in both confined and unconfined situations. The reason for this outcome is a consequence of the changing transmissivity, due to the time-changing depth, during tidal fluctuations. Figure A1 in Appendix A compares the effects on groundwater tides of a time-

varying transmissivity due to a change in saturated depth (i.e., unconfined conditions) with the case of a time-constant transmissivity (i.e., confined conditions).

#### 6.4.2 Sensitivity analysis

Values of the non-dimensional local sensitivity ( $S$ ; equation (6.17)) of  $\lambda$  (obtained by inversion of the circular solution) to changes in  $A_{g,obs}$  and  $\varphi_{obs}$  for each tidal constituent are shown in Tables 6.4 and 6.5, respectively.

**Table 6.4** Sensitivity ( $S_A$ ) of  $\lambda_A$  to changes in  $A_{g,obs}$  for  $\delta = 0.5\%$ .\*

$\lambda$ -scenario [m <sup>2</sup> /d]	Distance from the shoreline	<b>K<sub>1</sub></b> $\tau = 23.93$ hr	<b>M<sub>2</sub></b> $\tau = 12.42$ hr	<b>MK<sub>3</sub></b> $\tau = 8.18$ hr
$\lambda_1 = 150,000$	0.1a	1.454	1.048	0.850
	0.2a	0.727	0.524	0.425
	0.3a	0.485	0.349	0.283
$\lambda_2 = 350,000$	0.1a	2.220	1.600	1.299
	0.2a	1.110	0.800	0.649
	0.3a	0.740	0.533	0.433
$\lambda_3 = 500,000$	0.1a	2.653	1.912	1.552
	0.2a	1.326	0.956	0.776
	0.3a	0.884	0.637	0.517

\*see Section 6.3.6

**Table 6.5** Sensitivity ( $S_\varphi$ ) of  $\lambda_\varphi$  to changes in  $\varphi_{obs}$  for  $\delta = 0.5\%$ \*. Scenarios leading to phase lags greater than one tidal cycle are denoted by ‡.

$\lambda$ -scenario [m <sup>2</sup> /d]	Distance from the shoreline	<b>K<sub>1</sub></b> $\tau = 23.93$ hr	<b>M<sub>2</sub></b> $\tau = 12.42$ hr	<b>MK<sub>3</sub></b> $\tau = 8.18$ hr
$\lambda_1 = 150,000$	0.1a	-2.002	-2.000	-2.001
	0.2a	-2.002	-2.001	-2.001
	0.3a	-2.002	-2.001	-0.219‡
$\lambda_2 = 350,000$	0.1a	-2.004	-2.002	-2.001
	0.2a	-2.005	-2.002	-2.002
	0.3a	-2.005	-2.003	-2.002
$\lambda_3 = 500,000$	0.1a	-2.006	-2.003	-2.002
	0.2a	-2.007	-2.003	-2.002
	0.3a	-2.008	-2.004	-2.003

\*see Section 6.3.6

Table 6.4 shows that the values of  $S_A$  are all positive, whereas  $S_\varphi$  given in Table 6.5 are all negative. This indicates that when  $A_{g,obs}$  increases,  $\lambda_A$  also increases (i.e., positively correlated).

Conversely, when  $\varphi_{\text{obs}}$  increases,  $\lambda_{\varphi}$  decreases (i.e., negatively correlated). Given that positive values of  $E_A$  signify  $A'_{\text{g,obs}} > A_{\text{g,obs}}$ ,  $A_{\text{n,obs}} > A_{\text{g,obs}}$ , or  $A'_{\text{n,obs}} > A_{\text{g,obs}}$ , and over-estimation of  $A_{\text{g,obs}}$  leads to overestimation of  $\lambda_A$ , it follows that positive values of  $E_A$  (Tables 6.2 and 6.3) indicate overestimation of  $\lambda_A$ , while  $\lambda_A$  will be underestimated if  $E_A$  is negative. The inverse occurs for  $E_{\varphi}$  (see Tables 6.2 and 6.3), whereby the negative values of  $S_{\varphi}$  in Table 6.5 indicate that  $\lambda_{\varphi}$  is underestimated when  $E_{\varphi}$  is positive, whereas  $\lambda_{\varphi}$  is overestimated when  $E_{\varphi}$  is negative.

The spatial variability in  $S_A$  (Table 6.4) is distinctly different to that of  $S_{\varphi}$  (Table 6.5). For example,  $S_{\varphi}$  is relatively constant (i.e.,  $\approx -2$ ) (with the exception of MK<sub>3</sub> constituent,  $\lambda_1$ -scenario at a distance of  $0.3a$ , Table 6.5), while there is a decreasing trend in  $S_A$  with distance from the shoreline (Table 6.4). The disparate value of  $S_{\varphi} = -0.219$  in Table 6.5 corresponds to a groundwater tidal signal for which a complete cycle had transpired. This result was corroborated by estimating  $S_{\varphi}$  at locations further inland than those given in Table 6.5. In those locations, the observed groundwater tide was similarly in the second or third cycle (as expected), and values of  $S_{\varphi}$  were found to be of a similar order of magnitude to  $-0.219$  (i.e., the value obtained at a distance of  $0.3a$ ; Table 6.5).

### 6.4.3 Inverse calculation of $\lambda$ applying the circular solution

#### 6.4.3.1 Circular solution for confined conditions

The  $\lambda_A$  and  $\lambda_{\varphi}$  estimates (confined aquifer conditions) obtained through minimisation of equations (6.13) to (6.15) are given in Table 6.6. The average of  $\lambda_A$  and  $\lambda_{\varphi}$ , equal to  $\lambda_{\text{av}}$ , is also included. Table A1 in Appendix A shows the relative error,  $E_r$  (equation (6.16)), in the  $\lambda$  estimates given in Table 6.6.

**Table 6.6**  $\lambda$  estimates ( $\lambda_A$ ,  $\lambda_\phi$  and  $\lambda_{A,\phi}$ ) from theoretical observations with noise ( $A'_{g,obs}$  and  $\phi'_{obs}$ ) for the three  $\lambda$ -scenarios, obtained by minimisation of equations (6.13) to (6.15).  $\lambda_{av}$  is the average of  $\lambda_A$  and  $\lambda_\phi$ . Note that at the inland distance of  $0.3a$  for the MK<sub>3</sub> constituent,  $\lambda_1$ -scenario, the  $\lambda_\phi$  estimate did not require the cycle correction mentioned in Section 6.4.1, even though the transpired phase lag is greater than  $2\pi$ .

$\lambda$ -scenario [m <sup>2</sup> /d]	Constituent	Distance from the shoreline	$\lambda_A$ [m <sup>2</sup> /d]	$\lambda_\phi$ [m <sup>2</sup> /d]	$\lambda_{A,\phi}$ [m <sup>2</sup> /d]	$\lambda_{av}$ [m <sup>2</sup> /d]
$\lambda_1 =$ <b>150,000*</b>	K <sub>1</sub> $\tau = 23.93$ hr	$0.1a$	150,089	149,904	149,914	149,996
		$0.2a$	150,208	150,128	150,128	150,168
		$0.3a$	149,792	150,569	150,569	150,180
	M <sub>2</sub> $\tau = 12.42$ hr	$0.1a$	150,196	149,769	149,786	149,982
		$0.2a$	150,492	150,830	150,830	150,661
		$0.3a$	145,953	150,843	150,843	148,398
	MK <sub>3</sub> $\tau = 8.18$ hr	$0.1a$	149,563	149,398	149,399	149,481
		$0.2a$	153,608	150,525	150,525	152,067
		$0.3a$	132,737	176,757	176,757	154,747
$\lambda_2 =$ <b>350,000**</b>	K <sub>1</sub> $\tau = 23.93$ hr	$0.1a$	348,853	349,973	349,827	349,413
		$0.2a$	349,200	348,936	348,943	349,068
		$0.3a$	350,522	348,035	348,047	349,278
	M <sub>2</sub> $\tau = 12.42$ hr	$0.1a$	350,116	349,831	349,869	349,973
		$0.2a$	350,324	350,093	350,096	350,208
		$0.3a$	350,032	350,733	350,732	350,383
	MK <sub>3</sub> $\tau = 8.18$ hr	$0.1a$	350,527	350,330	350,332	350,428
		$0.2a$	349,315	351,186	351,185	350,251
		$0.3a$	346,514	348,068	348,068	347,291
$\lambda_3 =$ <b>500,000**</b>	K <sub>1</sub> $\tau = 23.93$ hr	$0.1a$	498,323	500,210	499,893	499,267
		$0.2a$	498,635	498,998	498,981	498,817
		$0.3a$	499,594	497,798	497,820	498,696
	M <sub>2</sub> $\tau = 12.42$ hr	$0.1a$	500,110	499,736	499,807	499,923
		$0.2a$	500,379	499,951	499,964	500,165
		$0.3a$	500,412	500,539	500,538	500,475
	MK <sub>3</sub> $\tau = 8.18$ hr	$0.1a$	500,787	500,250	500,261	500,518
		$0.2a$	499,966	501,413	501,410	500,690
		$0.3a$	496,918	500,818	500,817	498,868

\* Initial value used in the optimization process 180,000 m<sup>2</sup>/d

\*\* Initial value used in the optimization process 380,000 m<sup>2</sup>/d

The values in Table 6.6 show that estimates of  $\lambda_\phi$  are similar to  $\lambda_{A,\phi}$ , whereas these differ to  $\lambda_A$ . For example,  $\lambda_\phi$  and  $\lambda_{A,\phi}$  are both 150,830 m<sup>2</sup>/d at a distance of  $0.2a$  for the M<sub>2</sub> constituent,  $\lambda_1$ -scenario, which differs to  $\lambda_A$  (i.e., 150,492 m<sup>2</sup>/d) for the same case. This arises because  $S_\phi$  (Table 6.5) is generally higher than  $S_A$  (Table 6.4). That is, the higher value of  $S_\phi$  leads to  $\phi'_{obs}$  having a more dominate role (relative to  $A'_{g,obs}$ ) in the estimation of  $\lambda_{A,\phi}$ . Where there are marked differences between  $\lambda_\phi$  and  $\lambda_{A,\phi}$  (see Table 6.6),  $S_A > S_\phi$ . Those situations occur for the K<sub>1</sub> constituent (in both the  $\lambda_2$ - and  $\lambda_3$ -scenarios) at the location  $0.1a$  (Table 6.6). Trefry and Bekele

(2004) made a contrasting observation in their application of the Townley (1995) straight coastline-based analytical solution to tidal propagation for finite domains (i.e., for the inverse calculation of  $\lambda$ ). That is, they found that  $\lambda$  estimates based on both phase lag and amplitude were closer to  $\lambda$  values obtained from only the amplitude. Sensitivities of  $\lambda$  to changes in amplitude or phase lag were not reported in Trefry and Bekele (2004).

The results in Table 6.6 support the earlier assertion that positive values of  $E_A$  lead to overestimation of  $\lambda_A$  (this is because  $S_A$  is always positive; see Table 6.4), whereas positive values of  $E_\phi$  induce underestimation of  $\lambda_\phi$ . For example, at a distance of  $0.2a$  for the  $M_2$  constituent,  $\lambda_1$ -scenario,  $\lambda_A$  is overestimated (i.e.,  $\lambda_A > 150,000 \text{ m}^2/\text{d}$ ) because  $E_A$  for the same case is positive (i.e., 0.627; Table 6.2). Conversely, for negative values of  $E_A$ ,  $\lambda_A$  is underestimated, as occurs at the  $0.2a$  distance for the  $MK_3$  constituent,  $\lambda_2$ -scenario (i.e.,  $\lambda_A < 350,000 \text{ m}^2/\text{d}$ ; Table 6.6) due to the negative value of  $E_A$  (i.e., -0.301; Table 6.2).

Figure 6.4 compares the error (i.e.,  $|E_T|$ ) in values of  $\lambda_A$ ,  $\lambda_\phi$ ,  $\lambda_{A,\phi}$  and  $\lambda_{av}$ , with respect to the known diffusivities in the three  $\lambda$ -scenarios. The comparison shows the three inland locations (i.e.,  $0.1a$ ,  $0.2a$  and  $0.3a$ ) and the three tidal constituents ( $K_1$ ,  $M_2$  and  $MK_3$ ).

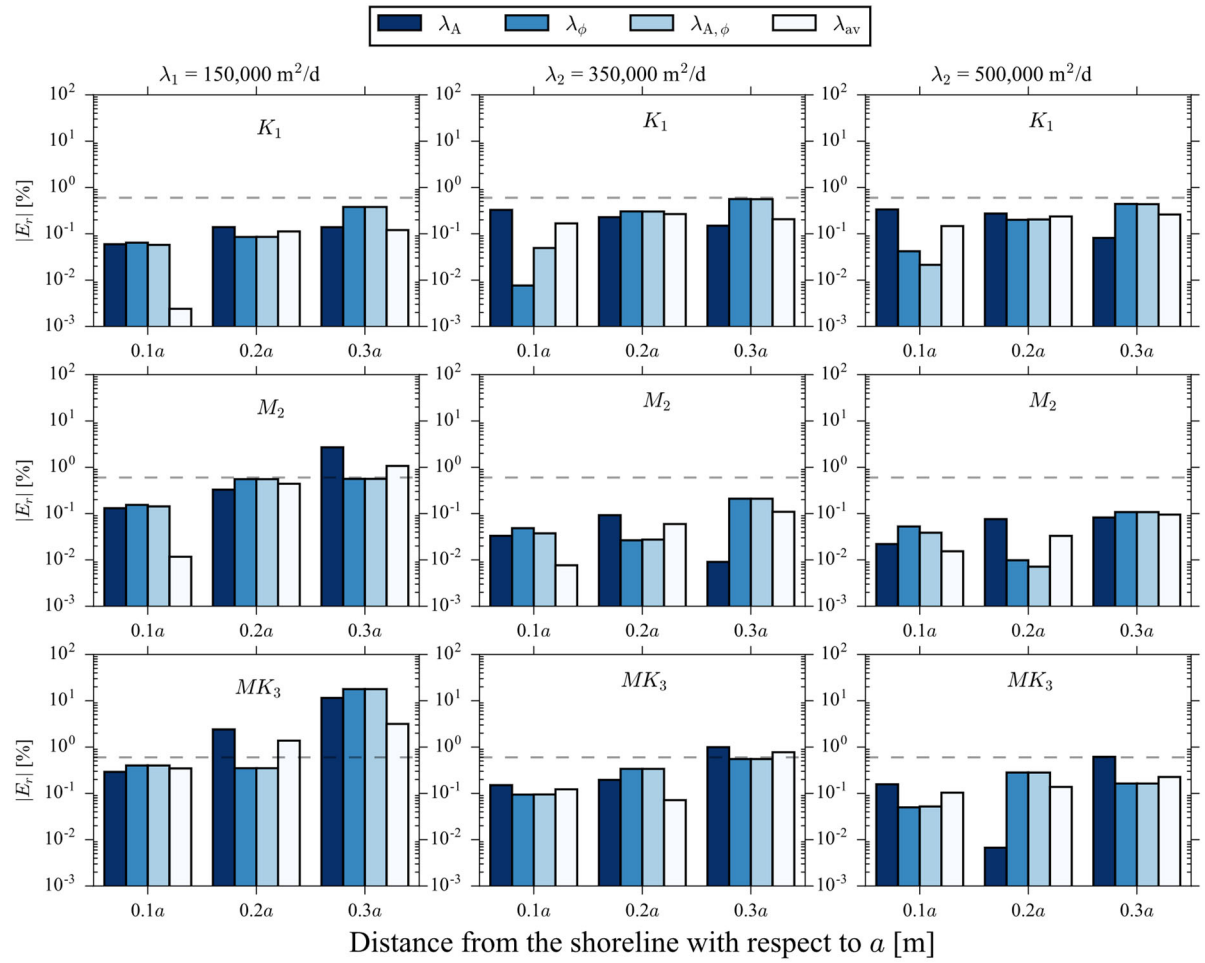


**Figure 6.4** Comparison of  $|E_r|$  for estimated values of  $\lambda_A$ ,  $\lambda_\phi$ ,  $\lambda_{A,\phi}$  and  $\lambda_{av}$  for the three  $\lambda$ -scenarios, derived from the theoretical observations with noise and applying the circular solution. Grey dashed line represents  $|E_r| = 0.6\%$ .

Figure 6.4 shows that in most cases  $|E_r| < 0.6\%$ . Cases where  $|E_r|$  values are  $\geq 0.6\%$  correspond to situations leading to observed amplitudes from harmonic analysis of theoretical observations with noise (i.e.,  $A'_{g,obs}$ ) smaller than 2.5 cm (i.e., within limits of measurement techniques; see Table 6.2). Therefore, we consider cases with  $|E_r| \geq 0.6\%$  inconsequential. Also, the high error of  $|E_r| \approx 18\%$  in the estimate of  $\lambda_\phi$  at the  $0.3a$  distance for the  $MK_3$  constituent,  $\lambda_1$ -scenario is related to the observed phase lag greater than one tidal cycle ( $\varphi'_{obs}$  value with asterisk in Table 6.2). The reason for this is that the associated groundwater amplitude is very small (i.e.,  $A'_{g,obs} = 3 \text{ mm}$ ; Table 6.2). Therefore, based only on relevant data (i.e.,  $A'_{g,obs} \geq 2.5 \text{ cm}$ ), the circular solution reproduces the known diffusivities within 0.6% error.

### 6.4.3.2 Circular solution for unconfined conditions

Figure 6.5 compares the  $|E_r|$  values in  $\lambda_A$ ,  $\lambda_\phi$ ,  $\lambda_{A,\phi}$  and  $\lambda_{av}$  estimates based on a low-frequency tidal constituent (i.e.,  $K_1$ ) under unconfined conditions at the three  $\lambda$ -scenarios and at the inland locations of  $0.1a$ ,  $0.2a$  and  $0.3a$ . Figure 6.5 presents the results derived from numerical observations (left column) and numerical observations with noise (right column). The  $\lambda$  estimates used to determine  $|E_r|$  are presented in Table A2 in Appendix A.

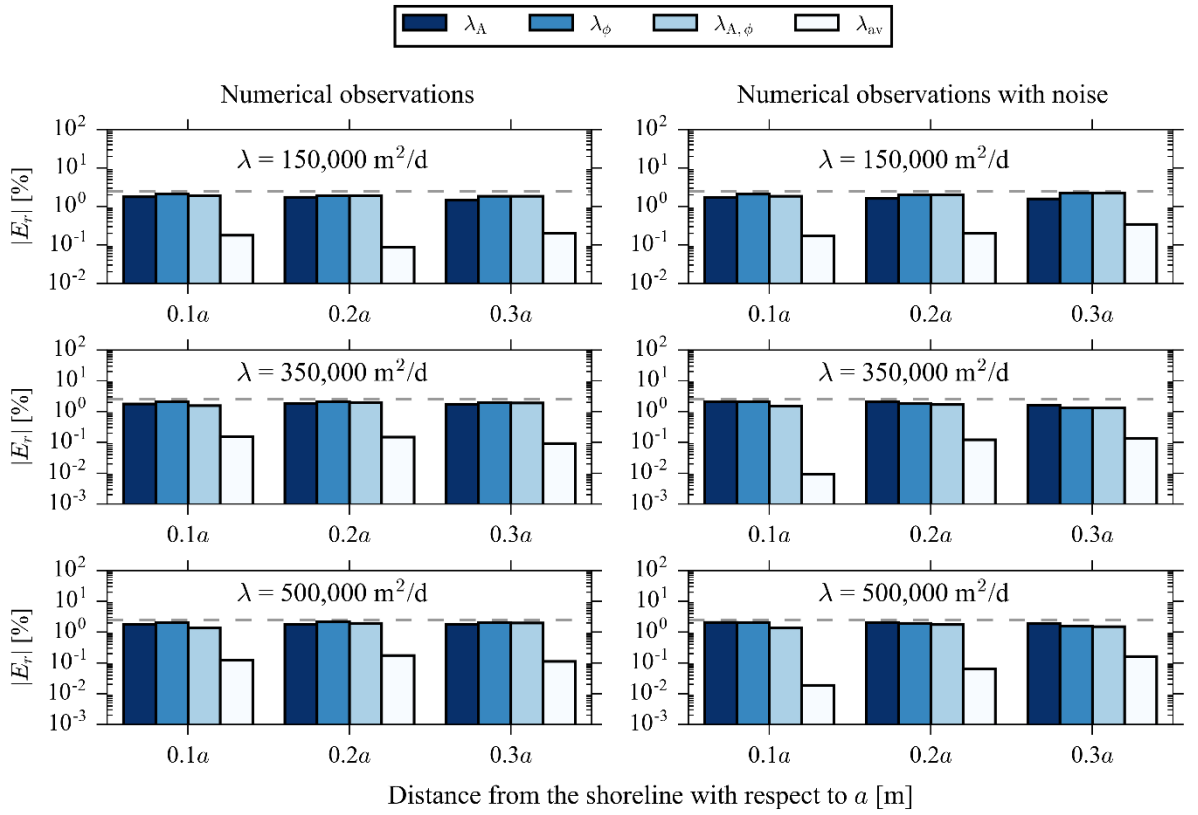


**Figure 6.5** Comparison of  $|E_r|$  for estimated values of  $\lambda_A$ ,  $\lambda_\phi$ ,  $\lambda_{A,\phi}$  and  $\lambda_{av}$  for the  $K_1$  constituent, three  $\lambda$ -scenarios, derived from the numerical observations (left column) and numerical observations with noise (right column) and applying the circular solution. Grey dashed line represents  $|E_r| = 2.5\%$ .

The results in Figure 6.5 show that the maximum  $|E_r|$  in the estimation of  $\lambda$  using both numerical observations, with and without noise, at the three  $\lambda$ -scenarios is 2.2% (ignoring the  $|E_r|$  values derived from the  $A_{n,obs}$  and  $A'_{n,obs}$  values smaller than 2.5 cm in Tables 6.3 and A8).  $|E_r|$  values for unconfined cases (average  $|E_r|$  of 1.8% for estimated values of  $\lambda_A$ ,  $\lambda_\phi$ , and  $\lambda_{A,\phi}$ ; Figure 6.5)

are higher than those for confined cases (average  $|E_r|$  of 0.86% for estimated values of  $\lambda_A$ ,  $\lambda_\phi$ , and  $\lambda_{A,\phi}$ ; Figure 6.4). This difference in  $|E_r|$  values is consistent with the difference in  $|E_A|$  and  $|E_\phi|$  values between confined and unconfined conditions. That is, the obtained  $|E_A|$  and  $|E_\phi|$  values for unconfined conditions (i.e., Tables 6.3 and A8) are significantly higher (i.e., average  $|E_A|$  of 1.8% and average  $|E_\phi|$  of 0.97%; including numerical observations with and without noise) than those obtained for confined conditions based on theoretical observations with noise (i.e., average  $|E_A|$  of 0.15% and average  $|E_\phi|$  of 0.1%; Table 6.2).

A comparison between the  $E_r$  values derived from numerical observations and those derived from numerical observations with noise shows that all approaches to  $\lambda$  estimation (i.e.,  $\lambda_A$ ,  $\lambda_\phi$ ,  $\lambda_{A,\phi}$  and  $\lambda_{av}$ ), produce the same range of values, regardless of whether noise is imposed or not. This outcome is consistent with the harmonic analysis results observed in Tables 6.3 and A8, where amplitudes and phase lags from numerical observations ( $A_{n,obs}$ ,  $\phi_{n,obs}$ ) and from numerical observations with noise ( $A'_{n,obs}$ ,  $\phi'_{n,obs}$ ) are within the same value range. That is,  $E_A$  values in Table 6.3 (i.e., unconfined conditions without noise) are similar to  $E_A$  values in Table A8 (i.e., unconfined conditions with noise). The same finding applies to the results of  $E_\phi$  in Tables 6.3 and A8.

Figure 6.4 shows that the best approach to estimate  $\lambda$  under unconfined conditions applying the circular solution on observations with and without noise is the average approach (i.e.,  $\lambda_{av}$ ; lightest-coloured bars). This is because  $\lambda_A$  is underestimated and  $\lambda_\phi$  is overestimated in all cases (see Table A2 in Appendix A), causing the average approach to be closer to the known value. This differs from the results obtained for the confined conditions (applying the circular solution), for which no consistent error trend was observed that would allow for the recommendation of a specific approach (i.e.,  $\lambda_A$ ,  $\lambda_\phi$ ,  $\lambda_{A,\phi}$  or  $\lambda_{av}$ ; see Section 6.4.3.1).

#### 6.4.4 $\lambda$ estimation applying the Solórzano-Rivas and Werner (2020) correction factor

The aquifer characteristics (i.e., island size and  $\lambda$ -scenarios) and observation distances from the shoreline used in this study lead to conditions that satisfied the requirements of  $|\gamma r| \geq 2$  and  $|\gamma a| \geq 2$  to apply the correction factor to the Ferris solution (e.g., Solórzano-Rivas and Werner, 2020). For example, the lowest value of  $|\gamma r|$  was 7.5 and occurred at the penetration distance of  $0.2a$  for the  $K_1$  constituent,  $\lambda_3$ -scenario. The lowest value of  $|\gamma a|$  was 10.7 and was constant at the three locations for the  $K_1$  constituent,  $\lambda_3$ -scenario. An evaluation of the correction factor to the Ferris solution was undertaken for both confined and unconfined aquifer conditions.

##### 6.4.4.1 *Application of the corrected Ferris solution for confined conditions*

Figure 6.6 compares the  $|E_r|$  for the different  $\lambda$  estimation approaches ( $\lambda_{AF}$ ,  $\lambda_{\phi F}$  and  $\lambda_{avF}$ ) in the three  $\lambda$ -scenarios applying the corrected Ferris solution in confined conditions. Results are derived from theoretical observations (i.e., without noise). The comparison shows  $|E_r|$  values for the three inland locations (i.e.,  $0.1a$ ,  $0.2a$  and  $0.3a$ ) and the three tidal constituents ( $K_1$ ,  $M_2$  and  $MK_3$ ). The  $\lambda$  estimates used to determine  $|E_r|$  are presented in Tables A3 to A5 in Appendix A.

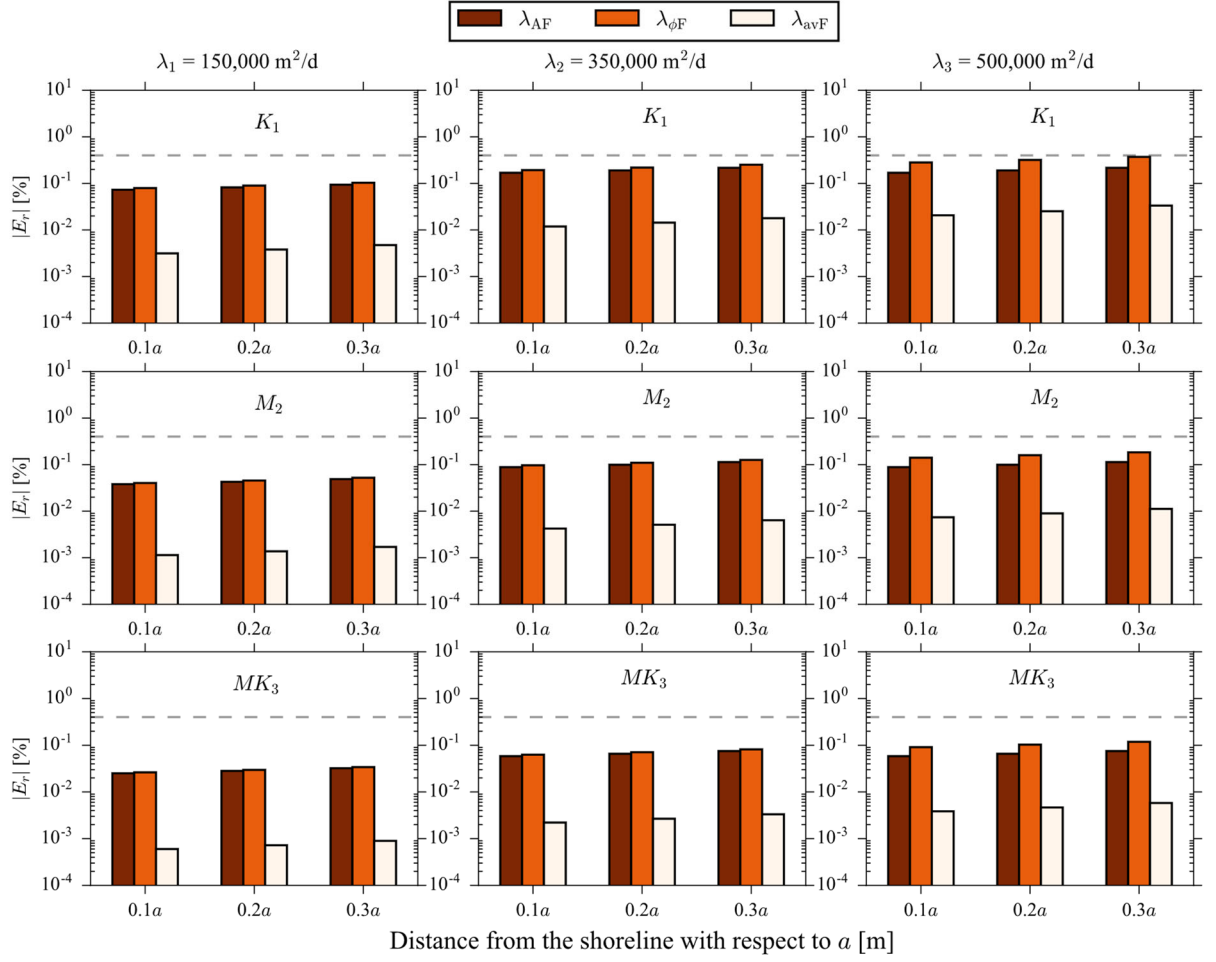


**Figure 6.6** Comparison of  $|E_r|$  for estimated values of  $\lambda_{AF}$ ,  $\lambda_{\phi F}$  and  $\lambda_{avF}$  for the three  $\lambda$ -scenarios, derived from theoretical observations (i.e., without noise) and applying the corrected Ferris solution. Grey dashed line represents  $|E_r| = 0.4\%$ .

Results in Figure 6.6 show that the corrected Ferris solution was able to reproduce the known diffusivities in all scenarios within 99.6% accuracy (i.e., maximum  $|E_r|$  is 0.37%), when the estimates are based on theoretical observations (i.e., without noise). Figure 6.6 shows a direct relationship between  $|E_r|$  and tidal period (i.e., estimates from larger period constituents, e.g.,  $K_1$ , involve larger errors) and  $\lambda$  (i.e., errors increase with increasing  $\lambda$ , i.e., from  $\lambda_1$ -scenario to  $\lambda_3$ -scenario). It is also evident that  $\lambda_{avF}$  produced the smallest  $|E_r|$  values (i.e., within 0.03%; lightest-coloured bars in Figure 6.6). The reason for this is that  $\lambda_{AF}$  overestimates the known diffusivities (positive  $E_r$  values in Tables A3-A5), whereas these are underestimated by  $\lambda_{\phi F}$  (negative  $E_r$  values in Tables A3-A5). This is similar to over- and under-estimation of  $\lambda$  for the unconfined conditions applying the circular solution (i.e., Section 6.4.3.2), leading to the lower errors occurring in  $\lambda_{av}$ .

Figure 6.7 present similar results to those given in Figure 6.6, except theoretical observations with noise are used in estimating  $\lambda$ .

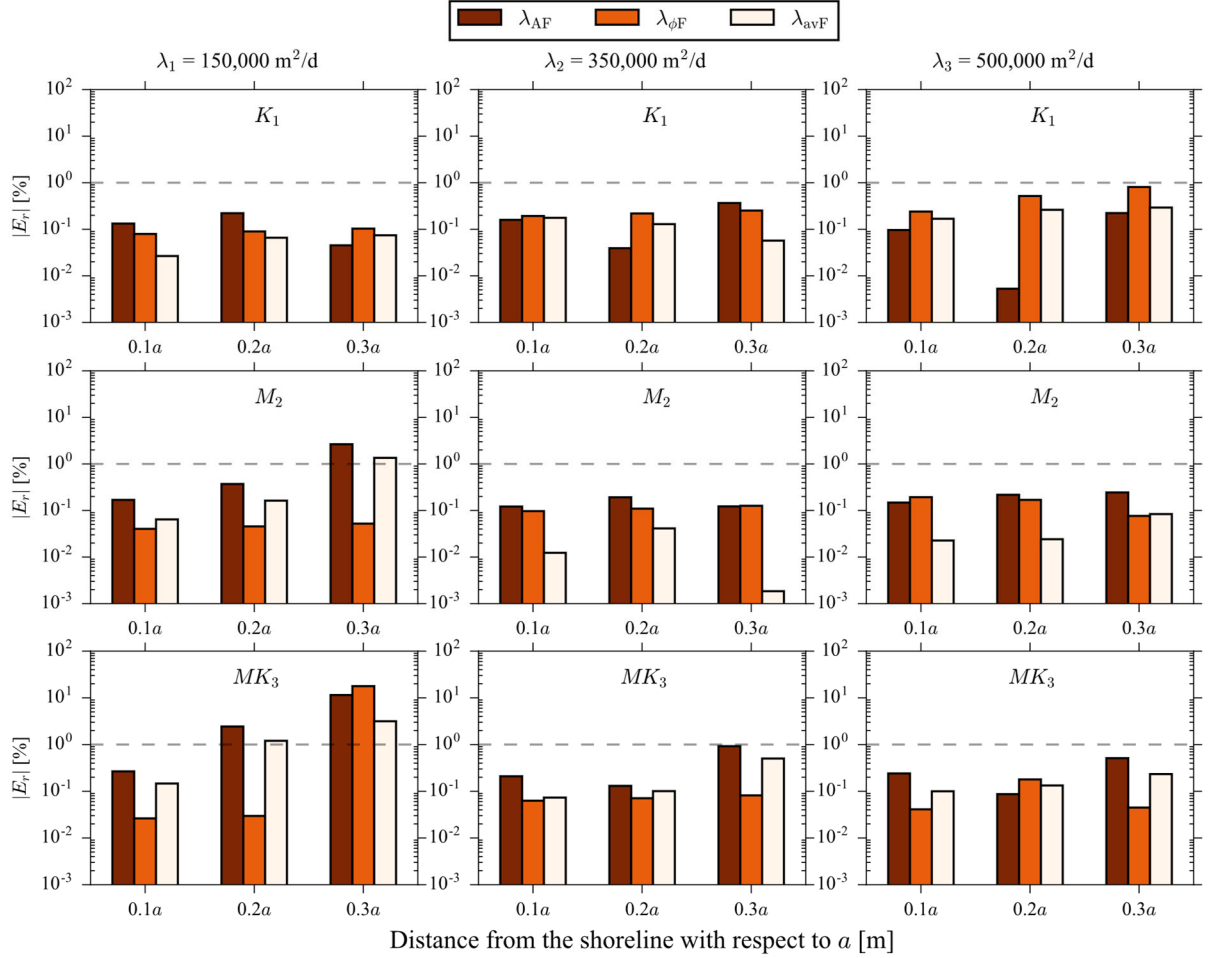


**Figure 6.7** Comparison of  $|E_r|$  for estimated values of  $\lambda_{AF}$ ,  $\lambda_{\phi F}$ , and  $\lambda_{avF}$  for the three  $\lambda$ -scenarios, derived from theoretical observations with noise and applying the corrected Ferris solution. Grey dashed line represents  $|E_r| = 1\%$ .

Figure 6.7 shows that the corrected Ferris solution reproduced the known diffusivities within 1% error (i.e., maximum  $|E_r|$  is 0.81%, ignoring cases where amplitudes are smaller than 2.5 cm; values denoted with “†” in Table 6.2). The only case where  $|E_r|$  for the estimated values of  $\lambda_{\phi F}$  (i.e., orange bars in Figure 6.7) exceeds 1% (i.e.,  $|E_r| \approx 18\%$ , at the  $0.3a$  distance for the  $MK_3$  constituent,  $\lambda_1$ -scenario) is associated with the situation where the phase lag is greater than one tidal cycle (i.e.,  $\phi'_{\text{obs}}$  value with asterisk in Table 6.2). Note that this large  $|E_r|$  value is also

associated with the corresponding small groundwater amplitude (i.e.,  $A'_{g,obs} = 3$  mm; Table 6.2). This is a similar result (i.e.,  $|E_r| \approx 18\%$ ) obtained for the same case applying the circular solution (i.e., Section 6.4.3.1). Figure 6.7 shows that  $\lambda_{avF}$  values applying the corrected Ferris solution were not the most accurate when based on theoretical observations with noise, contrary to diffusivity estimates from theoretical observations. This is because  $\lambda_{AF}$  or  $\lambda_{\phi F}$  based on theoretical observations with noise does not consistently overestimate or underestimate the known diffusivities as occurs with estimates derived from theoretical observations (see Tables A3-A5 in Appendix A).

We explored the errors obtained in  $\lambda$  estimates by the direct application of the Ferris solution (without the correction factor) to the three  $\lambda$ -scenarios under confined conditions, and with the  $K_1$  constituent only. The results show that the direct application of the Ferris solution (without the correction factor) led to higher  $|E_r|$  values than those obtained from application of the corrected Ferris solution, with errors in  $\lambda_{AF}$  and  $\lambda_{avF}$  estimates of up to 18% and 9%, respectively (see results in Table A7).

Optimization results provided estimates of island radii that lead to comparable groundwater amplitudes (i.e., within 1% of the radial solution) when applying the Ferris solution (without correction). The  $M_2$ -constituent,  $\lambda_2$ -scenario was adopted. The analysis showed that 1% errors were obtained at inland distances of 300 m, 600 m and 900 m when the island radius was approximately 15 km, 30 km and 45 km, respectively. In other words, to limit the error in the Ferris solution to 1% (in applying it to a circular island) at a measurement point at 300 m from the shoreline, the island radius should be larger than 15 km (i.e., the radial solution is needed for island radii less than 15 km). These results further indicate that the minimum island size to achieve a 1% error in applying the Ferris solution (without correction) to tidal propagation in orbiculate boundaries depends on the measurement location, in agreement with Solórzano-Rivas and Werner (2020). For the conditions studied (i.e.,  $M_2$ -constituent,  $\lambda_2$ -scenario), minimum island radii to achieve  $<1\%$  error were about 50-times the distance from the shoreline that tidal conditions were estimated. Noting that the limit of amplitude measurability (i.e., approximately 2.5cm), amplitude in the  $MK_3$ -constituent,  $\lambda_2$ -scenario at the  $0.2a$  inland distance (i.e., 600 m) is  $\approx 0.03$  m (Table 2), it follows that islands up 30 km may require application of the circular solution method to limit errors (due to the curved nature of the shoreline) to 1%.

#### 6.4.4.2 Application of the corrected Ferris solution for unconfined conditions

Figure 6.8 compares  $|E_r|$  for the different  $\lambda$  estimation approaches ( $\lambda_{AF}$ ,  $\lambda_{\phi F}$  and  $\lambda_{avF}$ ) applying the corrected Ferris solution in unconfined conditions based on both numerical observations and numerical observations with noise. The  $\lambda$  estimates used to determine  $|E_r|$  are presented in Table A6 in Appendix A.

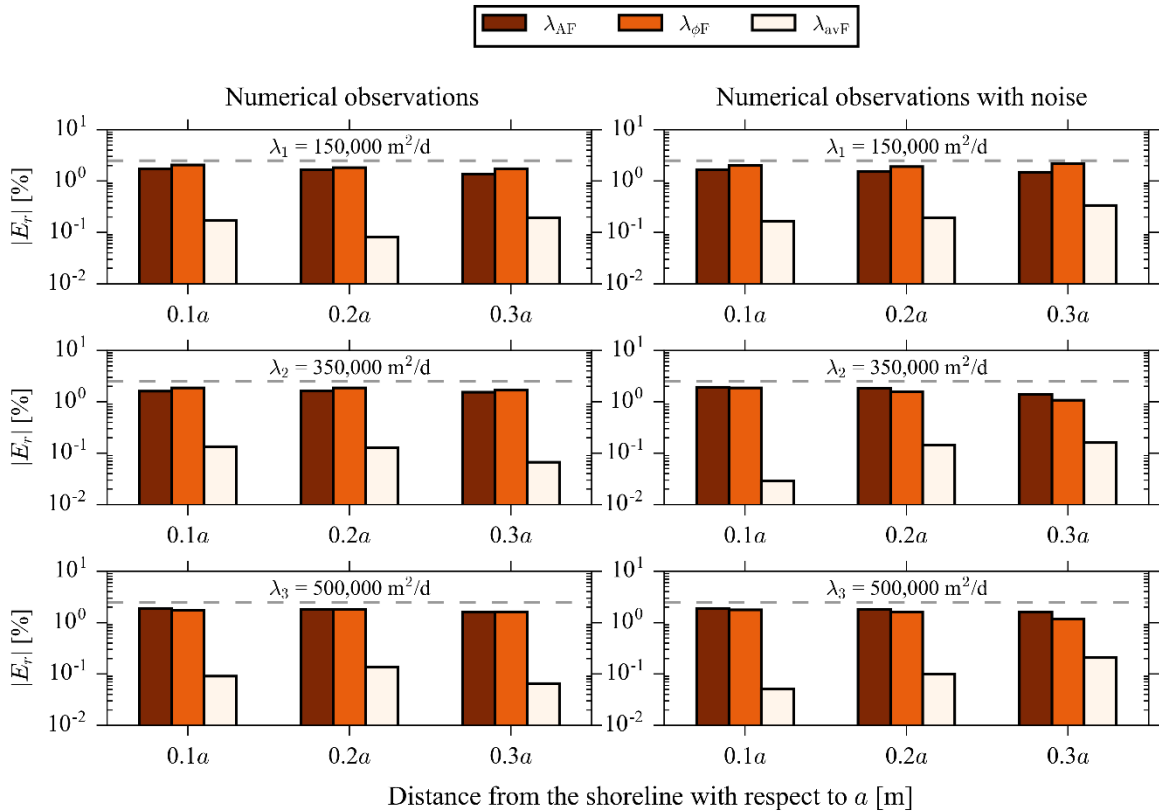


**Figure 6.8** Comparison of  $|E_r|$  for estimated values of  $\lambda_{AF}$ ,  $\lambda_{\phi F}$ , and  $\lambda_{avF}$  for the three  $\lambda$ -scenarios, derived from numerical observations and numerical observations with noise, applying the corrected Ferris solution. Grey dashed line represents  $|E_r| = 2.5\%$ .

Results in Figure 6.8 show that the maximum value of  $|E_r|$  is within 2.5% of the known value when the corrected Ferris solution is adopted to estimate  $\lambda$  in unconfined aquifer conditions, regardless of whether noise is imposed or not. A similar result was obtained (i.e., up to 2.5% error) with the estimation of  $\lambda$  applying the circular solution for unconfined conditions. These results show that both the corrected Ferris solution and circular solution provide similar ranges of errors in the estimation of  $\lambda$ ; including the same tendency of underestimating and

overestimating  $\lambda_{AF}$  and  $\lambda_{\phi F}$ , respectively (see Table A6). The under/overestimation of  $\lambda_{AF}$  and  $\lambda_{\phi F}$  is why the ideal method to estimate  $\lambda$  under unconfined conditions applying the corrected Ferris solution is the  $\lambda_{avF}$  approach (i.e., lightest-coloured bars; Figure 6.8), which uses an average of  $\lambda_{AF}$  and  $\lambda_{\phi F}$  and thereby under/overestimations are offset. The average approach is also the ideal approach in applying the circular solution to unconfined conditions, for the same reason.

## 6.5 Conclusions

The application of the circular solution for the estimation of aquifer diffusivity has been assessed for the first time. Given the functions that describe the circular solution, the inverse problem of estimating aquifer diffusivity (i.e.,  $\lambda$ ) requires the application of iterative methods.

The results of this study suggest that application of the circular and corrected Ferris solutions to the estimation of  $\lambda$  led to relative errors (i.e.,  $|E_r|$ )  $< 1\%$  and  $< 2.5\%$  for confined and unconfined conditions, respectively, even where noise was added to synthetic hydrographs. An exception arose in estimating  $\lambda$  based on phase lags corresponding to more than one tidal cycle, led to high relative errors in  $\lambda$  estimates (i.e., up to 18%). This applied to both the circular solution and the corrected Ferris solution. For the cases considered, large values of phase lags (i.e.,  $>$  one tidal cycle) occurred when the amplitude was smaller than the assumed limit of measurement techniques (i.e., 2.5 cm). Thus, it is unlikely that this error will be encountered in practical, field conditions, but nevertheless, we recommend not applying the circular solution or corrected Ferris solution to estimate  $\lambda$  where phase lags  $> 2\pi$  or amplitudes  $< 2.5$  cm.

The average approach (i.e.,  $\lambda$  is the mean of values obtained from the amplitude decay and phase lag) was found to be the most accurate technique to estimate  $\lambda$  applying the circular solution and the corrected Ferris solution for unconfined conditions, even when noise was imposed to the signal. The average approach was also the best technique to estimate  $\lambda$  from the corrected Ferris solution, at least under confined conditions and without noise added to the signal. There were no other cases where a specific approach consistently led to values of  $\lambda$  (from tidal analysis) closer to the known  $\lambda$ .

The use of different tidal periods (i.e., different ocean-tide constituents) did not show any influence in the estimation of  $\lambda$ , except when the corrected Ferris solution was applied to signals without noise (for confined conditions). In that case, a direct relationship between  $|E_r|$  and tidal period (i.e., estimates from larger period constituents, e.g.,  $K_1$ , involved larger errors) was observed.

The results presented here suggest that the minimum island size to achieve a 1% error in applying the Ferris solution (without correction) to tidal propagation from orbiculate boundaries depends on the measurement location. For the conditions studied (i.e.,  $M_2$ -constituent,  $\lambda_2$ -scenario), the minimum island radii to achieve  $<1\%$  error should be about 50-times the distance from the shoreline where tidal conditions are estimated. Thus, as a general rule, the circular solution and the corrected Ferris solution are the best approaches to estimate aquifer diffusivity in circular islands of radii less than several 10s of kilometres.

The methodologies proposed in this study extend the available tools to estimate aquifer parameters, especially in circular aquifers, facilitating the determination of properties that otherwise require more invasive methods such as pumping tests. This is particularly advantageous for the evaluation of the aquifer properties of small islands, given the ease with which tidal data can be obtained.

## Chapter 7      Conclusions

### 7.1      Summary of findings

The four studies contained in this thesis investigated three typical complex processes associated with coastal aquifers: (1) dispersion effects on submarine aquifers; (2) application of buoyancy theory to seafloor sediments; (3) application of analytical solutions to tidal propagation in circular islands. The main obtained conclusions are summarised in this chapter.

- (1) The effects of dispersion on the studied hydrogeological processes associated with offshore aquifers are interdependent with other features of the system that make the anticipation of those effects difficult. While the interface toe (i.e., where the interface intercepts the bottom of the aquifer) is located further offshore with increasing dispersion as it occurs with onshore aquifers; the relationship between dispersion and the interface tip location (i.e., where the interface intercepts the top of the aquifer) is more complex. Such complexity is associated with the integrated effect of dispersion with the hydraulic properties of the upper boundary layer of the aquifer, formed by low-permeability sediments (i.e., submarine aquitard) in direct contact with the ocean.

We found that the hydraulic conductivity ratio between the overlying aquitard and submarine aquifer plays an important role in the response of the interface tip location to dispersion. As the hydraulic conductivity ratio between aquitard and aquifer increases, the relationship between the interface tip location and dispersion becomes non-monotonic. That is, the interface tip location changes from being further offshore with increasing dispersion to be located closer to the shoreline as dispersion increases when the hydraulic conductivity ratio between aquitard and aquifer also increases.

The effects of dispersion on the interface width in offshore aquifers differ between the top and bottom of the aquifer. At the bottom, the effects of dispersion on the interface width are similar to those observed in at the bottom of onshore aquifers, where the interface width increases with upscaling dispersion. At the top, a non-monotonic relationship is observed between the interface width and increasing dispersion because of the dependence on the

aquitard-aquifer hydraulic conductivity ratio, as it occurs with the location of the interface tip.

The other hydrogeological process affected by dispersion in offshore aquifers is the submarine groundwater discharge to the ocean. This submarine groundwater discharge is formed by land-derived fresh groundwater and seawater circulation (i.e., estimated from numerical modelling results as the total seawater discharge back to the seafloor). Both, the submarine fresh groundwater discharge and the seawater circulation rates increase with increasing dispersion. This outcome indicates that aquifer heterogeneity (i.e., considering dispersion as a surrogate of heterogeneity in numerical modelling) leads to a larger submarine fresh and saline groundwater discharge, which has implications in the ecology of seafloor sediments due to the exchange of nutrients and dissolved substances caused by the flow dynamics associated with submarine groundwater discharge.

Our attempts to find a correction factor to the sharp-interface based Werner and Robinson (2018) analytical solution to account for dispersion were unsuccessful. The reason for this is the complex relationship between dispersion and aquitard hydraulic properties, and whether the interface toe is located onshore or offshore (i.e., analytical model cases adopted by the Werner and Robinson (2020) analytical solution).

- (2) The submarine fresh groundwater discharge distribution through high-permeability sediments in direct contact with the ocean is associated with mixed-convective processes in the form of buoyant freshwater fingers. These flow instabilities involved in mixed-convective processes make the freshwater distribution in submarine high-permeability sediments temporal and spatially variable. Such instability has implications in the measurement of submarine fresh groundwater discharge given its dependence on the location of measurement devices and duration of the monitoring process, especially when that measurement is undertaken through the deployment of seepage meters on the seafloor.

We found that the temporal conditions of the unstable flow in the form of buoyant freshwater fingers, are controlled by the lower boundary. While the flow restriction caused by a low-permeability layer at the lower boundary of the seafloor sediments cause unstable

flow conditions, no restriction to flow at the lower boundary cause temporal freshwater fingers until the system is rendered completely fresh. Hence, critical Rayleigh numbers to determine whether unstable flow conditions govern the flow distribution within high-permeability seafloor sediments is warranted.

- (3) Tidal propagation in orbiculate islands can be estimated through an existing circular solution based on radial groundwater flow, or through the corrected Ferris solution we have proposed in this thesis. Both approaches, the circular and the corrected Ferris solutions, to tidal propagation have shown to be reliable for the inverse estimation of aquifer diffusivities (i.e., within 1% and 2.5% error, respectively).

Our results indicate that the minimum island size to achieve a 1% error in applying the Ferris solution (without correction) to tidal propagation in orbiculate boundaries depends on the measurement location. For the conditions analysed in this thesis, the minimum island radii to achieve <1% error were about 50-times the distance from the shoreline that tidal conditions were estimated. Thus, as a general rule, the circular solution and the corrected Ferris solution are the best approaches to estimate aquifer diffusivity in circular islands of radii less than several 10s of kilometres.

## **7.2 Future work**

- (1) Finding an individual correction factor to account for dispersion in the Werner and Robinson (2018) analytical solution to offshore freshwater extent would be of interest: the controlling factors in the location of the dispersive toe differ from those governing the tip location. That is, the upper boundary (i.e., submarine aquitard) has a major influence on the tip location, whereas the toe is less sensitive to the characteristics of this upper boundary. Therefore, an individual factor (for the top and tip) to correct for dispersion the Werner and Robinson (2018) analytical solution is needed. Additionally, the type of analytical case (i.e., the Werner and Robinson (2018) analytical solution adopts four analytical cases) may also be considered when ascertaining a correction factor to dispersion.

- (2) This study has demonstrated that non-dimensional numbers widely applied to the characterisation and prediction of downward solute movement (e.g., Rayleigh number and the mixed convection ratio) can potentially be applied with the same purpose to the occurrence of submarine fresh groundwater discharge through high-permeability seafloor sediments. Therefore, further systematic analysis is needed to obtain a critical Rayleigh number or critical boundary Rayleigh number to help ascertain the occurrence of fresh groundwater discharge in the form of buoyant freshwater fingers through seafloor sediments.
- (3) An improvement on the current understanding of tidal propagation processes in coastal aquifer is needed. This thesis has demonstrated the influence of an orbiculate boundary on the estimation of aquifer properties by comparing it with a straight-based solution. Therefore, additional complex shoreline shapes could be analysed to study their influence on the tidal processes in coastal aquifers.

## Bibliography

Abarca, E., Carrera, J., Sánchez-Vila, X., Dentz, M. (2007). Anisotropic dispersive Henry problem. *Advances in Water Resources*, 30(4), 913-926, doi: 10.1016/j.advwatres.2006.08.005.

Abramowitz, M. and Stegun, I. A. (1965). Handbook of mathematical functions, with formulas, graphs, and mathematical tables. Dover Publications, New York.

Badaruddin, S., Werner, A. D., Morgan, L. K. (2017). Characteristics of active seawater intrusion. *Journal of Hydrology*, 551, 632-647, doi:10.1016/j.jhydrol.2017.04.031.

Bakker, M. (2006). Analytic solutions for interface flow in combined confined and semi-confined, coastal aquifers. *Advances in Water Resources*, 29(3), 417-425, doi: 10.1016/j.advwatres.2005.05.009.

Bakker, M., Miller, A. D., Morgan, L. K., Werner, A. D. (2017). Evaluation of analytic solutions for steady interface flow where the aquifer extends below the sea. *Journal of Hydrology*, 551, 660-664, doi: 10.1016/j.jhydrol.2017.04.009.

Banerjee, P., Sarwade, D., Singh, V. S. (2008). Characterization of an island aquifer from tidal response. *Environmental Geology*, 55(4), 901-906, doi: 10.1007/s00254-007-1041-y.

Bear, J. (1979). Hydraulics of groundwater (McGraw-Hill series in Water Resources and Environmental Engineering). McGraw-Hill International Book, New York.

Bear, J., Cheng, A. H. D. (2010). Modeling groundwater flow and contaminant transport (Vol. 23). Springer Science and Business Media.

Bear, J., Cheng, A. H. D., Sorek, S., Ouazar, D., Herrera, I. (1999). Seawater intrusion in coastal aquifers: concepts, methods and practices. Springer Science and Business Media, doi: 10.1007/978-94-017-2969-7.

Bloomfield, P. (1976). *Fourier Analysis of Time Series: An Introduction*. John Wiley and Sons, New York.

Bruggeman, G. A. (1999). *Analytical Solutions of Geohydrological Problems. Developments in Water Science*, 46. Elsevier, Amsterdam.

Burnett, W. C., Aggarwal, P. K., Aureli, A., Bokuniewicz, H., Cable, J. E., Charette, M. A., Kontar, E., Krupa, S., Kulkarni, K. M., Loveless, A., Moore, W. S., Oberdorfer, J. A., Oliveira, J., Ozyurt, N., Povinec, P., Privitera, A. M. G., Rajar, R., Ramessur, R. T., Scholten, J., Stieglitz, T., Taniguchi, M., Turner, J. V. (2006). Quantifying submarine groundwater discharge in the coastal zone via multiple methods. *Science of the Total Environment*, 367(2-3), 498-543. doi:10.1016/j.scitotenv.2006.05.009.

Cabrera, M. C., Custodio, E. (2004). Groundwater flow in a volcanic-sedimentary coastal aquifer: Telde area, Gran Canaria, Canary Islands, Spain. *Hydrogeology Journal*, 12(3), 305-320, doi: 10.1007/s10040-003-0316-y.

Carr, P. A., van der Kamp, G. S. (1969). Determining aquifer characteristics by the tidal method. *Water Resources Research*, 5(5), 1023-1031, doi: 10.1029/WR005i005p01023.

Carslaw, H., Jaeger, J. C. (1959). *Conduction of heat in solids*. Second Edition. Oxford University Press, Inc., New York.

Chattopadhyay, P. B., Vedanti, N., Singh, V. S. (2014). A conceptual numerical model to simulate aquifer parameters. *Water Resources Management*, 29(3), 771-784, doi: 10.1007/s11269-014-0841-6.

Chuang, M., Yeh, H. (2007). An analytical solution for the head distribution in a tidal leaky confined aquifer extending an infinite distance under the sea. *Advances in Water Resources*, 30(3), 439-445, doi: 10.1016/j.advwatres.2006.05.011.

- Cooper, H. H., Jr. (1959). A hypothesis concerning the dynamic balance of fresh water and salt water in a coastal aquifer. *Journal of Geophysical Research*, 64(4), 461-467.
- Custodio, E., Bruggeman, G. A. (1987). Groundwater problems in coastal areas. Studies and reports in hydrology (UNESCO).
- Depner, J. S., Rasmussen, T. C. (2016). Hydrodynamics of time-periodic flows: Diffusion waves in porous media. AGU Geophysical Monograph 224, Wiley.
- Doodson, A. T. (1954). The harmonic development of the tide generating potential. *International Hydrographic Review*, 31(1), 37-61.
- Elder, J. W., Simmons, C. T., Diersch, H., Frolkovič, P., Holzbecher, E., Johannsen, K. (2017). The Elder Problem. *Fluids*, 2(1), p. 11. doi: 10.3390/fluids2010011.
- Erskine, A. D. (1991). The effect of tidal fluctuation on a coastal aquifer in the UK. *Groundwater*, 29(4), 556-562, doi:10.1111/j.1745-6584.1991.tb00547.x.
- Essaid, H. I. (1986). A comparison of the coupled fresh water-salt water flow and the Ghyben-Herzberg sharp interface approaches to modeling of transient behavior in coastal aquifer systems. *Journal of Hydrology*, 86(1-2), 169-193, doi: 10.1016/0022-1694(86)90012-0.
- Ferris, J. G. (1951). Cyclic fluctuations of water level as a basis for determining aquifer transmissibility: Note 1. U.S. Geological Survey, Water Resources Division, Washington.
- Frind, E. O. (1982). Seawater intrusion in continuous coastal aquifer-aquitard systems. *Advances in Water Resources*, 5 (2), 89-97, doi: 10.1016/0309-1708(82)90050-1.
- Gallagher, B. S., Munk, W. H. (1971). Tides in shallow water: Spectroscopy. *Tellus*, 23(4-5), 346-363.

Gelhar, L. W., Welty, C., Rehfeldt, K. R. (1992). A critical review of data on field-scale dispersion in aquifers. *Water Resources Research*, 28(7), 1955-1974.

Godin, G. (1972). The analysis of tides. Liverpool University Press, Liverpool.

Guo, W., Langevin, C. D. (2002). User's Guide to SEAWAT: A Computer Program for the Simulation of Three-Dimensional Variable-Density Ground-Water Flow: Techniques of Water-Resources Investigations of the U. S. Geological Survey. Book 6, Chapter A7, Open File, 01-434, p. 77., Tallahassee, Florida.

Guo, H., Jiao, J. J. and Li, H. (2010). Groundwater response to tidal fluctuation in a two-zone aquifer. *Journal of Hydrology*, 381(3-4), 364-371, doi: 10.1016/j.jhydrol.2009.12.009.

Harbaugh, A. W., Banta, E. R., Hill, M. C., McDonald, M. G. (2000). MODFLOW-2000, the U. S. Geological Survey Modular Ground-Water Model - User guide to modularization concepts and the ground-water flow process, U. S. Geological Survey, Open File, 00-92, 121 pp., Reston, Virginia.

Heiss, J. W., Michael, H. A. (2014). Saltwater-freshwater mixing dynamics in a sandy beach aquifer over tidal, spring-neap, and seasonal cycles. *Water Resources Research*, 50(8), 6747-6766, doi:10.1002/2014WR015574.

Hill, M. C. (1988). A Comparison Of Coupled Freshwater-Saltwater Sharp-Interface And Convective-Dispersive Models Of Saltwater Intrusion in a Layered Aquifer System. *Computational Methods in Water Resources*, 1, Proc. 7th conference, Cambridge, MA, 1988, 211-216.

Huyakorn, P. S., Andersen, P. F., Mercer, J. W., White, H. O. (1987). Saltwater intrusion in aquifers: development and testing of a three-dimensional finite element model. *Water Resources Research*, 23 (2), 293–312, doi: 10.1029/WR023i002p00293.

Ingersoll, L. R., Zobel, O. J. and Ingersoll, A. C. (1948). Heat Conduction, With Engineering and Geological Applications. McGraw – Hill Co., Inc., New York.

In-Situ Inc. (2017). Rugged TROLL 100 Data Logger, < [https://in-situ.com/wp-content/uploads/2014/11/SS\\_RuggedTROLL\\_100\\_200\\_Dec2017.pdf](https://in-situ.com/wp-content/uploads/2014/11/SS_RuggedTROLL_100_200_Dec2017.pdf)>, viewed 20 March 2019.

In-Situ Inc., 2020. Level TROLL 400, 500 & 700 Data Loggers, <[https://in-situ.com/pub/media/support/documents/LevelTROLL\\_SS.pdf](https://in-situ.com/pub/media/support/documents/LevelTROLL_SS.pdf)>, viewed 27 April 2020.

Irvine, D. J., Sheldon, H. A., Simmons, C. T., Werner, A. D., Griffiths, C. M. (2015). Investigating the influence of aquifer heterogeneity on the potential for thermal free convection in the Yarragadee Aquifer, Western Australia. *Hydrogeology Journal*, 23(1), 161-173. doi:10.1007/s10040-014-1194-1.

Irvine, D. J., Werner, A. D., Ye, Y., Jazayeri, A. (2021). Upstream dispersion in solute transport models: A simple evaluation and reduction methodology. *Groundwater*, 59(2), 287-291. doi:10.1111/gwat.13036.

Jacob, C. E. (1950). Flow of ground water, in *Engineering Hydraulics*, 321-386. John Wiley and Sons, Inc., New York.

Jha, M. K., Kamii, Y., Chikamori, K. (2003). On the estimation of phreatic aquifer parameters by the tidal response technique. *Water Resources Management*, 17(1), 69-88, doi:10.1023/A:1023018107685.

Jiao, J. J., Post, V. E. A. (2019). Coastal hydrogeology (pp. 1-403) doi:10.1017/9781139344142.

Jiao, J. J. and Tang, Z. (1999). An analytical solution of groundwater response to tidal fluctuation in a leaky confined aquifer. *Water Resources Research*, 35(3), 747-751, doi: 10.1029/1998WR900075.

Jiao, J. J., Shi, L., Kuang, X., Lee, C. M., Yim, W. W. S., Yang, S. (2015). Reconstructed chloride concentration profiles below the seabed in Hong Kong (China) and their implications for offshore groundwater resources. *Hydrogeology Journal*. 23 (2), 277–286. doi: 10.1007/s10040-014-1201-6.

Johannes, R. E. (1980). The Ecological Significance of the Submarine Discharge of Groundwater. *Marine Ecology – Progress Series*, 365-373.

Kay, S. M. (1993). Fundamentals of statistical signal processing. Prentice Hall PTR. Upper Saddle River, New Jersey.

Kerrou, J., Renard, P. (2010). A numerical analysis of dimensionality and heterogeneity effects on advective dispersive seawater intrusion processes. *Hydrogeology Journal*, 18(1), 55-72, doi:10.1007/s10040-009-0533-0.

Knight, A. C., Werner, A. D., Morgan, L. K. (2018). The onshore influence of offshore fresh groundwater. *Journal of Hydrology*, 561, 724-736, doi:10.1016/j.jhydrol.2018.03.028.

Kooi, H., Groen, J. (2001). Offshore continuation of coastal groundwater systems; predictions using sharp-interface approximations and variable-density flow modelling. *Journal of Hydrology*, 246 (1), 19–35, doi:10.1016/S0022-1694(01)00354-7.

Kurylyk, B. L., Irvine, D. J., Mohammed, A. A., Bense, V. F., Briggs, M. A., Loder, J. W., Geshelin, Y. (2018). Rethinking the Use of Seabed Sediment Temperature Profiles to Trace Submarine Groundwater Flow. *Water Resources Research*, 54(7), 4595-4614. doi:10.1029/2017WR022353.

Kvale, E. P. (2012). Tidal Constituents of Modern and Ancient Tidal Rhythmites: Criteria for Recognition and Analyses. In *Principles of Tidal Sedimentology* (pp. 1-17). Springer, Dordrecht.

Langevin, C. D. (2008). Modeling axisymmetric flow and transport. *Groundwater*, 46(4), 579-590, doi: 10.1111/j.1745-6584.2008.00445.x.

Langevin, C. D., Thorne Jr., D. T., Dausman, A. M., Sukop, M. C., Guo, W. (2008). SEAWAT version 4: a computer program for simulation of multi-species solute and heat transport, U. S. Geological Survey Techniques and Methods, Book 6, Chap. A22, 39 pp., Reston, Virginia.

Lapwood, E. R. (1948). Convection of a fluid in a porous medium. *Mathematical Proceedings of the Cambridge Philosophical Society*, 44(4), 508-521. doi:10.1017/S030500410002452X.

Li, H. and Jiao, J. J. (2001). Tide-induced groundwater fluctuation in a coastal leaky confined aquifer system extending under the sea. *Water Resources Research*, 37(5), 1165-1171, doi: 10.1029/2000WR900296.

Llopis-Albert, C., Pulido-Velazquez, D. (2014). Discussion about the validity of sharp-interface models to deal with seawater intrusion in coastal aquifers. *Hydrological Processes*, 28(10), 3642-3654, doi: 10.1002/hyp.9908.

Lohman, S. W. (1972). Ground-Water Hydraulics. Professional Paper 708, U.S. Geological Survey, Washington, doi: 10.3133/pp708.

Lu, C., Chen, Y., Zhang, C., Luo, J. (2013). Steady-state freshwater-seawater mixing zone in stratified coastal aquifers. *Journal of Hydrology*, 505, 24–34, doi: 10.1016/j.jhydrol.2013.09.017.

Luick, J. L. (2004). Australian tidal handbook. National Tidal Centre. Adelaide, South Australia. Commonwealth of Australia.

Mehdizadeh, S. S., Werner, A. D., Vafaie, F., Badaruddin, S. (2014). Vertical leakage in sharp-interface seawater intrusion models of layered coastal aquifers. *Journal of Hydrology*, 519(PA), 1097-1107, doi:10.1016/j.jhydrol.2014.08.027.

Merritt, M. L. (2004). Estimating Hydraulic Properties of the Floridan Aquifer System by Analysis of Earth-Tide, Ocean-Tide, and Barometric Effects, Collier and Hendry Counties, Florida. U.S. Geological Survey. Water-Resources Investigations Report 03-4267.

Michael, H. A., Mulligan, A. E., Harvey, C. F. (2005). Seasonal oscillations in water exchange between aquifers and the coastal ocean. *Nature*, 436(7054), 1145-1148. doi:10.1038/nature03935.

Michael, H. A., Scott, K. C., Koneshloo, M., Yu, X., Khan, M. R., Li, K. (2016). Geologic influence on groundwater salinity drives large seawater circulation through the continental shelf. *Geophysical Research Letters*, 43(20), 10,782-10,791, doi:10.1002/2016GL070863.

Moore, W. S. (1999). The subterranean estuary: a reaction zone of ground water and sea water. *Marine Chemistry*, 65(1-2), 111-125. doi:10.1016/S0304-4203(99)00014-6.

Moore, W. S., Wilson, A. M. (2005). Advective flow through the upper continental shelf driven by storms, buoyancy, and submarine groundwater discharge. *Earth and Planetary Science Letters*, 235(3-4), 564-576. doi:10.1016/j.epsl.2005.04.043.

Mulligan, A. E., Langevin, C., Post, V. E. (2011). Tidal boundary conditions in SEAWAT. *Groundwater*, 49(6), 866-879, doi:10.1111/j.1745-6584.2010.00788.x.

Nelder, J. A., Mead, R. (1965). A simplex method for function minimization. *The Computer Journal*, 7(4), 308-313.

Pool, M., Carrera, J. (2011). A correction factor to account for mixing in Ghyben - Herzberg and critical pumping rate approximations of seawater intrusion in coastal aquifers. *Water Resources Research*, 47(5), doi:10.1029/2010WR010256.

Pool, M., Carrera, J., Dentz, M., Hidalgo, J. J., Abarca, E. (2011). Vertical average for modeling seawater intrusion. *Water Resources Research*, 47(11), doi:10.1029/2011WR010447.

Pool, M., Post, V. E. A. and Simmons, C. T. (2014). Effects of tidal fluctuations on mixing and spreading in coastal aquifers: Homogeneous case. *Water Resources Research*, 50(8), 6910-6926, doi: 10.1002/2014WR015534.

Post, V. E. A. (2011). A new package for simulating periodic boundary conditions in MODFLOW and SEAWAT. *Computers and Geosciences*, 37(11), 1843-1849, doi: 10.1016/j.cageo.2011.01.012.

Post, V. E. A., Kooi, H. (2003). Rates of salinization by free convection in high-permeability sediments: Insights from numerical modeling and application to the dutch coastal area. *Hydrogeology Journal*, 11(5), 549-559. doi:10.1007/s10040-003-0271-7.

Post, V., Kooi, H., Simmons, C. (2007). Using hydraulic head measurements in variable-density ground water flow analyses. *Groundwater*, 45(6), 664-671. doi:10.1111/j.1745-6584.2007.00339.x.

Post, V. E. A., Groen, J., Kooi, H., Person, M., Ge, S., Edmunds, W. M. (2013). Offshore fresh groundwater reserves as a global phenomenon. *Nature*, 504(7478), 71-78, doi:10.1038/nature12858.

Reilly, T. E., Goodman, A. S. (1985). Quantitative analysis of saltwater-freshwater relationships in groundwater systems – A historical perspective. *Journal of Hydrology*, 80(1-2), 125-160.

Riedl, R. J., Huang, N., Machan, R. (1972). The subtidal pump: a mechanism of interstitial water exchange by wave action. *Marine Biology*, 13(3), 210-221. doi:10.1007/BF00391379.

Robinson, N. I., Werner, A. D. (2017). On concentrated solute sources in faulted aquifers. *Advances in Water Resources*, 104, 255-270, doi:10.1016/j.advwatres.2017.04.008.

Rotzoll, K., El-Kadi, A. I. (2008). Estimating hydraulic properties of coastal aquifers using wave setup. *Journal of Hydrology*, 353(1-2), 201-213, doi: 10.1016/j.jhydrol.2008.02.005.

Rotzoll, K., El-Kadi, A. I., Gingerich, S. B. (2008). Analysis of an unconfined aquifer subject to asynchronous dual-tide propagation. *Groundwater*, 46(2), 239-250, doi:10.1111/j.1745-6584.2007.00412.x.

Rotzoll, K., Gingerich, S. B., Jenson, J. W. El-Kadi, A. I. (2013). Estimating hydraulic properties from tidal attenuation in the Northern Guam Lens Aquifer, territory of Guam, USA. *Hydrogeology Journal*, 21(3), 643-654, doi:10.1007/s10040-012-0949-9.

Sebben, M. L., Werner, A. D. (2016). On the effects of preferential or barrier flow features on solute plumes in permeable porous media. *Advances in Water Resources*, 98, 32-46, doi:10.1016/j.advwatres.2016.10.011.

Segol, G., Pinder, G. F., Gray, W. G. (1975). A Galerkin-Finite Element Technique For Calculating The Transient Position Of The Saltwater Front. *Water Resources Research*, 11(2), 343-347.

Serrano, S. E. and Workman, S. R. (1998). Modeling transient stream/aquifer interaction with the non-linear Boussinesq equation and its analytical solution. *Journal of Hydrology*, 206(3-4), 245-255, doi: 10.1016/S0022-1694(98)00111-5.

Shoemaker, W. B. (2004). Important Observations and Parameters for a Salt Water Intrusion Model. *Groundwater*, 42(6), 829-840. doi:10.1111/j.1745-6584.2004.t01-2-.x.

Simmons, C. T., Narayan, K. A. (1997). Mixed convection processes below a saline disposal basin. *Journal of Hydrology*, 194(1-4), 263-285. doi:10.1016/S0022-1694(96)03204-0.

Simmons CT, Bauer-Gottwein P, Graf T, Kinzelbach W, Kooi H, Li L, Post V, Prommer H, Therrien R, Voss C, Ward J, Werner A (2010) Variable density groundwater flow: from modelling to applications, Chapter 7, In: Wheater HS, Mathias SA and Li X (Ed.) “Groundwater Modelling in Arid and Semi-Arid Areas”, 87-117, International Hydrology Series, Cambridge University Press, ISBN: 978-0-521-11129-4.

Smith, A. J. (1999). Application of a Tidal Method for Estimating Aquifer Diffusivity: Swan River, Western Australia. CSIRO Land and Water. Technical Report 13/99.

Smith, A. J. (2004). Mixed convection and density-dependent seawater circulation in coastal aquifers. *Water Resources Research*, 40(8), W08309, doi: 10.1029/2003WR002977.

Smith, A. J., Turner, J. V. (2001). Density-dependent surface water-groundwater interaction and nutrient discharge in the Swan-Canning Estuary. *Hydrological Processes*, 15(13), 2595-2616, doi: 10.1002/hyp.303.

Solórzano-Rivas, S. C., Werner, A. D. (2018). On the representation of subsea aquitards in models of offshore fresh groundwater. *Advances in Water Resources*, 112, 283-294, doi: 10.1016/j.advwatres.2017.11.025.

Solórzano-Rivas, S. C., Werner, A. D. (2020). Applicability of analytical solutions to tidal propagation in circular islands. *Journal of Hydrology*, 589. doi:10.1016/j.jhydrol.2020.125136.

Solórzano-Rivas, S. C., Werner, A. D., Irvine, D. J. (2019). Dispersion effects on the freshwater–seawater interface in subsea aquifers. *Advances in Water Resources*, 130, 184-197. doi:10.1016/j.advwatres.2019.05.022.

Stevens, J. D., Sharp Jr., J. M., Simmons, C. T., Fenstermaker, T. R. (2009). Evidence of free convection in groundwater: Field-based measurements beneath wind-tidal flats. *Journal of Hydrology*, 375(3-4), 394-409. doi:10.1016/j.jhydrol.2009.06.035.

Stewart, R. H. (2008). Introduction to Physical Oceanography. Texas A&M University.

Taniguchi, M., Burnett, W. C., Smith, C. F., Paulsen, R. J., O'Rourke, D., Krupa, S. L., Christoff, J. L. (2003). Spatial and temporal distributions of submarine groundwater discharge rates obtained from various types of seepage meters at a site in the Northeastern Gulf of Mexico. *Biogeochemistry*, 66(1-2), 35-53. doi:10.1023/B:BIOG.0000006090.25949.8d.

Taniguchi, M., Dulai, H., Burnett, K. M., Santos, I. R., Sugimoto, R., Stieglitz, T., Kim, G., Moosdorf, N., Burnett, W. C. (2019). Submarine groundwater discharge: Updates on its measurement techniques, geophysical drivers, magnitudes, and effects. *Frontiers in Environmental Science*, 7:141. doi:10.3389/fenvs.2019.00141.

Theis, C. V. (1935). The relation between the lowering of the piezometric surface and the rate and duration of discharge of a well using ground-water storage. *Transactions American Geophysical Union*, 16(2), 519-524.

Townley, L. R. (1995). The response of aquifers to periodic forcing. *Advances in Water Resources*, 18(3), 125-146, doi: 10.1016/0309-1708(95)00008-7.

Trefry, M. G. (1999). Periodic forcing in composite aquifers. *Advances in Water Resources*, 22(6), 645-656, doi: 10.1016/S0309-1708(98)00037-2.

Trefry, M. G., Bekele, E. (2004). Structural characterization of an island aquifer via tidal methods. *Water Resources Research*, 40(1), W015051, doi: 10.1029/2003WR002003.

Trglavcnik, V., Morrow, D., Weber, K. P., Li, L., Robinson, C. E. (2018). Analysis of tide and offshore storm-induced water table fluctuations for structural characterization of a coastal island aquifer. *Water Resources Research*, 54(4), 2749-2767, doi:10.1002/2017WR020975.

van Reeuwijk, M., Mathias, S. A., Simmons, C. T., Ward, J. D. (2009). Insights from a pseudospectral approach to the Elder problem. *Water Resources Research*, 45(4). doi:10.1029/2008WR007421.

Volker, R. E., Rushton, K. R. (1982). An assessment of the importance of some parameters for seawater intrusion in aquifers and a comparison of dispersive and sharp-interface modelling approaches. *Journal of Hydrology*, 56(3-4), 239-250, doi :10.1016/0022-1694(82)90015-4.

Voss, C. I., Souza, W. R. (1987). Variable Density Flow and Solute Transport Simulation of Regional Aquifers Containing a Narrow Freshwater-Saltwater Transition Zone. *Water Resources Research*, 23(10), 1851-1866. doi:10.1029/WR023i010p01851.

Webster, I. T., Norquay, S. J., Ross, F. C., Wooding, R. A. (1996). Solute exchange by convection within estuarine sediments. *Estuarine, Coastal and Shelf Science*, 42(2), 171-183. doi:10.1006/ecss.1996.0013.

Werner, A. D. (2017a). Correction factor to account for dispersion in sharp-interface models of terrestrial freshwater lenses and active seawater intrusion. *Advances in Water Resources*, 102, 45-52, doi: 10.1016/j.advwatres.2017.02.001.

Werner, A. D. (2017b). On the classification of seawater intrusion. *Journal of Hydrology*, 551, 619-631, doi: 10.1016/j.jhydrol.2016.12.012.

Werner, A. D., Laattoe, T. (2016). Terrestrial freshwater lenses in stable riverine settings: Occurrence and controlling factors. *Water Resources Research*, 52(5), 3654-3662, doi:10.1002/2015WR018346.

Werner, A. D., Lockington, D. A. (2006). Tidal impacts on riparian salinities near estuaries. *Journal of Hydrology*, 328(3-4), 511-522., doi: 10.1016/j.jhydrol.2005.12.011.

Werner, A. D., Robinson, N. I. (2018). Revisiting analytical solutions for steady interface flow in subsea aquifers: Aquitard salinity effects. *Advances in Water Resources*, 116, 117-126, doi:10.1016/j.advwatres.2018.01.002.

Werner, A. D., Simmons, C. T. (2009). Impact of sea-level rise on sea water intrusion in coastal aquifers. *Groundwater*, 47(2), 197-204, doi:10.1111/j.1745-6584.2008.00535.x.

Werner, A. D., Sharp, H. K., Galvis, S. C., Post, V. E. A., Sinclair, P. (2017). Hydrogeology and management of freshwater lenses on atoll islands: Review of current knowledge and research needs. *Journal of Hydrology*, 551, 819-844, doi: 10.1016/j.jhydrol.2017.02.047.

White, I., Falkland, T. (2010). Management of freshwater lenses on small pacific islands. [Gestion des lentilles d'eau douce dans de petites îles du Pacifique]. *Hydrogeology Journal*, 18(1), 227-246, doi:10.1007/s10040-009-0525-0.

Williams, J. A., Wada, R. N., Wang, R. (1970). Model studies of tidal effects on ground water hydraulics. Technical Report No. 39. Project Completion Report of Tidal effects on ground-water hydraulics in Hawaii. Water Resources Research Center. Department of the Interior, USA.

Wooding, R. A. (1969). Growth of fingers at an unstable diffusing interface in a porous medium or Hele-Shaw cell. *Journal of Fluid Mechanics*, 39(3), 477-495. doi:10.1017/S002211206900228X.

Wooding, R. A., Tyler, S. W., White, I. (1997). Convection in groundwater below an evaporating salt lake: 1. Onset of instability. *Water Resources Research*, 33(6), 1199-1217, doi: 10.1029/96WR03533.

Xie, Y., Simmons, C. T., Werner, A. D., Ward, J. D. (2010). Effect of transient solute loading on free convection in porous media. *Water Resources Research*, 46(11). doi:10.1029/2010WR009314.

Xie, Y., Simmons, C. T., Werner, A. D. (2011). Speed of free convective fingering in porous media. *Water Resources Research*, 47(11). doi:10.1029/2011WR010555.

Xun, Z., Chuanxia, R., Yanyan, Y., Bin, F., Yecheng, O. (2006). Tidal effects of groundwater levels in the coastal aquifers near Beihai, China. *Environmental Geology*, 51(4), 517-525, doi:10.1007/s00254-006-0348-4.

Xun, Z., Chao, S., Ting, L., Ruige, C., Huan, Z., Jingbo, Z., Qin, C. (2015). Estimation of aquifer parameters using tide-induced groundwater level measurements in a coastal confined aquifer. *Environmental Earth Sciences*, 73(5), 2197-2204, doi:10.1007/s12665-014-3570-5.

Zech, A., Attinger, S., Cvetkovic, V., Dagan, G., Dietrich, P., Fiori, A., Rubin, Y., Teutsch, G. (2015). Is unique scaling of aquifer macrodispersivity supported by field data? *Water Resources Research*, 51(9), 7662-7679, doi:10.1002/2015WR017220.

Zheng, C., Bennett, G. D. (2002). *Applied Contaminant Transport Modeling, Second Ed.* Wiley-Interscience, New York, pp. 656.

Zheng, C., Wang, P. P. (1999). MT3DMS: A modular three-dimensional multispecies transport model for simulation of advection, dispersion, and chemical reactions of contaminants in groundwater systems-documentation and user's guide. Contract report SERDP-99-1, U. S. Army Engineer Research and Development Center, Vicksburg, Mississippi.

Zhou, X. (2008). Determination of aquifer parameters based on measurements of tidal effects on a coastal aquifer near Beihai, China. *Hydrological Processes*, 22(16), 3176-3180, doi:10.1002/hyp.6906.

## Appendix A

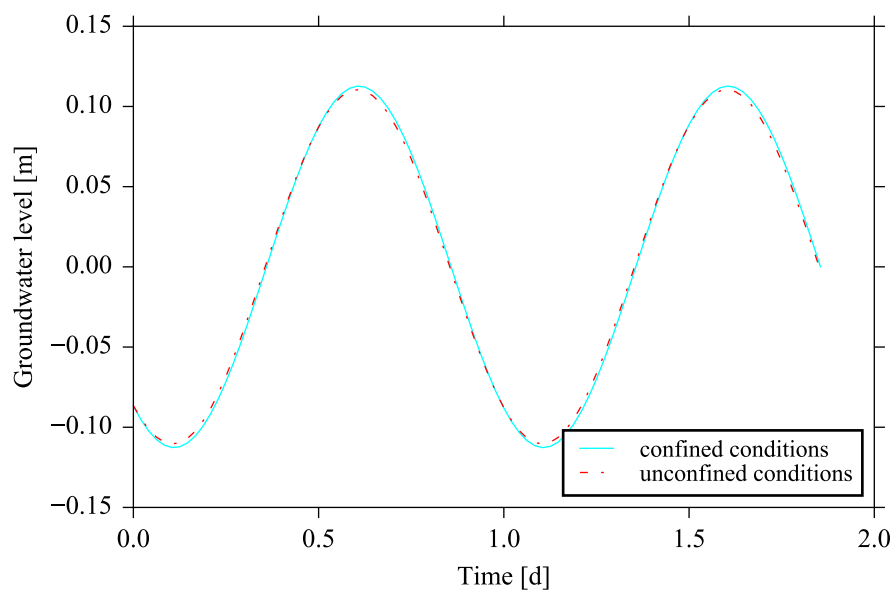


**Figure A1.** Comparison of groundwater tides for both confined and unconfined conditions (without noise), at the  $0.3a$  inland distance for the  $K_1$ -constituent,  $\lambda_3$ -scenario (i.e.,  $500,000 \text{ m}^2/\text{d}$ ).

**Table A1.** Relative errors,  $E_r$ , for estimated values of  $\lambda_A$ ,  $\lambda_\phi$ ,  $\lambda_{A,\phi}$  and the average ( $\lambda_{av}$ ) of  $\lambda_A$  and  $\lambda_\phi$ , applying the circular solution under confined conditions for the three  $\lambda$ -scenarios. Results are based on theoretical observations with noise ( $A'_{g,obs}$  and  $\phi'_{obs}$ ).

$\lambda$ -scenario [m <sup>2</sup> /d]	Constituent	Distance from the shoreline	$E_r$ [%]			
			$\lambda_A$	$\lambda_\phi$	$\lambda_{A,\phi}$	$\lambda_{av}$
$\lambda_1$ <b>150,000</b>	K <sub>1</sub> $\tau = 23.93$ hr	0.1a	0.059	-0.064	-0.058	-0.002
		0.2a	0.139	0.085	0.086	0.112
		0.3a	-0.139	0.379	0.379	0.120
	= M <sub>2</sub> $\tau = 12.42$ hr	0.1a	0.131	-0.154	-0.143	-0.012
		0.2a	0.328	0.554	0.553	0.441
		0.3a	-2.698	0.562	0.562	-1.068
	MK <sub>3</sub> $\tau = 8.18$ hr	0.1a	-0.291	-0.401	-0.401	-0.346
		0.2a	2.41	0.350	0.350	1.38
		0.3a	-11.5	17.8	17.8	3.16
$\lambda_2$ <b>350,000</b>	K <sub>1</sub> $\tau = 23.93$ hr	0.1a	-0.328	-0.008	-0.049	-0.168
		0.2a	-0.228	-0.304	-0.302	-0.266
		0.3a	0.149	-0.562	-0.558	-0.206
	= M <sub>2</sub> $\tau = 12.42$ hr	0.1a	0.033	-0.048	-0.037	-0.008
		0.2a	0.093	0.027	0.027	0.060
		0.3a	0.009	0.210	0.209	0.109
	MK <sub>3</sub> $\tau = 8.18$ hr	0.1a	0.151	0.094	0.095	0.122
		0.2a	-0.196	0.339	0.339	0.072
		0.3a	-0.996	-0.552	-0.552	-0.774
$\lambda_3$ <b>500,000</b>	K <sub>1</sub> $\tau = 23.93$ hr	0.1a	-0.335	0.042	-0.021	-0.147
		0.2a	-0.273	-0.200	-0.204	-0.237
		0.3a	-0.081	-0.440	-0.436	-0.261
	= M <sub>2</sub> $\tau = 12.42$ hr	0.1a	0.022	-0.053	-0.039	-0.015
		0.2a	0.076	-0.010	-0.007	0.033
		0.3a	0.082	0.108	0.108	0.095
	MK <sub>3</sub> $\tau = 8.18$ hr	0.1a	0.157	0.050	0.052	0.104
		0.2a	-0.007	0.283	0.282	0.138
		0.3a	-0.616	0.164	0.163	-0.226

**Table A2.**  $\lambda$  estimates ( $\lambda_A$ ,  $\lambda_\phi$ ,  $\lambda_{A,\phi}$  and  $\lambda_{av}$ ) from numerical observations ( $A_{n,obs}$  and  $\phi_{n,obs}$ ) and numerical observations with noise ( $A'_{n,obs}$  and  $\phi'_{n,obs}$ ) of the  $K_1$  tidal constituent. Relative errors,  $E_r$ , for estimated values of  $\lambda_A$ ,  $\lambda_\phi$ ,  $\lambda_{A,\phi}$  and  $\lambda_{av}$  for the three  $\lambda$ -scenarios are also shown.

Observations	$\lambda$ -scenario [m <sup>2</sup> /d]	Distance from the shoreline	$\lambda$ [m <sup>2</sup> /d]			
			$\lambda_A$ [m <sup>2</sup> /d]	$\lambda_\phi$ [m <sup>2</sup> /d]	$\lambda_{A,\phi}$ [m <sup>2</sup> /d]	$\lambda_{av}$ [m <sup>2</sup> /d]
Numerical ( $A_{n,obs}$ and $\phi_{n,obs}$ )	$\lambda_1 =$ 150,000	0.1a	147,314 (-1.791)	153,226 (2.150)	152,890 (1.927)	150,270 (0.180)
		0.2a	147,375 (-1.750)	152,890 (1.927)	152,866 (1.911)	150,132 (0.088)
		0.3a	147,806 (-1.463)	152,806 (1.871)	152,805 (1.870)	150,306 (0.204)
	$\lambda_2 =$ 350,000	0.1a	343,779 (-1.777)	357,298 (2.085)	355,485 (1.567)	350,538 (0.154)
		0.2a	343,648 (-1.815)	357,404 (2.115)	357,013 (2.004)	350,526 (0.150)
		0.3a	343,860 (-1.754)	356,799 (1.943)	356,728 (1.922)	350,330 (0.094)
	$\lambda_3 =$ 500,000	0.1a	491,053 (-1.789)	510,168 (2.034)	506,880 (1.376)	500,611 (0.122)
		0.2a	491,011 (-1.798)	510,742 (2.148)	509,756 (1.951)	500,876 (0.175)
		0.3a	490,977 (-1.805)	510,153 (2.031)	509,898 (1.980)	500,565 (0.113)
Numerical with noise ( $A'_{n,obs}$ and $\phi'_{n,obs}$ )	$\lambda_1 =$ 150,000	0.1a	147,401 (-1.733)	153,123 (2.082)	152,799 (1.866)	150,262 (0.175)
		0.2a	147,586 (-1.609)	153,020 (2.013)	152,996 (1.997)	150,303 (0.202)
		0.3a	147,617 (-1.589)	153,418 (2.278)	153,416 (2.277)	150,517 (0.345)
	$\lambda_2 =$ 350,000	0.1a	342,654 (-2.099)	357,281 (2.080)	355,317 (1.519)	349,967 (-0.009)
		0.2a	342,837 (-2.047)	356,303 (1.801)	355,922 (1.692)	349,570 (-0.123)
		0.3a	344,330 (-1.620)	354,714 (1.347)	354,657 (1.331)	349,522 (-0.137)
	$\lambda_3 =$ 500,000	0.1a	489,412 (-2.118)	510,399 (2.080)	506,782 (1.356)	499,905 (-0.019)
		0.2a	489,649 (-2.070)	509,716 (1.943)	508,716 (1.743)	499,683 (-0.063)
		0.3a	490,525 (-1.895)	507,846 (1.569)	507,618 (1.523)	499,185 (-0.163)

**Table A3.**  $\lambda$  estimates ( $\lambda_{AF}$ ,  $\lambda_{\phi F}$  and  $\lambda_{avF}$ ) from theoretical observations ( $A_{g,obs}$  and  $\phi_{obs}$ ) and theoretical observations with noise ( $A'_{g,obs}$  and  $\phi'_{obs}$ ) applying the corrected Ferris solution (i.e., confined conditions), and their corresponding relative errors,  $E_r$ , for the  $\lambda_1$ -scenario. Note that at the inland distance of  $0.3a$  for the MK<sub>3</sub> constituent,  $\lambda_1$ -scenario, the  $\lambda_{\phi}$  estimate (i.e., values with asterisks) did require the cycle correction mentioned in Section 6.4.1. The number of tidal cycles transpired was determined by comparing  $\phi_{obs}$  and  $\phi'_{obs}$  values with phase lags at distances closer to the shoreline (i.e.,  $0.2a$  and  $0.1a$ ; Table 2). It was thereby ascertained that only one tidal cycle had occurred (i.e.,  $k = 1$ ) at the inland distance of  $0.3a$ . Therefore, at the inland distance of  $0.3a$  for the MK<sub>3</sub> constituent,  $\lambda_1$ -scenario, the value of  $2\pi$  was added to the corresponding values of  $\phi_{obs}$  and  $\phi'_{obs}$  (Table 2) for the inverse estimation of  $\lambda$  from the corrected Ferris solution.

Constituent	Distance from the shoreline	Theoretical observations			Theoretical observations with noise		
		$\lambda_{AF}$ [m <sup>2</sup> /d] ( $E_r$ ) [%]	$\lambda_{\phi F}$ [m <sup>2</sup> /d] ( $E_r$ ) [%]	$\lambda_{avF}$ [m <sup>2</sup> /d] ( $E_r$ ) [%]	$\lambda_{AF}$ [m <sup>2</sup> /d] ( $E_r$ ) [%]	$\lambda_{\phi F}$ [m <sup>2</sup> /d] ( $E_r$ ) [%]	$\lambda_{avF}$ [m <sup>2</sup> /d] ( $E_r$ ) [%]
<b>K<sub>1</sub></b> $\tau = 23.93$ hr	0.1a	150,110 (0.073)	149,881 (-0.079)	149,995 (-0.003)	150,199 (0.133)	149,881 (-0.079)	150,040 (0.027)
	0.2a	150,123 (0.082)	149,865 (-0.090)	149,994 (-0.004)	150,332 (0.221)	149,865 (-0.090)	150,099 (0.066)
	0.3a	150,141 (0.094)	149,845 (-0.103)	149,993 (-0.005)	149,932 (-0.045)	149,845 (-0.103)	149,889 (-0.074)
<b>M<sub>2</sub></b> $\tau = 12.42$ hr	0.1a	150,057 (0.038)	149,940 (-0.040)	149,998 (-0.001)	150,253 (0.169)	149,940 (-0.040)	150,096 (0.064)
	0.2a	150,064 (0.043)	149,932 (-0.046)	149,998 (-0.001)	150,557 (0.371)	149,932 (-0.046)	150,244 (0.163)
	0.3a	150,073 (0.049)	149,922 (-0.052)	149,997 (-0.002)	146,022 (-2.65)	149,922 (-0.052)	147,972 (-1.35)
<b>MK<sub>3</sub></b> $\tau = 8.18$ hr	0.1a	150,038 (0.025)	149,961 (-0.026)	149,999 (-0.001)	149,600 (-0.267)	149,961 (-0.026)	149,780 (-0.146)
	0.2a	150,042 (0.028)	149,956 (-0.030)	149,999 (-0.001)	153,653 (2.44)	149,956 (-0.030)	151,804 (1.20)
	0.3a	150,048 (0.032)	149,949* (-0.034)	149,999 (-0.001)	132,774 (-11.5)	176,686* (17.8)	154,730 (3.15)

**Table A4.**  $\lambda$  estimates ( $\lambda_{AF}$ ,  $\lambda_{\phi F}$  and  $\lambda_{avF}$ ) from theoretical observations ( $A_{g,obs}$  and  $\varphi_{obs}$ ) and theoretical observations with noise ( $A'_{g,obs}$  and  $\varphi'_{obs}$ ) applying the corrected Ferris solution (i.e., confined conditions), and their corresponding relative errors,  $E_r$ , for the  $\lambda_2$ -scenario (i.e.  $\lambda = 350,000 \text{ m}^2/\text{d}$ ).

Constituent	Distance from the shoreline	Theoretical observations			Theoretical observations with noise		
		$\lambda_{AF}$ [m <sup>2</sup> /d] ( $E_r$ ) [%]	$\lambda_{\phi F}$ [m <sup>2</sup> /d] ( $E_r$ ) [%]	$\lambda_{avF}$ [m <sup>2</sup> /d] ( $E_r$ ) [%]	$\lambda_{AF}$ [m <sup>2</sup> /d] ( $E_r$ ) [%]	$\lambda_{\phi F}$ [m <sup>2</sup> /d] ( $E_r$ ) [%]	$\lambda_{avF}$ [m <sup>2</sup> /d] ( $E_r$ ) [%]
<b>K<sub>1</sub></b> $\tau = 23.93 \text{ hr}$	0.1a	350,592 (0.169)	349,324 (-0.193)	349,958 (-0.012)	349,442 (-0.159)	349,324 (-0.193)	349,383 (-0.176)
	0.2a	350,665 (0.190)	349,234 (-0.219)	349,950 (-0.014)	349,863 (-0.039)	349,234 (-0.219)	349,548 (-0.129)
	0.3a	350,758 (0.217)	349,117 (-0.252)	349,937 (-0.018)	351,282 (0.366)	349,117 (-0.252)	350,200 (0.057)
<b>M<sub>2</sub></b> $\tau = 12.42 \text{ hr}$	0.1a	350,310 (0.088)	349,661 (-0.097)	349,985 (-0.004)	350,425 (0.122)	349,661 (-0.097)	350,043 (0.012)
	0.2a	350,348 (0.099)	349,616 (-0.110)	349,982 (-0.005)	350,672 (0.192)	349,616 (-0.110)	350,144 (0.041)
	0.3a	350,397 (0.113)	349,558 (-0.126)	349,978 (-0.006)	350,429 (0.123)	349,558 (-0.126)	349,994 (-0.002)
<b>MK<sub>3</sub></b> $\tau = 8.18 \text{ hr}$	0.1a	350,204 (0.058)	349,780 (-0.063)	349,992 (-0.002)	350,732 (0.209)	349,780 (-0.063)	350,256 (0.073)
	0.2a	350,230 (0.066)	349,752 (-0.071)	349,991 (-0.003)	349,544 (-0.130)	349,752 (-0.071)	349,648 (-0.101)
	0.3a	350,262 (0.075)	349,714 (-0.082)	349,988 (-0.003)	346,771 (-0.923)	349,714 (-0.082)	348,243 (-0.502)

**Table A5.**  $\lambda$  estimates ( $\lambda_{AF}$ ,  $\lambda_{\phi F}$  and  $\lambda_{avF}$ ) from theoretical observations ( $A_{g,obs}$  and  $\varphi_{obs}$ ) and theoretical observations with noise ( $A'_{g,obs}$  and  $\varphi'_{obs}$ ) applying the corrected Ferris solution (i.e., confined conditions), and their corresponding relative errors,  $E_r$ , for the  $\lambda_3$ -scenario. (i.e.  $\lambda = 500,000 \text{ m}^2/\text{d}$ ).

Constituent	Distance from the shoreline	Theoretical observations			Theoretical observations with noise		
		$\lambda_{AF}$ [m <sup>2</sup> /d] ( $E_r$ ) [%]	$\lambda_{\phi F}$ [m <sup>2</sup> /d] ( $E_r$ ) [%]	$\lambda_{avF}$ [m <sup>2</sup> /d] ( $E_r$ ) [%]	$\lambda_{AF}$ [m <sup>2</sup> /d] ( $E_r$ ) [%]	$\lambda_{\phi F}$ [m <sup>2</sup> /d] ( $E_r$ ) [%]	$\lambda_{avF}$ [m <sup>2</sup> /d] ( $E_r$ ) [%]
<b>K<sub>1</sub></b> $\tau = 23.93 \text{ hr}$	0.1a	501,203 (0.240)	498,591 (-0.282)	499,897 (-0.021)	499,518 (-0.096)	498,799 (-0.240)	499,159 (-0.168)
	0.2a	501,345 (0.269)	498,402 (-0.320)	499,874 (-0.025)	499,974 (-0.005)	497,407 (-0.519)	498,690 (-0.262)
	0.3a	501,522 (0.304)	498,143 (-0.371)	499,833 (-0.033)	501,114 (0.223)	495,958 (-0.808)	498,536 (-0.293)
<b>M<sub>2</sub></b> $\tau = 12.42 \text{ hr}$	0.1a	500,630 (0.126)	499,296 (-0.141)	499,963 (-0.007)	500,740 (0.148)	499,033 (-0.193)	499,887 (-0.023)
	0.2a	500,708 (0.142)	499,203 (-0.159)	499,955 (-0.009)	501,088 (0.218)	499,154 (-0.169)	500,121 (-0.024)
	0.3a	500,807 (0.161)	499,081 (-0.184)	499,944 (-0.011)	501,220 (0.244)	499,617 (-0.077)	500,419 (0.084)
<b>MK<sub>3</sub></b> $\tau = 8.18 \text{ hr}$	0.1a	500,416 (0.083)	499,545 (-0.091)	499,981 (-0.004)	501,204 (0.241)	499,795 (-0.041)	500,500 (0.100)
	0.2a	500,468 (0.094)	499,486 (-0.103)	499,977 (-0.005)	500,434 (0.087)	500,896 (0.179)	500,665 (0.133)
	0.3a	500,534 (0.107)	499,408 (-0.118)	499,971 (-0.006)	497,445 (-0.511)	500,224 (0.045)	498,835 (-0.233)

**Table A6.**  $\lambda$  estimates ( $\lambda_{AF}$ ,  $\lambda_{\phi F}$  and  $\lambda_{avF}$ ) from numerical observations ( $A_{n,obs}$  and  $\phi_{n,obs}$ ) and numerical observations with noise ( $A'_{n,obs}$  and  $\phi'_{n,obs}$ ) of the  $K_1$  tidal constituent by the corrected Ferris solution (i.e., unconfined conditions), and their corresponding relative errors,  $E_r$ , for the three  $\lambda$ -scenarios.

$\lambda$ -scenario [m <sup>2</sup> /d]	Distance from the shoreline	Numerical observations			Numerical observations with noise		
		$\lambda_{AF}$ [m <sup>2</sup> /d] ( $E_r$ ) [%]	$\lambda_{\phi F}$ [m <sup>2</sup> /d] ( $E_r$ ) [%]	$\lambda_{avF}$ [m <sup>2</sup> /d] ( $E_r$ ) [%]	$\lambda_{AF}$ [m <sup>2</sup> /d] ( $E_r$ ) [%]	$\lambda_{\phi F}$ [m <sup>2</sup> /d] ( $E_r$ ) [%]	$\lambda_{avF}$ [m <sup>2</sup> /d] ( $E_r$ ) [%]
$\lambda_1 = 150,000$	0.1a	147,429 (-1.72)	153,101 (2.07)	150,260 (0.17)	147,507 (-1.66)	152,999 (2.0)	150,253 (0.17)
	0.2a	147,494 (-1.67)	152,750 (1.83)	150,122 (0.08)	147,705 (-1.53)	152,880 (1.92)	150,292 (0.19)
	0.3a	147,943 (-1.37)	152,645 (1.76)	150,294 (0.20)	147,753 (-1.50)	153,256 (2.17)	150,504 (0.34)
$\lambda_2 = 350,000$	0.1a	344,351 (-1.61)	356,593 (1.88)	350,472 (0.13)	343,222 (-1.94)	356,576 (1.88)	349,899 (-0.03)
	0.2a	344,289 (-1.63)	356,604 (1.89)	350,447 (0.13)	343,476 (-1.86)	355,508 (1.57)	349,492 (-0.15)
	0.3a	344,592 (-1.55)	355,880 (1.68)	350,236 (0.07)	345,064 (-1.41)	353,806 (1.09)	349,435 (-0.16)
$\lambda_3 = 500,000$	0.1a	492,214 (-1.56)	508,700 (1.74)	500,457 (0.09)	490,565 (-1.89)	508,929 (1.79)	499,747 (-0.05)
	0.2a	492,309 (-1.54)	509,072 (1.81)	500,691 (0.14)	490,940 (-1.81)	508,053 (1.61)	499,497 (-0.10)
	0.3a	492,446 (-1.51)	508,214 (1.64)	500,331 (0.07)	491,991 (-1.60)	505,927 (1.19)	498,959 (-0.21)

**Table A7.**  $\lambda$  estimates ( $\lambda_{AF}$ ,  $\lambda_{\phi F}$  and  $\lambda_{avF}$ ) from theoretical observations ( $A_{obs}$  and  $\phi_{obs}$ ) and theoretical observations with noise ( $A'_{obs}$  and  $\phi'_{obs}$ ) of the  $K_1$  tidal constituent by the Ferris solution (i.e., without correction factor and confined conditions), and their corresponding relative errors,  $E_r$ , for the three  $\lambda$ -scenarios.

$\lambda$ -scenario [m <sup>2</sup> /d]	Distance from the shoreline	Theoretical observations			Theoretical observations with noise		
		$\lambda_{AF}$ [m <sup>2</sup> /d] ( $E_r$ ) [%]	$\lambda_{\phi F}$ [m <sup>2</sup> /d] ( $E_r$ ) [%]	$\lambda_{avF}$ [m <sup>2</sup> /d] ( $E_r$ ) [%]	$\lambda_{AF}$ [m <sup>2</sup> /d] ( $E_r$ ) [%]	$\lambda_{\phi F}$ [m <sup>2</sup> /d] ( $E_r$ ) [%]	$\lambda_{avF}$ [m <sup>2</sup> /d] ( $E_r$ ) [%]
$\lambda_1 = 150,000$	0.1a	162,313 (8.21)	149,881 (-0.079)	156,097 (4.06)	162,414 (8.28)	149,785 (-0.144)	156,099 (4.07)
	0.2a	163,094 (8.73)	149,865 (-0.090)	156,480 (4.32)	163,331 (8.89)	149,993 (-0.005)	156,662 (4.44)
	0.3a	164,023 (9.35)	149,845 (-0.103)	156,934 (4.62)	163,785 (9.19)	150,413 (-0.275)	157,099 (4.73)
$\lambda_2 = 350,000$	0.1a	395,577 (13.0)	349,324 (-0.193)	372,451 (6.41)	394,198 (12.6)	349,298 (-0.201)	371,748 (6.21)
	0.2a	398,583 (13.9)	349,234 (-0.219)	373,909 (6.83)	397,611 (13.6)	348,174 (-0.522)	372,893 (6.54)
	0.3a	402,178 (14.9)	349,117 (-0.252)	375,648 (7.33)	402,823 (15.1)	347,162 (-0.811)	374,992 (7.14)
$\lambda_3 = 500,000$	0.1a	579,536 (15.9)	498,591 (-0.281)	539,063 (7.81)	577,442 (15.5)	498,799 (-0.240)	538,121 (7.62)
	0.2a	584,896 (17.0)	498,402 (-0.320)	541,649 (8.33)	583,168 (16.6)	497,407 (-0.519)	540,287 (8.06)
	0.3a	591,320 (18.3)	498,143 (-0.371)	544,732 (8.95)	590,797 (18.2)	495,958 (-0.808)	543,378 (8.68)

**Table A8.** Parameters obtained from the harmonic analysis of the numerical observations for unconfined conditions with noise ( $A'_{n,obs}$  and  $\varphi'_{n,obs}$ ) for the  $K_1$  constituent, and their respective relative errors. Amplitude values smaller than 2.5 cm are denoted by †.

$\lambda$ -scenario [m <sup>2</sup> /d]	Distance from the shoreline	Numerical observations with noise		$E_A$ [%]	$E_\varphi$ [%]
		$A'_{n,obs}$ [m]	$\varphi'_{n,obs}$ [rad]		
$\lambda_1 = 150,000$	$0.1a$	0.237	1.361	-1.241	-1.057
	$0.2a$	0.063	2.724	-2.410	-0.949
	$0.3a$	0.017†	4.081†	-3.005†	-0.921†
$\lambda_2 = 350,000$	$0.1a$	0.382	0.892	-0.956	-1.022
	$0.2a$	0.163	1.784	-1.855	-0.886
	$0.3a$	0.071	2.678	-2.192	-0.665
$\lambda_3 = 500,000$	$0.1a$	0.444	0.746	-0.808	-1.021
	$0.2a$	0.220	1.494	-1.573	-0.954
	$0.3a$	0.110	2.246	-2.151	-0.772

**Table A9.** Parameters obtained from harmonic analysis of the numerical observations for unconfined conditions without noise ( $A_{n,obs}$  and  $\varphi_{n,obs}$ ) for the  $M_2$ -constituent,  $\lambda_3$ -scenario (i.e., 500,000 m<sup>2</sup>/d). Note that all values of  $A_{n,obs}$  are smaller than 1.5 mm.

$\lambda$ -scenario [m <sup>2</sup> /d]	Distance from the shoreline	Numerical observations (no noise)	
		$A_{n,obs}$ [mm]	$\varphi_{n,obs}$ [rad]
$\lambda_3 = 500,000$	$0.1a$	1.22	0.746
	$0.2a$	0.61	1.494
	$0.3a$	0.35	2.246

## Appendix B

A Groundwater Modelling Investigation of Greywater Disposal: South Tarawa, Kiribati. Jazayeri, Amir; Solórzano-Rivas, S. Cristina; Sinclair, Peter; Antoniou, Andreas; Irvine, Dylan J.; Werner, Adrian D.. 2019. A Groundwater Modelling Investigation of Greywater Disposal : South Tarawa, Kiribati. World Bank, Washington, DC. © World Bank. <https://openknowledge.worldbank.org/handle/10986/32766> License: CC BY 3.0 IGO.

*Approximate contribution of co-author: S.C. Solórzano-Rivas (80%, which includes all the numerical model simulations - Chapters 5, 6 and 7)*